AD-A117 497 JAYCOR SAN DIEGO CA F/G 4/1
SOME PHYSICAL AND CHEMICAL ASPECTS OF STRIATION STRUCTURE.(U)
AUG 80 S R GOLDMAN, J L SPERLING DNA001-79-C-0050
UNCLASSIFIED DNA-5912Z NL

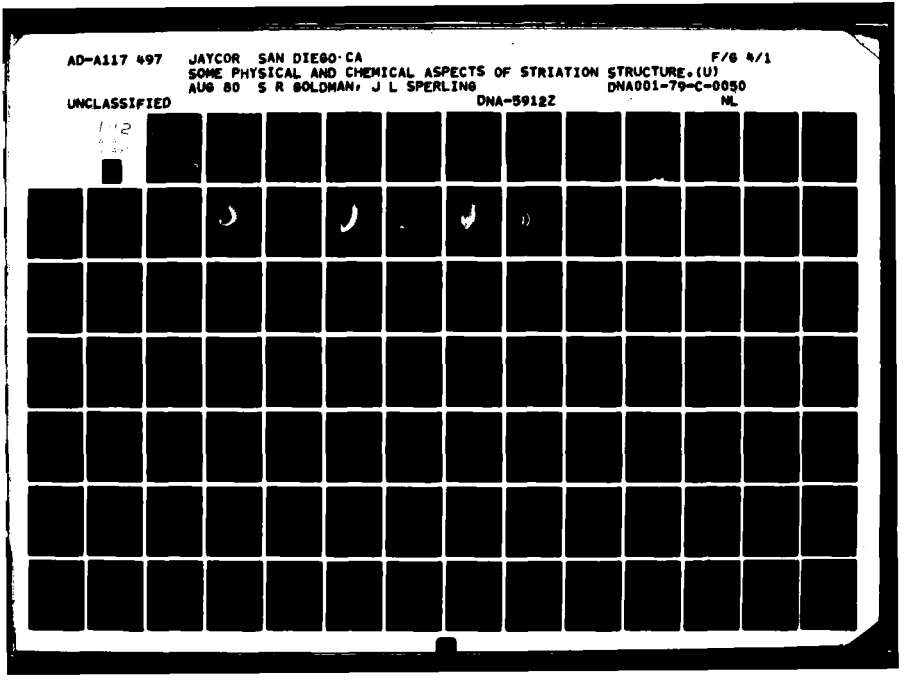

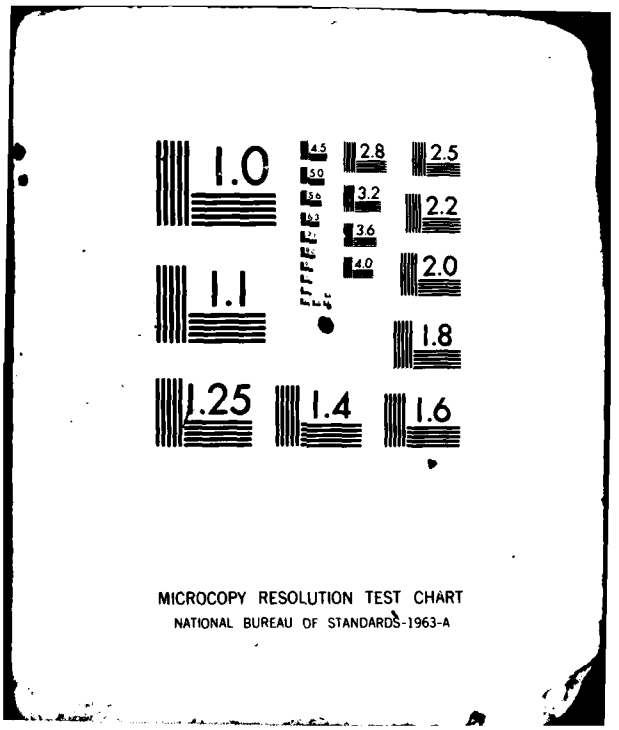
1.0
1.1
1.25
1.4
1.6
1.8
2.0
2.2
2.5
2.8
3.2
3.6
4.0
4.5
5.0
5.6
MICROCOPY RESOLUTION TEST CHART
NATIONAL BUREAU OF STANDARDS-1963-A

DNA 5912Z

SOME PHYSICAL AND CHEMICAL ASPECTS OF STRIATION STRUCTURE

S. R. Goldman
J. L. Sperling
JAYCOR
P.O. Box 85154
San Diego, California 92138

15 August 1980

Interim Report for Period 1 February 1979—15 August 1980

CONTRACT No. DNA 001-79-C-0050

APPROVED FOR PUBLIC RELEASE;
DISTRIBUTION UNLIMITED.

THIS WORK SPONSORED BY THE DEFENSE NUCLEAR AGENCY
UNDER RDT&E RMSS CODE B322080464 S99QAXHC04124 H2590D.

Prepared for
Director
DEFENSE NUCLEAR AGENCY
Washington, D. C. 20305

Destroy this report when it is no longer needed. Do not return to sender.

PLEASE NOTIFY THE DEFENSE NUCLEAR AGENCY, ATTN: STTI, WASHINGTON, D.C. 20305, IF YOUR ADDRESS IS INCORRECT, IF YOU WISH TO BE DELETED FROM THE DISTRIBUTION LIST, OR IF THE ADDRESSEE IS NO LONGER EMPLOYED BY YOUR ORGANIZATION.

UNCLASSIFIED

SECURITY CLASSIFICATION OF THIS PAGE (When Data Entered)

REPORT DOCUMENTATION PAGE		READ INSTRUCTIONS BEFORE COMPLETING FORM
1. REPORT NUMBER DNA 5912Z	2. GOVT ACCESSION NO. AD-A112 497	3. RECIPIENT'S CATALOG NUMBER
4. TITLE (and Subtitle) SOME PHYSICAL AND CHEMICAL ASPECTS OF STRIATION STRUCTURE		5. TYPE OF REPORT & PERIOD COVERED Interim Report for Period 1 Feb 79 - 15 Aug 80
		6. PERFORMING ORG. REPORT NUMBER
7. AUTHOR(s) S. R. Goldman J. L. Sperling		8. CONTRACT OR GRANT NUMBER(s) DNA 001-79-C-0050
9. PERFORMING ORGANIZATION NAME AND ADDRESS JAYCOR P. O. Box 85154 San Diego, CA 92138		10. PROGRAM ELEMENT, PROJECT, TASK AREA & WORK UNIT NUMBERS Subtask S99QAXHC041-24
11. CONTROLLING OFFICE NAME AND ADDRESS Director Defense Nuclear Agency Washington, D.C. 20305		12. REPORT DATE 15 August 1980
		13. NUMBER OF PAGES 116
14. MONITORING AGENCY NAME & ADDRESS(if different from Controlling Office)		15. SECURITY CLASS. (of this report) UNCLASSIFIED
		15a. DECLASSIFICATION DOWNGRADING SCHEDULE N/A since UNCLASSIFIED

16. DISTRIBUTION STATEMENT (of this Report)

Approved for public release; distribution unlimited.

17. DISTRIBUTION STATEMENT (of the abstract entered in Block 20, if different from Report)

18. SUPPLEMENTARY NOTES

This work sponsored by the Defense Nuclear Agency under RDT&E RMSS Code B322080464 S99QAXHC04124 H2590D.

19. KEY WORDS (Continue on reverse side if necessary and identify by block number)

Striation seeding
Late-time striation behavior
Striation diffusion
Chemical effects on striations

20. ABSTRACT (Continue on reverse side if necessary and identify by block number)

In this report we assess a number of physical and chemical processes for their effect on striation structuring, with particular emphasis on times after a nuclear event, but prior to the re-establishment of the undisturbed ambient magnetic field. The results for charge exchange and impact ionization are particularly striking in that slow electron structure in the 100-200 km altitude range, due to fast ions created at an altitude of 400 km, exhibits a sharp decay with decreasing wavelength, at inverse wavenumbers below 20 kilometers.

DD FORM 1 JAN 73 1473 EDITION OF 1 NOV 65 IS OBSOLETE

UNCLASSIFIED

SECURITY CLASSIFICATION OF THIS PAGE (When Data Entered)

PREFACE

We wish to thank Captain Leon Wittwer, USAF, for his strong guidance in suggesting the approach of limiting striation structure at early times through the application of "well-established," non-plasma wave mechanisms.

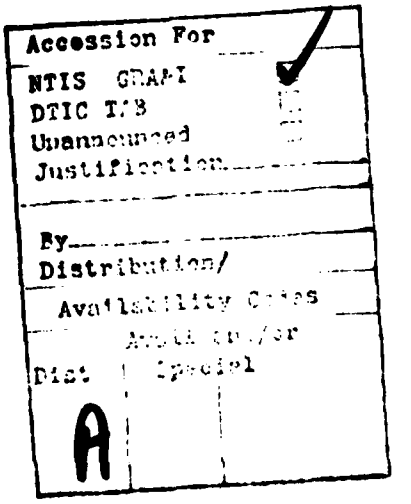

TABLE OF CONTENTS

LIST OF ILLUSTRATIONS

LIST OF ILLUSTRATIONS (Continued)

LIST OF TABLES

1. INTRODUCTION

In this report we assess a number of physical and chemical processes for their effect on striation structuring, with particular emphasis on phenomena present at times after a nuclear event, but prior to the re-establishment of the undisturbed ambient magnetic field. During this time interval the plasma is far from thermal equilibrium, and there are many sources of free energy to drive plasma instabilities. One could attempt a detailed plasma physical description of the phenomenology; such an effort even if theoretically successful would be difficult to verify observationally.

Alternately we have sought to estimate the effect at time t_2 of several physically and chemically "well-established" (e.g., non plasma-wave) mechanisms on structure of specified wavelength and amplitude present at some earlier time, t_1.[1] As time progresses, one expects the plasma free energy (and hence the variety and intensity of instability) to decrease. It is then possible that plasma structure at t_2 can be constructed out of structure present at t_1 which evolves by non plasma-wave processes between t_1 and t_2. If plasma wave processes are completed prior to t_1 it is likely that, at most, they affect structural dynamics from t_1 to t_2 only parametrically.

This approach has the advantage of simplicity and of certainty in the qualitative aspects of its individual chemical and physical components. Upper bounds on each Fourier component of the density structure at t_2 obtain readily when one assumes that the amplitude of the component at t_1 is of order the background density (i.e., relative "perturbations" of order unity).

The values of t_1 and t_2 need not be the same for the various physical and chemical processes invoked to affect structure. In Section 2 we consider the effect of charge exchange and impact ionization on structural decay. In this case t_1 can be the time at which air ionization pick-up is completed at a location at the burst point altitude of the bomb, and t_2 can be the time at which the resulting energetic air ions have completed their conjugate region deposition. (This latter time is generally prior to the relaxation of the magnetic field to its undisturbed state.) In Section 3 we consider the effect of recombination on structural decay. In Section 4 we consider the effect of

Coulomb scattering on structural decay. For these two cases t_1 can be the time at which slow (non suprathermal velocity) ionization is created and t_2 can be the time of re-establishment of the undisturbed magnetic field.

The results for the charge exchange and impact ionization calculations are particularly striking in that slow electron structure in the 100-200 km altitude range due to fast ions created at an altitude of 400 km exhibits a sharp decay with decreasing wavelength at inverse wavenumbers below 20 kilometers (see Figures 11 and 13 for details). Such information provides both qualitative and quantitative inputs, "seeds," for the SCENARIO code.[2]

In addition to the primary results of Sections 2-4, which are summarized in Section 5, a number of additional results relevant to striation decay are presented in Appendices A-C. Appendix A is a theoretical discussion of the relationship between magnetic field diffusion and particle diffusion. This provides background for the calculation of Section 4. Appendix B is a discussion of slow ionization production by 12 keV O^+ ions, as occurring in magnetic storms. Appendix C presents new results on the suppression of anomalous diffusion in late time striation structure by ionospheric electric fields.

2. THE DECAY OF HIGH ENERGY IONIZED STRUCTURE THROUGH CHARGE EXCHANGE AND IMPACT IONIZATION

The undisturbed ionosphere is a complex mixture of charged and neutral particle species. One way in which a nuclear detonation can modify this composition is through the generation of ions and neutrals with energies of the order of 10 or even 100 keV. Once formed, the fast, high energy neutrals are transformed into ions by impact ionization.[3] Between charge exchange and impact ionization events, high energy ions and neutrals can increase the thermal charged particle density of the ionosphere through ionization collisions. Eventually, a sufficiently large number of collisions occur so that the initially high energy particles become part of the thermal background.

The purpose of this section is to quantify the degree to which an initial structure consisting of high energy ions is degraded as it flows down field lines into denser portions of the ionosphere and to determine the density of thermal ionization formed as a result of ionization by high energy ions and neutrals. As the basis for determining the density of high energy ions and neutrals as a function of time, the following equations have been solved:

$$\frac{\partial n_1(\vec{r},t)}{\partial t} = -\nu_1(t)n_1(\vec{r},t) + \nu_2(t)n_2(\vec{r},t) \qquad (1a)$$

$$\frac{\partial n_2(\vec{r},t)}{\partial t} = -\nu_2(t)n_2(\vec{r},t) + \nu_1(t)n_1(\vec{r},t) - \nu_0(t)n_2(\vec{r},t) \quad . \qquad (1b)$$

Here,

$n_1(\vec{k},t)$ = high energy ion density

$n_2(\vec{k},t)$ = high energy neutral density

$\nu_1(t)$ = rate at which high energy ions are destroyed and high energy neutrals are created as a function of time

$\nu_2(t)$ = rate at which high energy neutrals are destroyed and high energy ions are created as a function of time

$\nu_0(t)$ = rate at which high energy neutral structure is lost by convection or diffusion.

Writing the spatial structure of $n_1(\vec{r},t)$ and $n_2(\vec{r},t)$ in terms of Fourier integrals,

$$n_1(\vec{r},t) = \int_{-\infty}^{\infty} d^3k\, n_1(\vec{r},t)\, \exp(ikx) \tag{2a}$$

$$n_2(\vec{r},t) = \int_{-\infty}^{\infty} d^3k\, n_2(\vec{r},t)\, \exp(ikx) \tag{2b}$$

permits Eqs. (1a) and (1b) to be rewritten in the following way:

$$\left[\frac{\partial}{\partial t} + \nu_1(t)\right]\ n_1(\vec{k},t) = \nu_2(t) n_2(\vec{k},t) \tag{3a}$$

$$\left[\frac{\partial}{\partial t} + \nu_2(t) + \nu_0(t)\right]\ n_2(\vec{k},t) = \nu_1 n_1(\vec{k},t) \quad . \tag{3b}$$

In writing Eqs. (1) and (3) a term for ions comparable to ν_0 for neutrals has not been included since structure dimensions larger than an ion gyroradius are assumed. Furthermore, the spatial dependence of ν_0, ν_1, and ν_2 on the coordinate orthogonal to the field lines has been neglected. This assumption is reasonable if the spatial variation of the parameters orthogonal to the field line is neglected and the evaluation of the equations is in a frame of reference moving along the field lines for a particular velocity space class of ions. Hence, the solution to Eqs. (1) and (3) depends upon the ion velocity considered.

Two forms for ν_0 have been chosen. For the case when the neutral mean free path is smaller than the characteristic dimensions of structure a diffusion form for ν_0 is chosen. In Fourier space:[4]

$$\nu_0 = k^2 v_{n\perp}{}^2/3\nu_2 \tag{4}$$

where $v_{n\perp}$ is the component of neutral velocity perpendicular to the magnetic field lines. For neutral mean free paths larger than structure dimensions the diffusion approximation is not valid and ν_0 represents a convective loss:[4]

$$\nu_0 = k\, v_n/8 \tag{5}$$

where v_n is the fast neutral speed and the relation

$$\Delta x\, \Delta k = \tfrac{1}{2} \tag{6}$$

for a Gaussian profile has been used.

In addition to changing form as either fast ions or fast neutrals, the fast particles ionize the cold neutral background and thereby increase the number of slow ions and electrons. The expressions giving the rate of slow electron or positive ionization are

$$\frac{dn_e(\vec{k},t)}{dt} = n_1(\vec{k},t) \sum_s \nu_s(t) n_s(t) + n_2(\vec{k},t) \sum_s \nu_s'(t) n_s(t) \tag{7a}$$

$$\frac{dn_+(\vec{k},t)}{dt} = n_1(\vec{k},t) \sum_s \bar{\nu}_s'(t) n_s(t) + n_2(\vec{k},t) \sum_s \bar{\nu}_s'(t) n_s(t) \tag{7b}$$

where

$n_e(\vec{k},t)$ = slow electron density

$n_+(\vec{k},t)$ = slow ion density

$\nu_s(t)$ = collision frequency for slow electron production due to fast ion collisions with species s

$\nu_s'(t)$ = collision frequency for slow ion production due to fast neutral collisions with species s

$\bar{\nu}_s(t)$ = collision frequency for slow positive ion production due to fast ion collisions with species s

$\bar{\nu}_s'(t)$ = collision frequency for slow positive ion production due to fast neutral collisions with species s

In writing Eqs. (7a) and (7b) the spatial variation orthogonal to the magnetic field of $\nu_s(t)$, $\nu_s'(t)$, $\bar{\nu}_s(t)$, $\bar{\nu}_s'(t)$, and n_s has been neglected.

Eqs. (3a) and (3b) have been solved with $\vec{k}$ assumed to be one-dimensional and just after a nuclear detonation when the ionosphere is strongly modified. MRC code results[5] and CIRA tables[6] have been used as the basis for quantifying the solutions assuming that the fast, high energy species is monatomic oxygen. Also, Reference 3 has been used to evaluate the collision frequencies and ν_0.

In subsection 2.1 calculations are first shown for the 400 km burst altitude Starfire VER238 simulation with vertical magnetic field lines, and then (assuming negligible change in the ionization background) for the same burst with magnetic field lines making an angle of 52.7^0 with the vertical. In subsection 2.2 calculations are shown for the 600 km burst altitude TB600 MRC simulation. In subsection 2.3 calculations are shown for the 200 km altitude LITTLE ONE simulation. Comparison of the results of the various subsections gives insight into the variables affecting ionization deposition and structural degradation.

Magnetic field and background density variation used in subsection 2.1 is shown in Figures 1 and 2. The variables for subsections 2.2 and 2.3 are shown in Figures 3 and 4, and 5 and 6, respectively. Figures 1-6 are microfiche output associated with Reference 5.

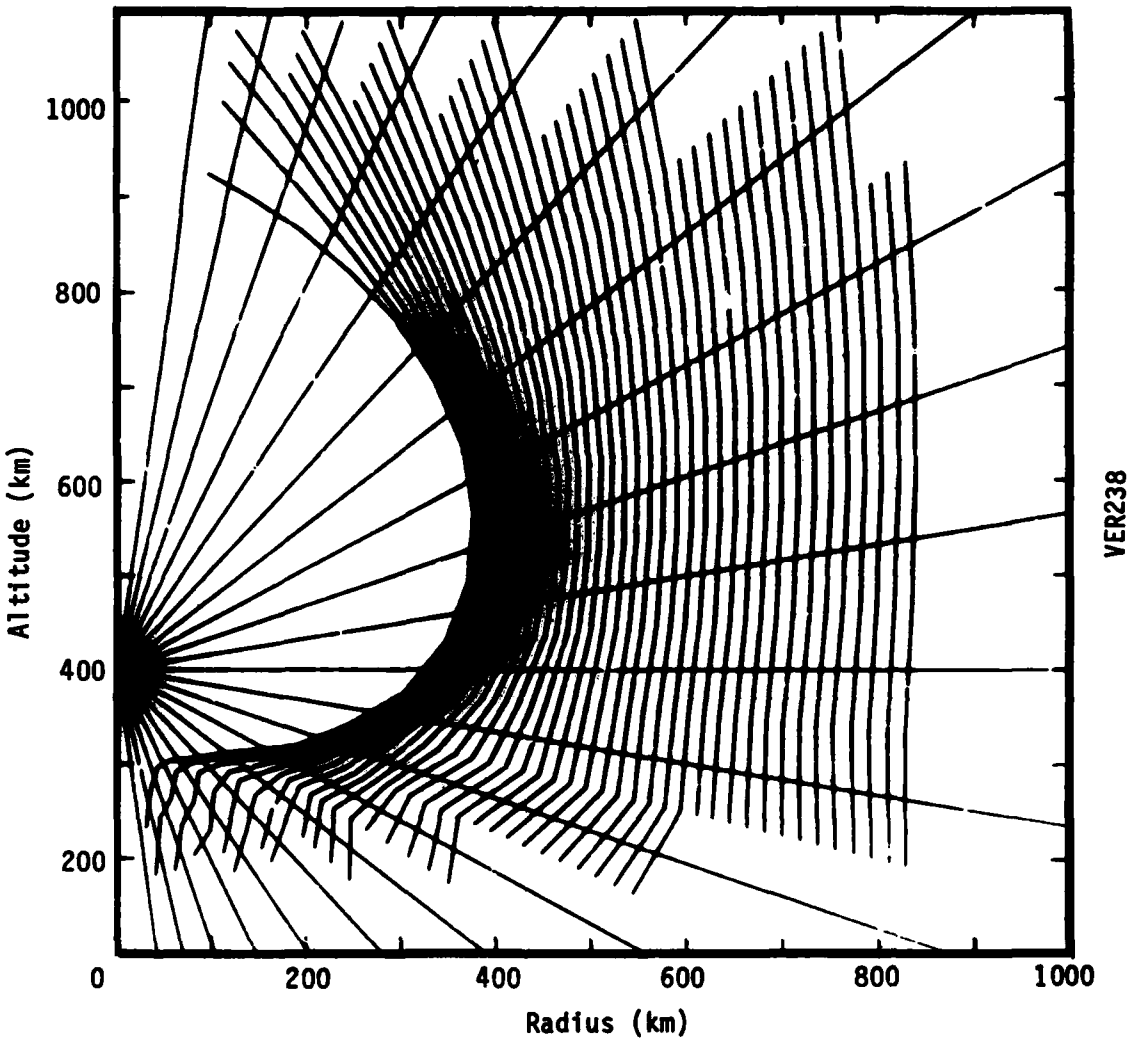

Figure 1. Magnetic field geometry for the 400 km altitude Starfish VER238 simulation. Fast ions were assumed to originate at 400 km altitude and to move down along a magnetic field line passing through the region of magnetic field compression.

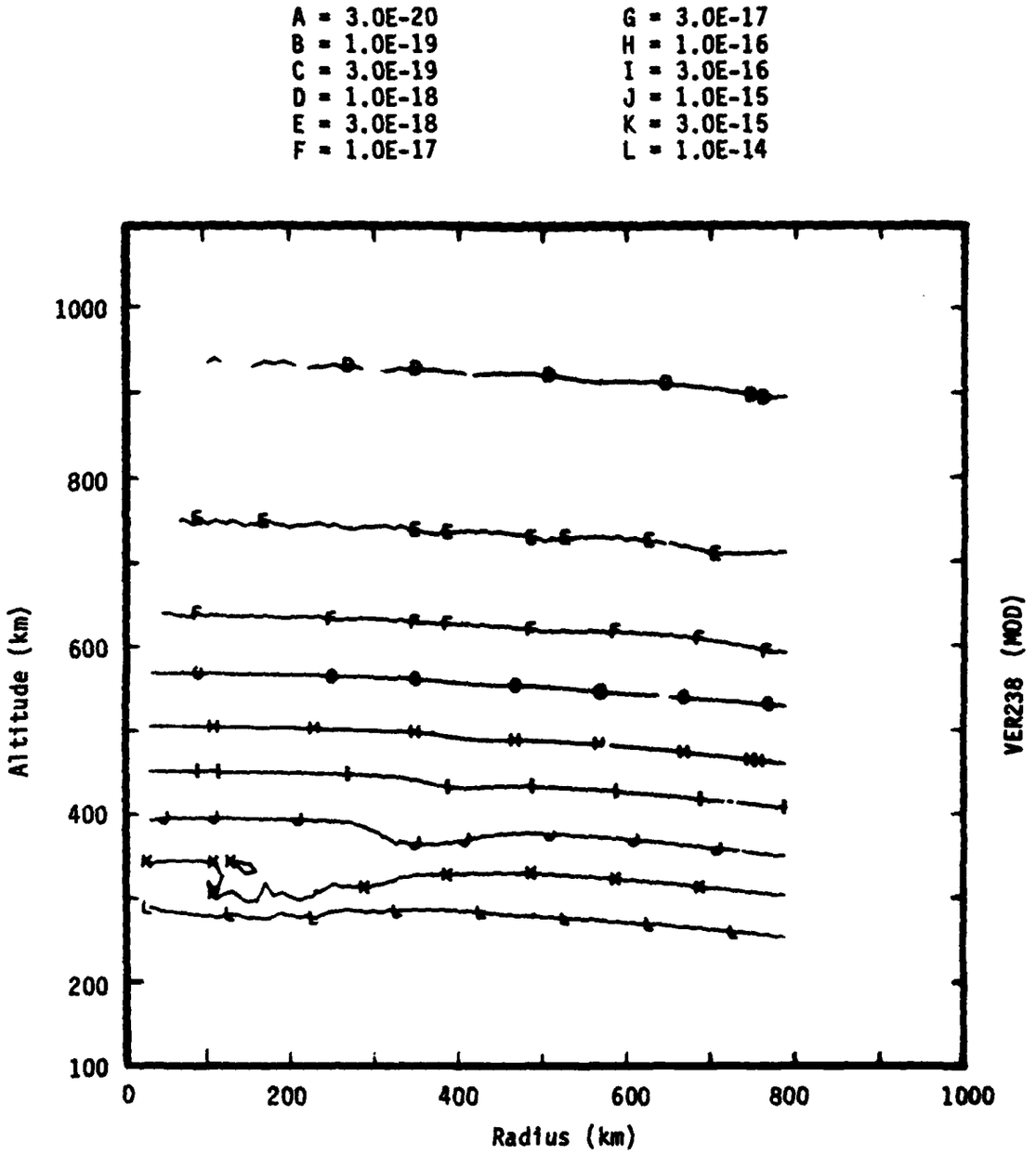

Figure 2. The cold neutral background appropriate to the 400 km altitude Starfish VER238 simulation.

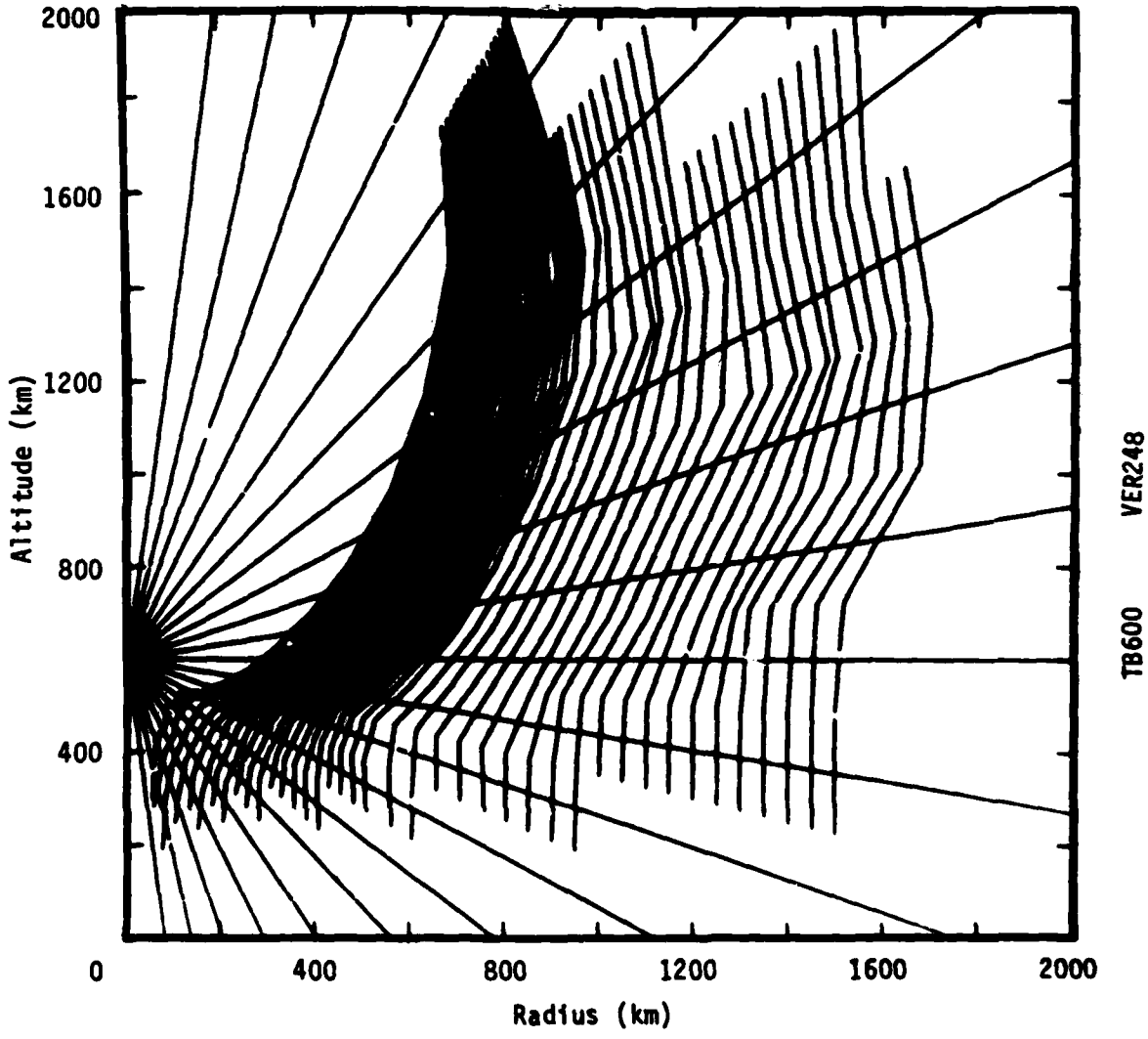

Figure 3. Magnetic field geometry for the 600 km TB600 MRC simulation. Fast ions were assumed to originate at 600 km altitude and to move down along a magnetic field line passing through the region of magnetic field compression.

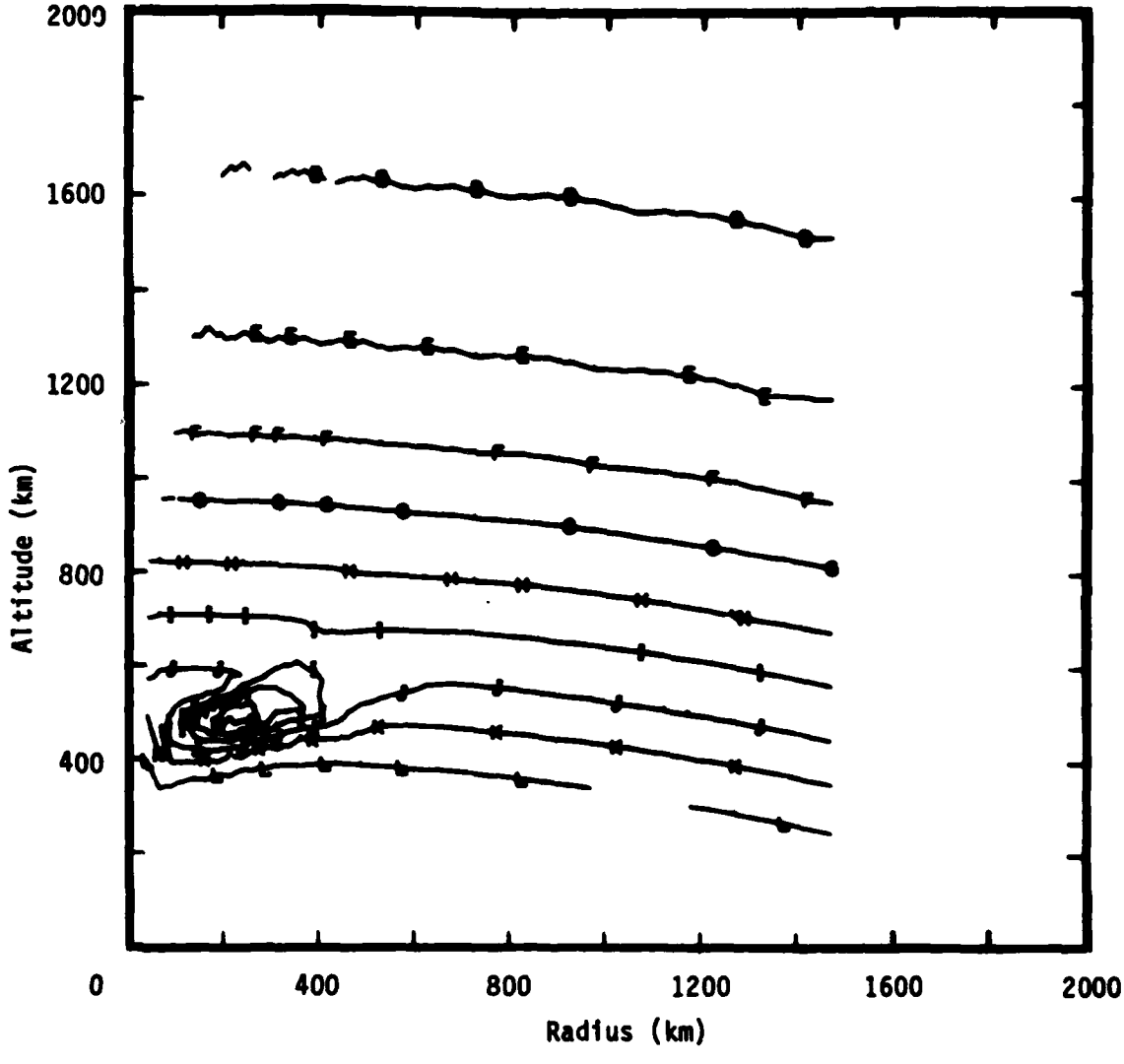

Figure 4. The cold neutral background appropriate to the 600 km TB600 MRC simulation.

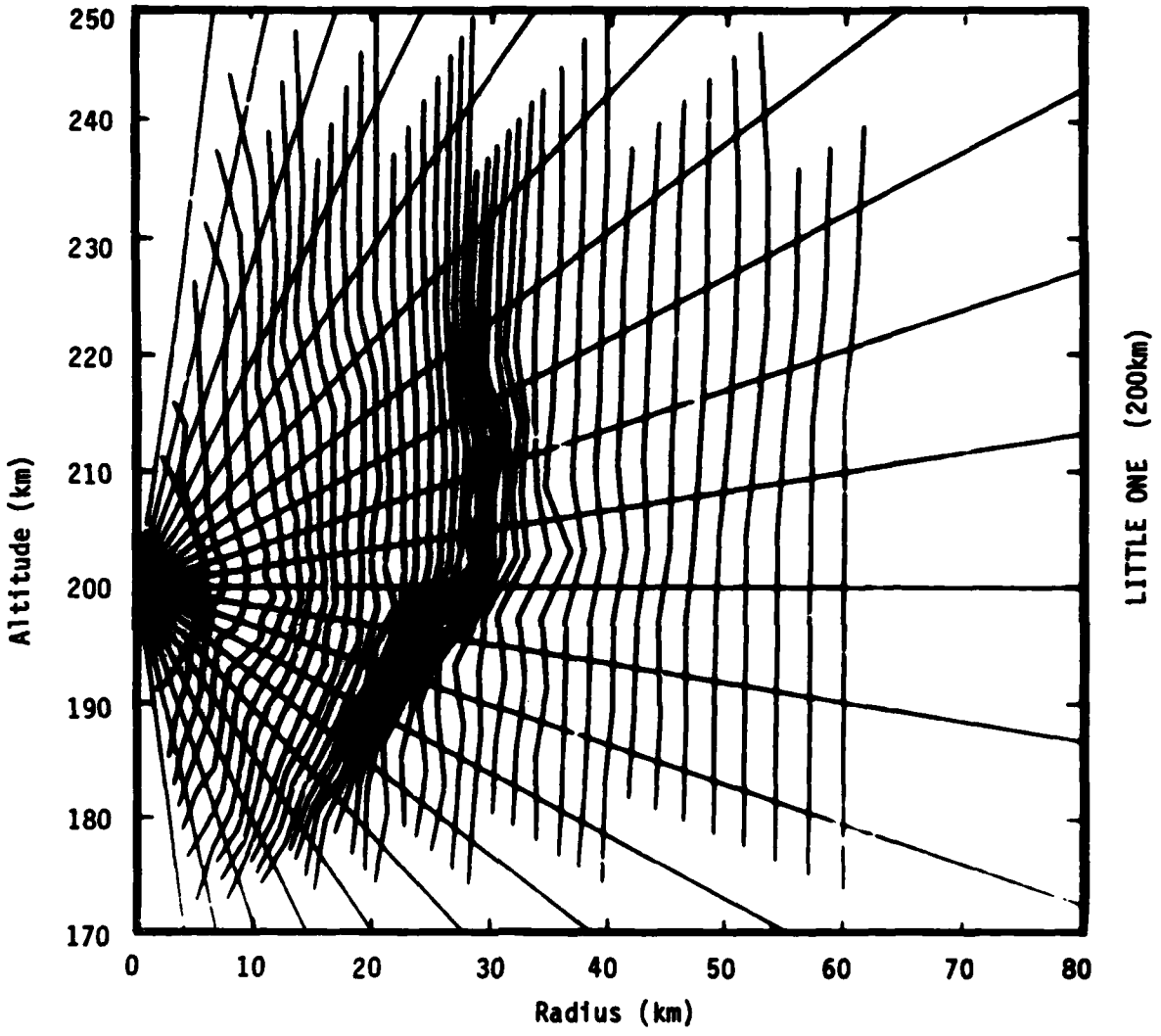

Figure 5. Magnetic field geometry for the 200 km Little One simulation.

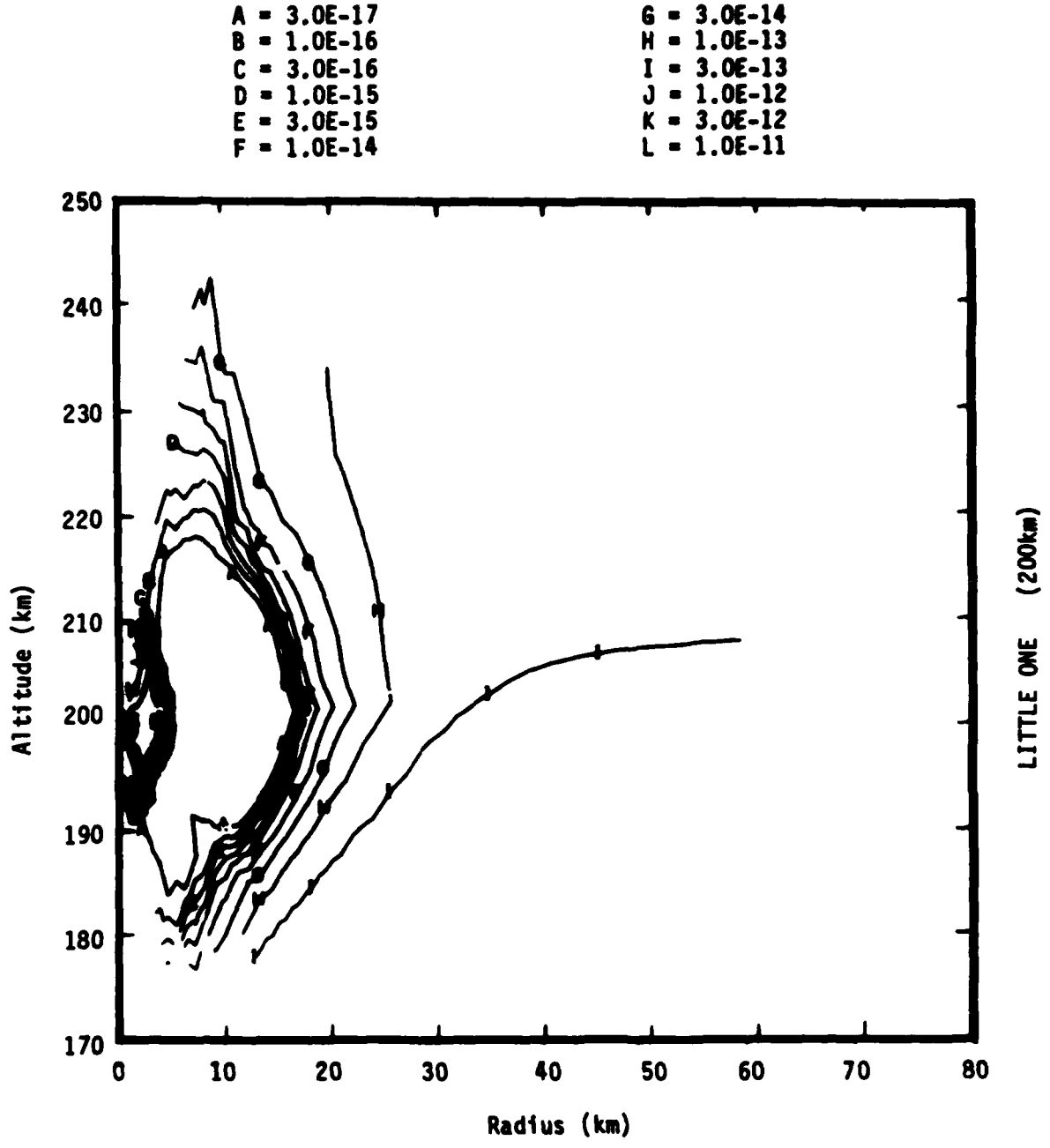

Figure 6. The cold neutral background appropriate to the 200 km Little One simulation. For this simulation, with (roughly) constant cold neutral mass density at altitude below 200 km along a magnetic field line, particles were assumed to move along the cold neutral mass density contour for 3.0×10^{-15} gm/cm^3.

2.1 400 KM

Based on the MRC simulation of STARFISH at 400 km and the geometry of Figures 1 and 2, calculations have been carried out to determine the impact of charge exchange and impact ionization on the decay of fast ionized structure moving down field lines. Also, the slow electron and ion generation resulting from ionization by fast ions and neutrals has been evaluated. The only differences with the calculations of Section 2.2, q.v., are that the calculations for STARFISH were started at 400 km and the CIRA atmosphere chosen was appropriate to STARFISH. The results are tabulated in Tables 1 and 2 and Figures 7 to 14. Table 1 shows the slow ionization density produced by fast particles derived from the original fast ion for an inverse wave number of 500 km. Results are presented for electrons and ion produced by 160 keV and 30 keV ions and neutrals. Table 2 shows the field line integrated production of slow electrons and ions as a function of inverse wavenumber for both 160 keV and 30 keV cases.

Figures 7 to 9 show fast ion and fast neutral density as functions of wavenumber and altitude (or time). Figure 10 shows the inverse wavenumber variation of fast ions and neutrals at an altitude of 110 km. Figures 11 and 12 show respectively the slow electron and slow positive ion production at specified wavenumbers relative to the production for inverse wavenumber of 500 km by fast particles at 160 keV. Hence the curves are indications of the relative values of Fourier components of density structure if one assumes a 500 km scale length background. For a background of smaller scale length the ordinate for the same abscissa would be greater. Figures 13 and 14 are similar to 11 and 12 but for fast particles of 30 keV.

The qualitative results are similar to those of Section 2.2; however, because of the different cold neutral atmospheres, there is a greater degree of slow ionization at relatively short wavelengths (e.g., 5 km) produced by the STARFISH than for the 600 km burst (Tables 2 and 4). Note also that slow electron and ion production for short wavelengths is greater for 160 keV particles than for 30 keV particles.

The MRC simulation assumes that the magnetic field is aligned with gravity. However, the magnetic field lines in the real ionosphere actually

Table 1. The slow electron production by 160 keV particles, $n_e^{160}(k_o)$, the slow ion production by 160 keV particles, $n_+^{160}(k_o)$, the slow electron production by 30 keV particles, $n_e^{30}(k_o)$, and the slow ion production by 30 keV particles, $n_+^{30}(k_o)$, are tabulated as a function of altitude. $k_0 = 1/500\ km^{-1}$. All quantities are in units of particles/cm per single fast ion at 400 km altitude.

H(km)	$n_e^{160}(k_o) \times 10^6$	$n_+^{160}(k_o) \times 10^6$	$n_e^{30}(k_o) \times 10^6$	$n_+^{30}(k_o) \times 10^6$
400	3.5×10^{-3}	3.6×10^{-2}	1.5×10^{-3}	2.9×10^{-3}
390	7.0×10^{-3}	4.6×10^{-2}	3.2×10^{-3}	4.3×10^{-3}
380	1.1×10^{-2}	5.3×10^{-2}	5.3×10^{-3}	5.4×10^{-3}
370	1.9×10^{-2}	6.6×10^{-2}	9.0×10^{-3}	7.7×10^{-3}
360	2.9×10^{-2}	7.7×10^{-2}	1.3×10^{-2}	9.2×10^{-3}
350	4.6×10^{-2}	9.5×10^{-2}	2.1×10^{-2}	1.2×10^{-2}
340	6.5×10^{-2}	1.1×10^{-1}	3.0×10^{-2}	1.4×10^{-2}
330	9.7×10^{-2}	1.4×10^{-1}	4.4×10^{-2}	1.8×10^{-2}
320	1.3×10^{-1}	1.6×10^{-1}	5.8×10^{-2}	2.0×10^{-2}
310	1.9×10^{-1}	2.0×10^{-1}	8.1×10^{-2}	2.6×10^{-2}
300	2.5×10^{-1}	2.5×10^{-1}	1.0×10^{-1}	3.0×10^{-2}
290	3.4×10^{-1}	3.2×10^{-1}	1.4×10^{-1}	4.1×10^{-2}
280	4.6×10^{-1}	4.3×10^{-1}	1.8×10^{-1}	5.8×10^{-2}
270	6.3×10^{-1}	5.9×10^{-1}	2.3×10^{-1}	8.5×10^{-2}
260	8.8×10^{-1}	8.0×10^{-1}	3.1×10^{-1}	1.3×10^{-1}
250	1.2×10^{0}	1.1×10^{0}	4.1×10^{-1}	1.9×10^{-1}
240	1.7×10^{0}	1.6×10^{0}	5.6×10^{-1}	2.9×10^{-1}
230	2.5×10^{0}	2.2×10^{0}	7.6×10^{-1}	4.3×10^{-1}
220	3.6×10^{0}	3.2×10^{0}	1.0×10^{0}	6.6×10^{-1}
210	5.3×10^{0}	4.6×10^{0}	1.4×10^{0}	1.0×10^{0}
200	7.8×10^{0}	6.8×10^{0}	2.1×10^{0}	1.6×10^{0}
190	1.2×10^{1}	1.0×10^{1}	3.0×10^{0}	2.4×10^{0}
180	1.8×10^{1}	1.6×10^{1}	4.4×10^{0}	3.9×10^{0}
170	3.0×10^{1}	2.5×10^{1}	6.8×10^{0}	6.4×10^{0}
160	4.9×10^{1}	4.2×10^{1}	1.1×10^{1}	1.1×10^{1}
150	8.6×10^{1}	7.3×10^{1}	1.8×10^{1}	1.9×10^{1}
140	1.6×10^{2}	1.4×10^{2}	3.4×10^{1}	3.7×10^{1}
130	3.6×10^{2}	3.1×10^{2}	7.3×10^{1}	8.2×10^{1}
120	1.0×10^{3}	8.4×10^{2}	1.8×10^{2}	2.3×10^{2}

Table 2. The total production (per single fast ion) of slow electrons and ions between 400 and 110 km is tabulated as a function of inverse wavenumber.

k^{-1}(km)	$n_{eT}^{160}(k)$	$n_{+T}^{160}(k)$	$n_{eT}^{30}(k)$	$n_{+T}^{30}(k)$
5	8.0×10^{1}	6.9×10^{1}	8.5×10^{-1}	9.6×10^{-1}
20	9.3×10^{2}	7.8×10^{2}	8.8×10^{1}	9.8×10^{1}
100	1.7×10^{3}	1.4×10^{3}	3.0×10^{2}	3.0×10^{2}
500	1.7×10^{3}	1.5×10^{3}	3.4×10^{2}	4.0×10^{2}

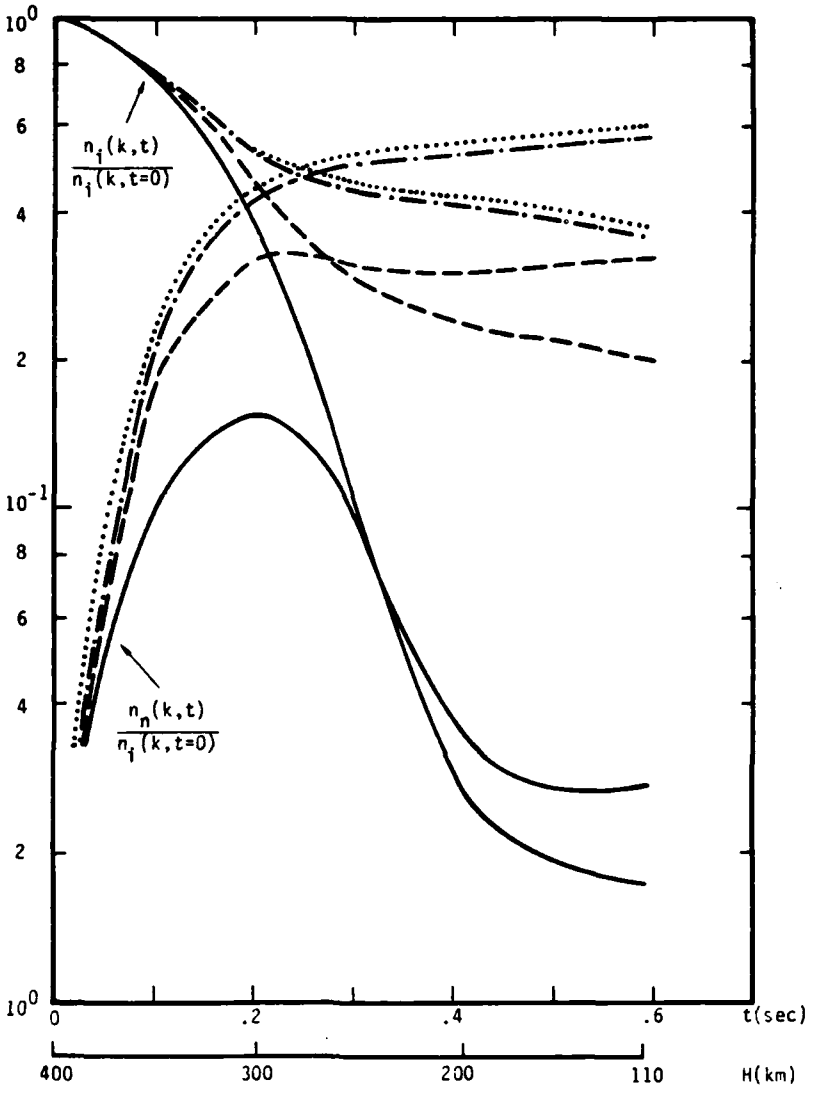

Figure 7. For 160 keV particles, the fast ion density as a function of wavenumber and time, $n_i(k,t)$, and the fast neutral density as a function of wavenumber and time, $n_n(k,t)$, are normalized to the initial fast ion density at time, t = 0 sec, and altitude of 400 km, and plotted versus time, t(sec), and altitude, H(km). The initial neutral density is zero. The different types of lines used in the figure represent different wavelengths: k^{-1} = 5 km ———, = 20 km - - -, = 100 km — · —, and = 500 km ·····.

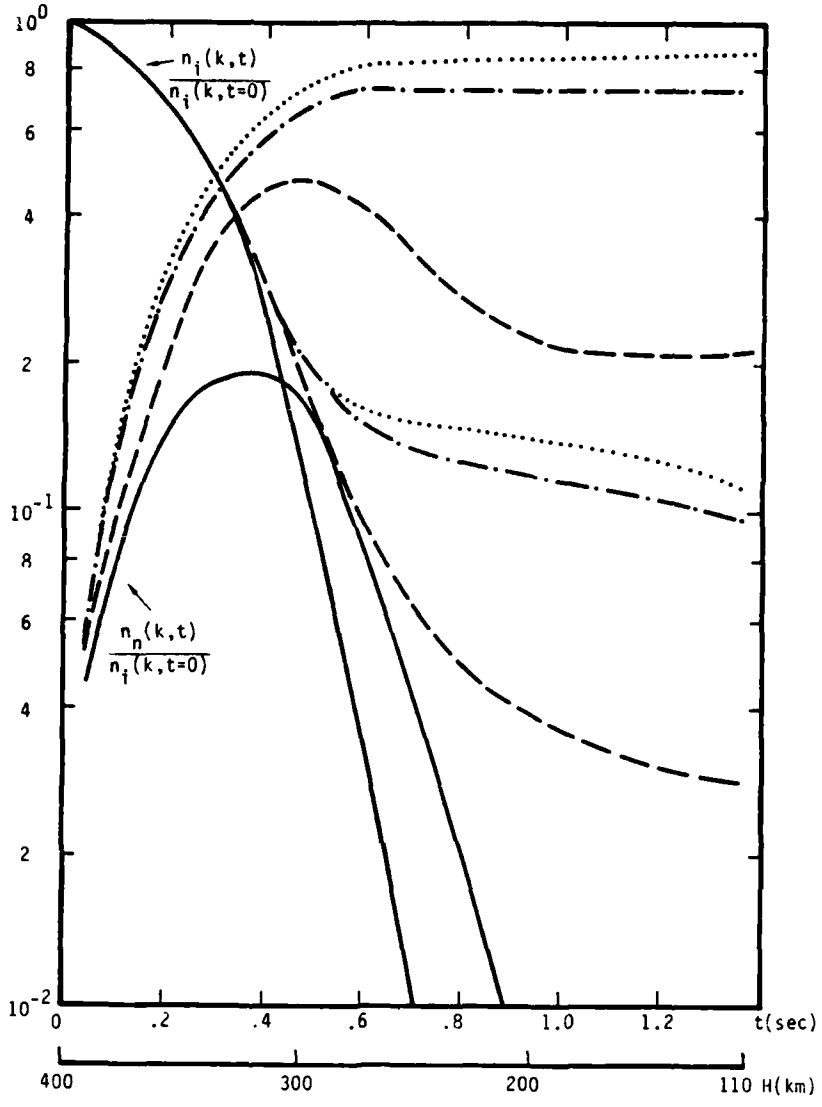

Figure 8. For 30 keV particles, the fast ion density as a function of wavenumber and time, $n_i(k,t)$, and the fast neutral density as a function of wavenumber and time, $n_n(k,t)$, are normalized to the initial fast ion density at time, t = 0 sec, and altitude of 400 km, and plotted versus time, t(sec), and altitude, H(km). The initial neutral density is zero. The different types of lines used in the figure represent different wavelengths: k^{-1} = 5 km ———, = 20 km - - -, = 100 km — · — , and = 500 km ·····.

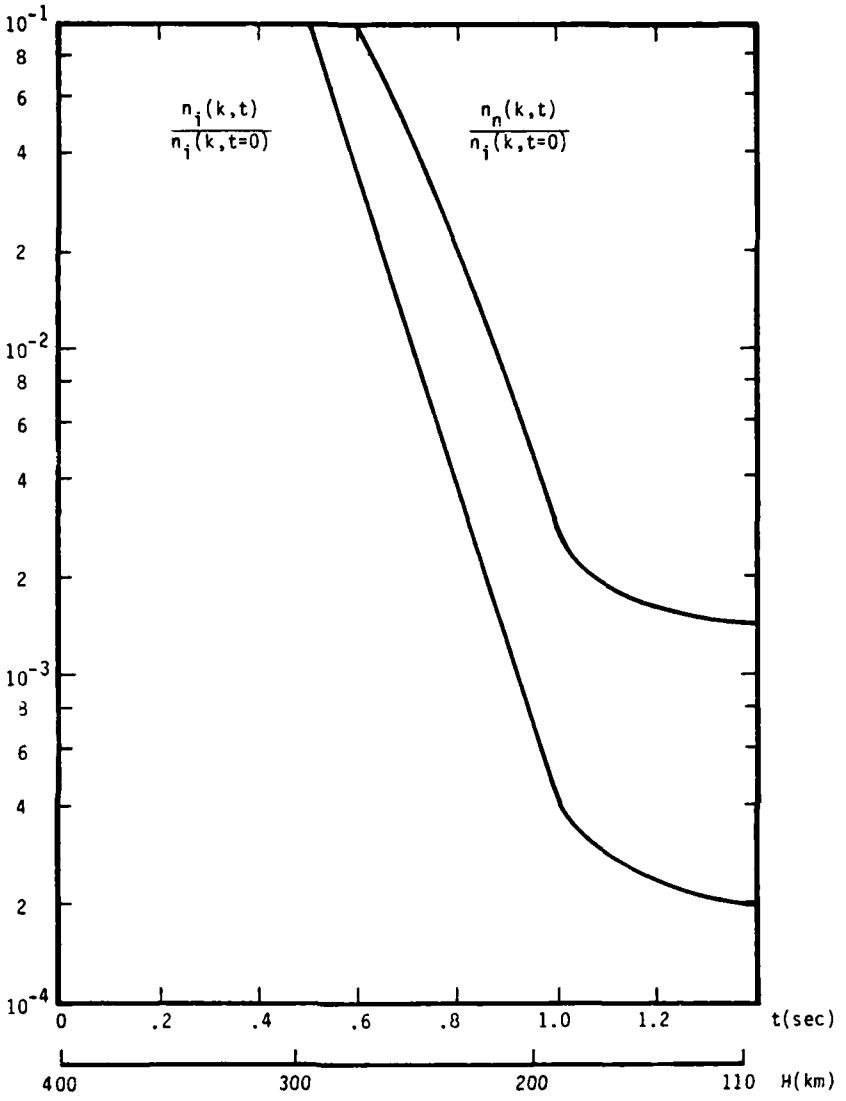

Figure 9. For 30 keV particles, the fast ion density as a function of wavenumber and time, $n_i(k,t)$, and the fast neutral density as a function of wavenumber and time, $n_n(k,t)$, are normalized to the initial fast ion density at time, t = 0 sec, and altitude of 400 km, and plotted versus time, t(sec), and altitude, H(km). The initial neutral density is zero. The different types of lines used in the figure represent different wavelengths: k^{-1} = 5 km ——— , = 20 km - - - , = 100 km — · — , and = 500 km ·····.

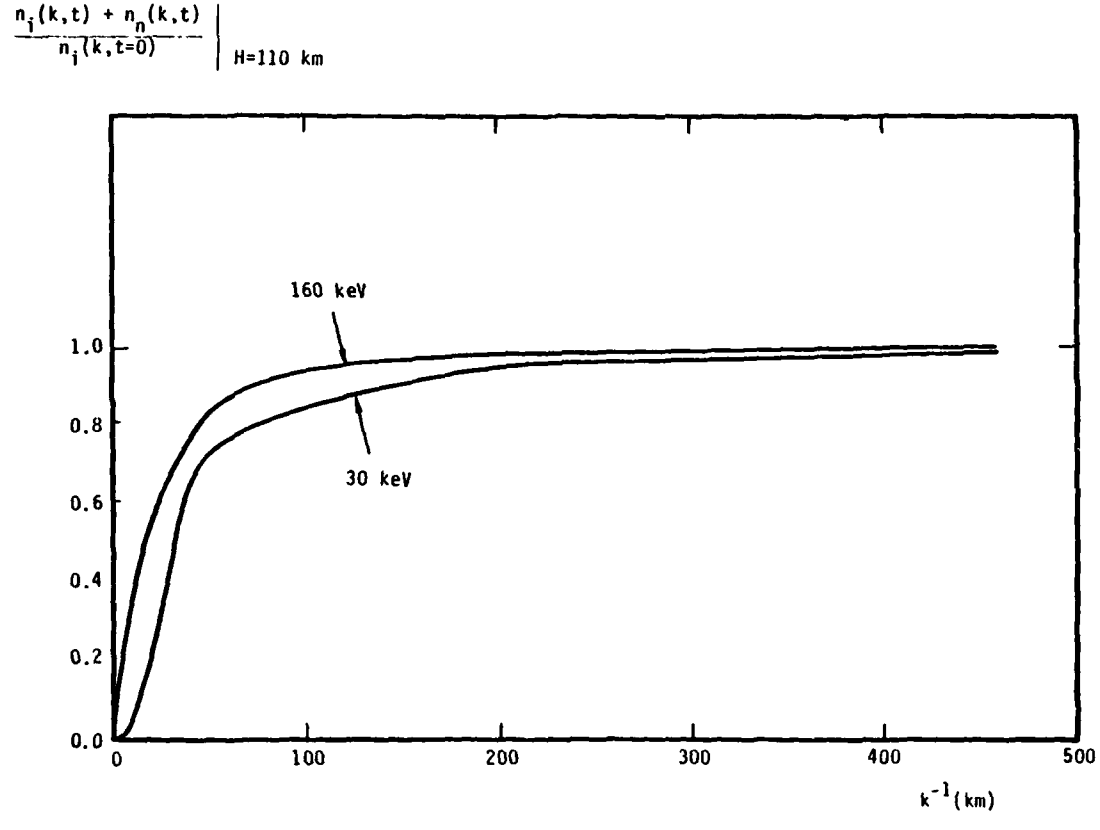

Figure 10. The total fast ion and fast neutral density at H = 110 km normalized to the initial fast ion density versus inverse wavenumber in kilometers.

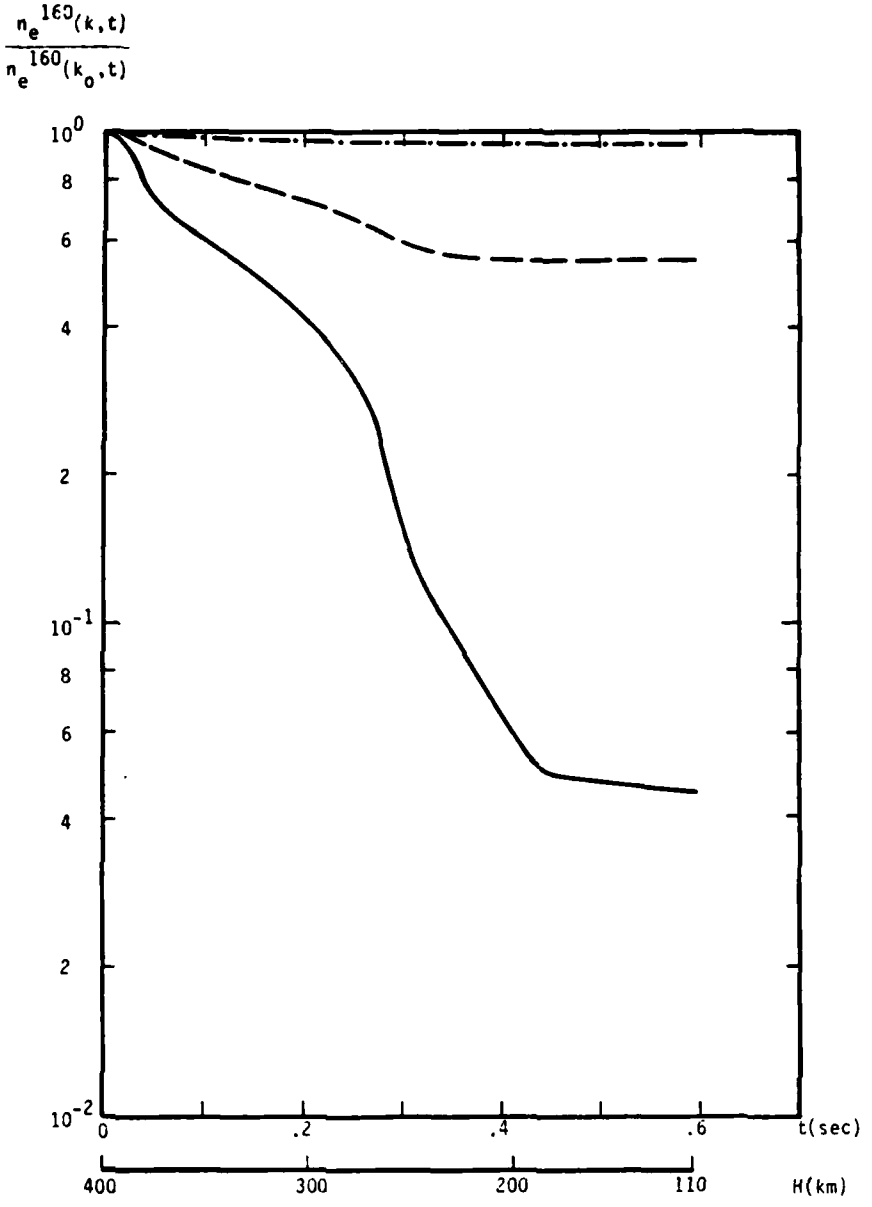

Figure 11. For 160 keV particles, the slow electron production as a function of wavenumber and time is normalized to the corresponding quantity in Table 1 (k_o^{-1} = 500 km) and plotted versus altitude, H(km), and time, t(sec). The different types of lines in the figure represent different wavenumbers: k^{-1} = 5 km ———, = 20 km - - -, = 100 km — • —•

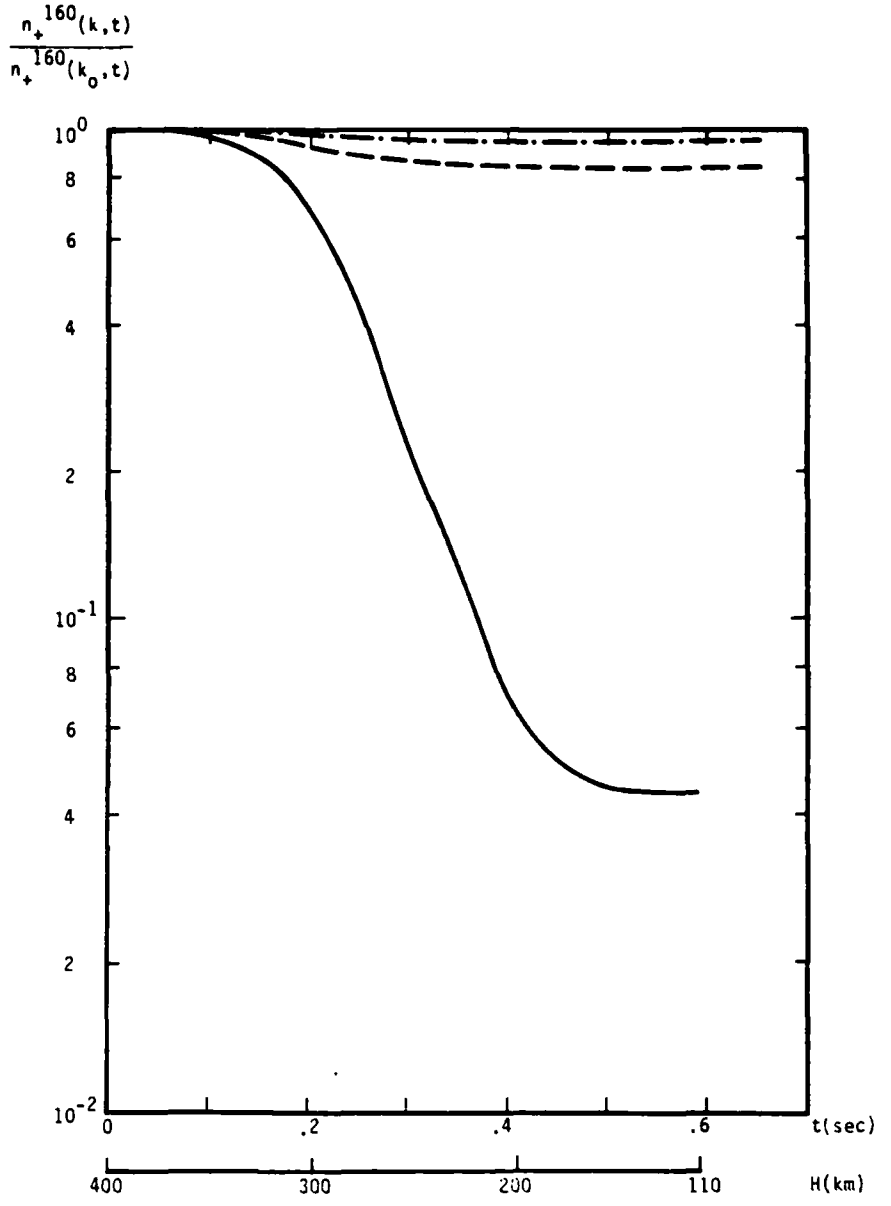

Figure 12. For 160 keV particles, the slow positive ion production as a function of wavenumber and time is normalized to the corresponding quantity in Table 1 (k_o^{-1} = 500 km) and plotted versus altitude, H(km), and time, t(sec). The different types of lines in the figure represent different wavenumbers: k^{-1} = 5 km ———, = 20 km - - -, = 100 km —·—·

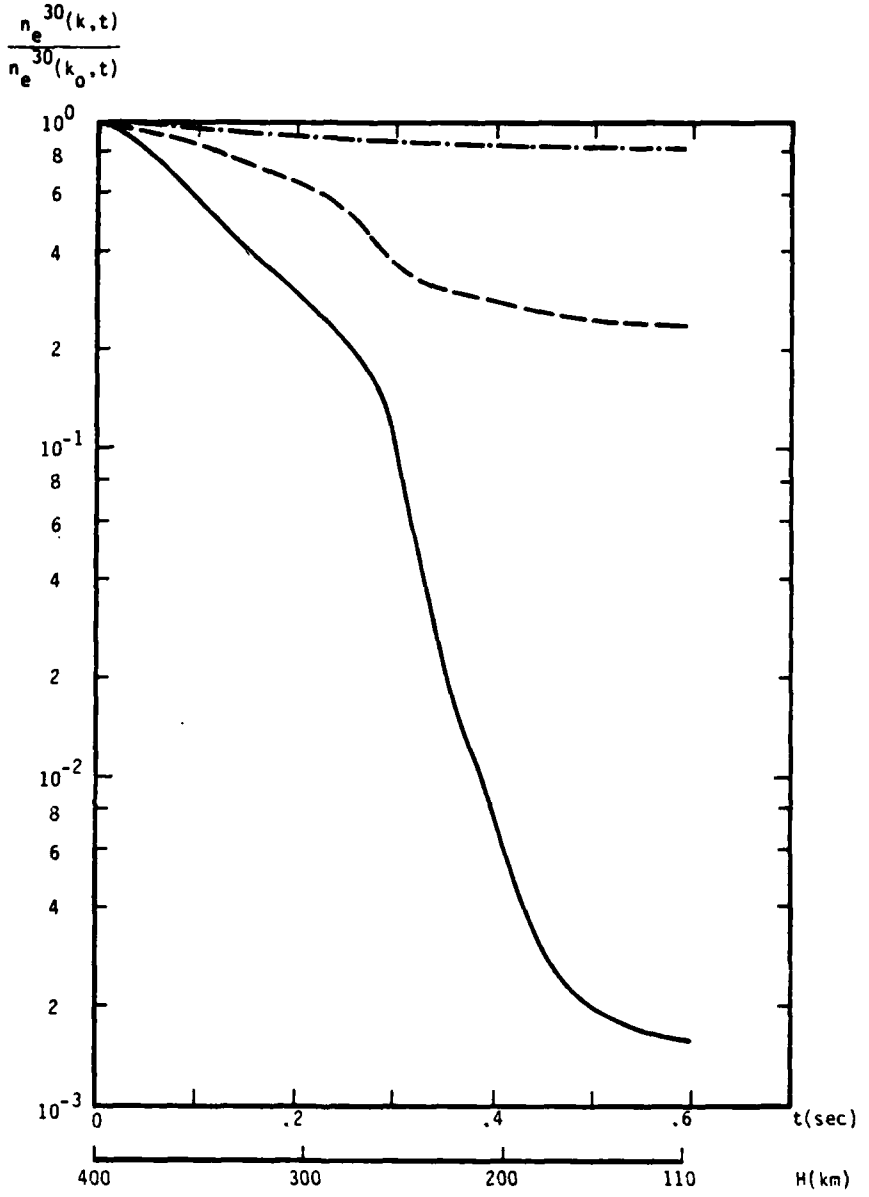

Figure 13. For 30 keV particles, the fast electron production as a function of wavenumber and time is normalized to the corresponding quantity in Table 1 (k_o^{-1} = 500 km) and plotted versus altitude, H(km), and time, t(sec). The different types of lines in the figure represent different wavenumbers: k^{-1} = 5 km ———, = 20 km - - -, = 100 km — ·— ·

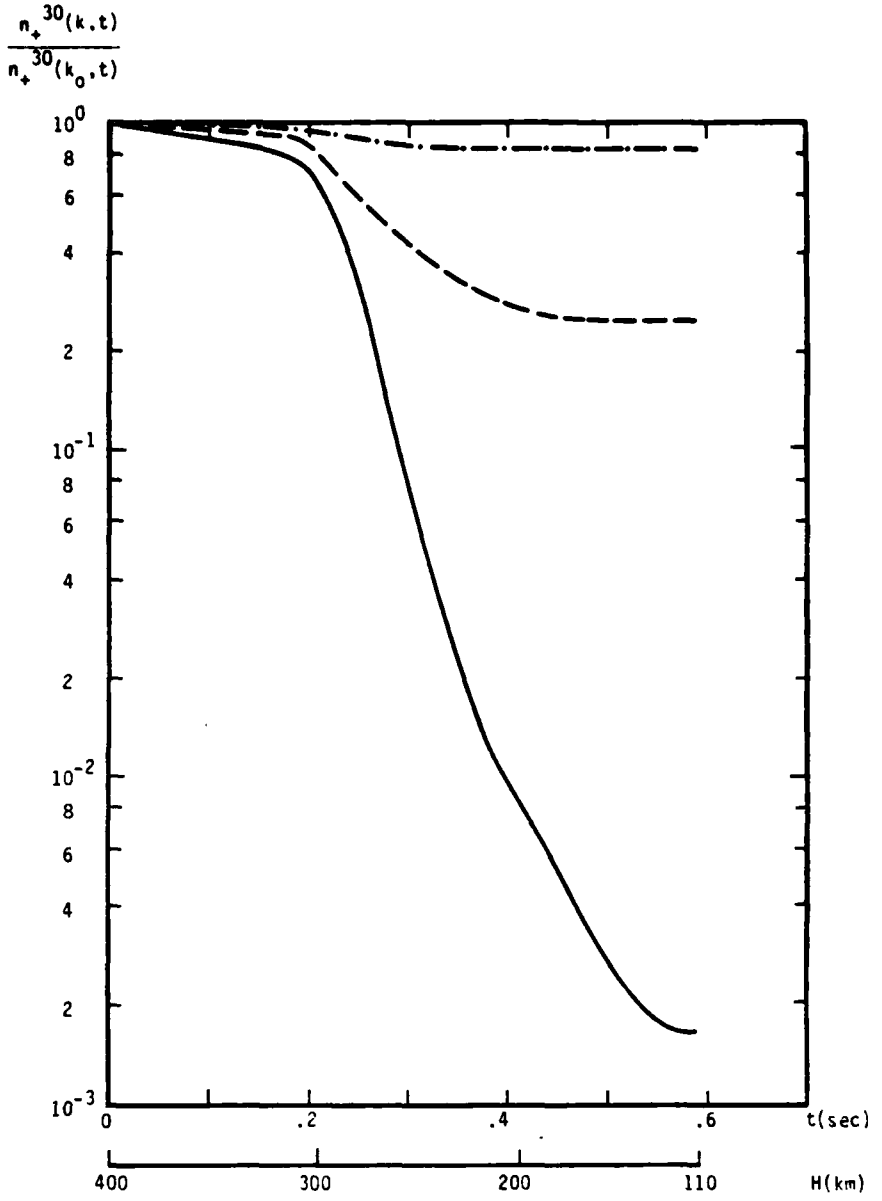

Figure 14. For 30 keV particles, the fast ion production as a function of wavenumber and time is normalized to the corresponding quantity in Table 1 (k_o^{-1} = 500 km) and plotted versus altitude, H(km), and time, t(sec). The different types of lines in the figure represent different wavenumbers: k^{-1} = 5 km ———, = 20 km - - -, = 100 km —·—·

make an oblique angle with gravity. To determine the effect of magnetic field geometry on slow electron and ion production, the relative production rates of slow electrons and ions for magnetic field lines which make a realistic angle of 52.7^{o} with gravity have been calculated. The production rates for slow ions and electrons for this angle have been plotted in Figures 15 to 17 for three altitudes (i.e., 250, 200, and 150 km, respectively) relative to the production rates for magnetic field lines which are aligned with gravity. The figures indicate that the slow particle production rates are decreased for the oblique angles, especially for larger wavelengths and lower altitudes primarily because with oblique angles there is more time for the neutral convective or diffusive loss processes to decrease the number of particles available for slow particle production.

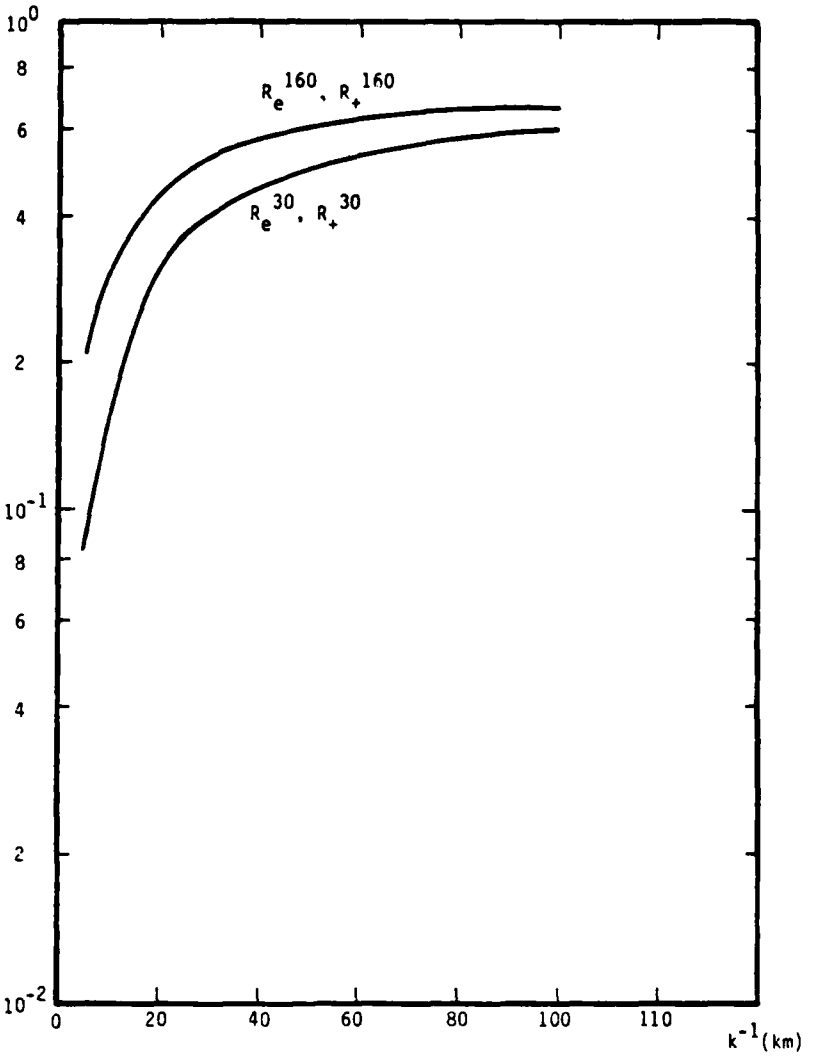

Figure 15. The rates of slow electron and ion production by 160 and 30 keV particles for magnetic field lines at an angle of 52.7° with the vertical relative to production rates for magnetic field lines at an angle of 0° with the vertical [i.e., $Re^{160} = ne^{160}_{+}(\theta = 52.7)/ne^{160}_{+}(\theta = 0)$, $Re^{30}_{+} = ne^{30}_{+}(\theta = 52.7)/ne^{30}_{+}(\theta = 0)$] are plotted versus inverse wavenumber at an altitude of 250 km. The initial ion and neutral densities at 400 km altitude are taken to be 1 and 0, respectively.

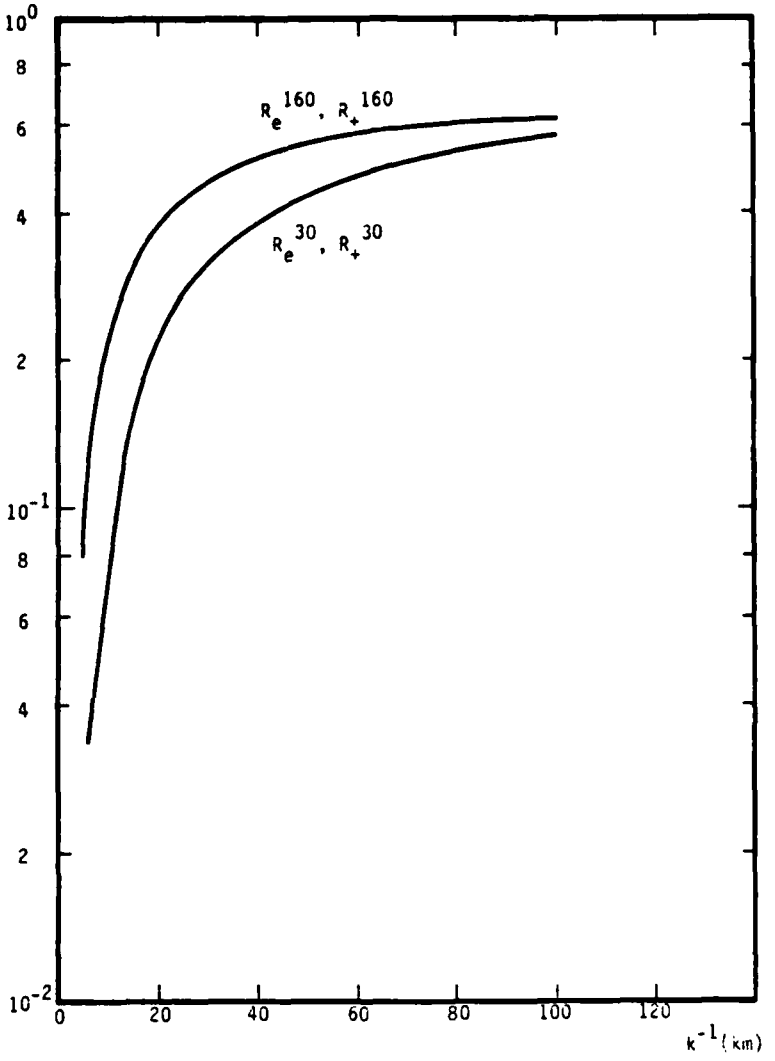

Figure 16. The rates of slow electron and ion production by 160 and 30 keV particles for magnetic field lines at an angle of 52.7° with the vertical relative to production rates for magnetic field lines at an angle of 0° with the vertical [i.e., $Re^{160} = ne^{160}_{+}(\theta = 52.7)/ne^{160}_{+}(\theta = 0)$, $Re^{30}_{+} = ne^{30}_{+}(\theta = 52.7)/ne^{30}_{+}(\theta = 0)$] are plotted versus inverse wavenumber at an altitude of 200 km. The initial ion and neutral densities at 400 km altitude are taken to be 1 and 0, respectively.

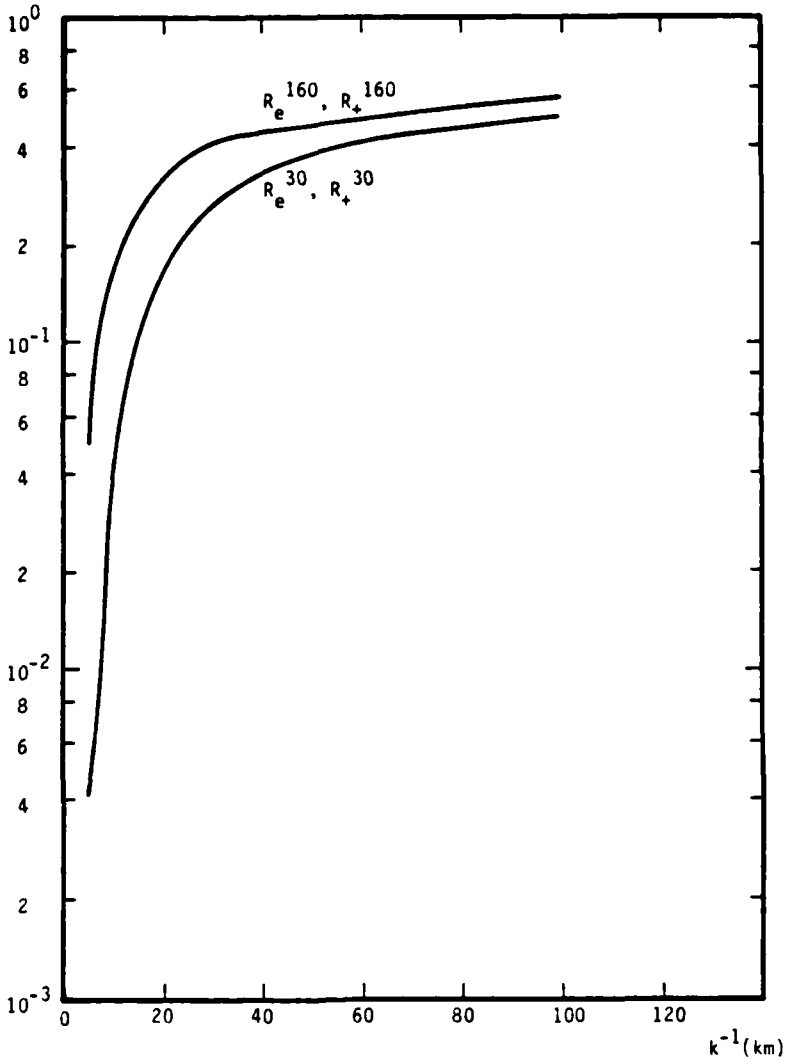

Figure 17. The rates of slow electron and ion production by 160 and 30 keV particles for magnetic field lines at an angle of 52.7° with the vertical relative to production rates for magnetic field lines at an angle of 0° with the vertical [i.e., $Re^{160} = ne^{160}(\theta = 52.7)/ne^{160}(\theta = 0)$, $Re^{30}_{+} = ne^{30}_{+}(\theta = 52.7)/ne^{30}_{+}(\theta = 0)$] are plotted versus inverse wavenumber at an altitude of 150 km. The initial ion and neutral densities at 400 km altitude are taken to be 1 and 0, respectively.

2.2 600 KM

In Figures 18-20 and Tables 3 and 4, the results of our calculations for fast particle structure degradation and slow particle production are graphed and tabulated for initial fast ion energies of 160 keV and 30 keV. The initial fast ion density at an altitude of 600 km at time equal to zero is normalized to be one for all wavenumbers while the initial fast neutral density is set equal to zero. The fast ion velocity makes an angle of 60^{o} with the magnetic field. As the fast ions move down the field line they are converted into fast neutrals by charge exchange. The neutrals subsequently either again revert to fast ion form due to impact ionization or are lost as a result of convection or diffusion.

The following figures and tables specifically address the 600 km VER248 MRC simulation.[5] Based on the simulation, the magnetic field is assumed to be vertical, aligned with the gravity vector, while the cold neutral background is assumed to be undisturbed by the nuclear burst to lowest order. These variables are shown in more detail in Figures 3 and 4. In Figures 18 and 19 normalized $n_i(k,t)$ and $n_n(k,t)$ are plotted versus altitude and time for 160 keV particles. The curves demonstrate that the fast ion contribution to structure decays most strongly for short wavelengths. The neutral density starts off at an initial value of zero and reaches a maximum for short wavelengths and then decays. For longer wavelengths the neutral density does not reach a maximum but continually increases for the times and altitudes of interest. Figures 20 and 22 are comparable to Figures 18 and 19 except that the particle energy is 30 keV. The general qualitative features ascribed to the earlier figures also apply to Figures 20 to 22. In Figures 23 and 24 the total fast ion and neutral density are plotted, at 310 km and 120 km, respectively. It is evident that a greater number of fast ion and neutral particles are lost from the short wavelength as compared to the long wave contribution to structure. This result is implied by the neutral diffusion and convection models which are most effective for short wavelengths. It is also noteworthy that for long wavelengths when the convective and diffusive losses are weakest the density profiles evolve in a quasi-steady state manner with

$$\nu_1 n_1(k,t) = \nu_2 n_2(k,t) \quad . \tag{8}$$

Table 3. The slow electron density production by 160 keV particles, $n_e^{160}(k_o)$, the slow ion density production by 160 keV particles, $n_+^{160}(k_o)$, the slow electron production by 30 keV particles, $n_e^{30}(k_o)$, and the slow ion production by 30 keV particles, $n_+^{30}(k_o)$, are tabulated as a function of altitude. k_o = 1/500 km. Quantities are in units of particles produced/cm per single particle at 600 km altitude.

H(km)	$n_e^{160}(k_o) \times 10^6$	$n_+^{160}(k_o) \times 10^6$	$n_e^{30}(k_o) \times 10^6$	$n_+^{30}(k_o) \times 10^6$
600-590	1.5×10^{-2}	7.1×10^{-2}	6.2×10^{-3}	1.4×10^{-2}
590-580	2.1×10^{-2}	7.4×10^{-2}	9.2×10^{-3}	1.5×10^{-2}
580-570	2.7×10^{-2}	7.6×10^{-2}	1.2×10^{-2}	1.5×10^{-2}
570-560	3.4×10^{-2}	8.0×10^{-2}	1.5×10^{-2}	1.5×10^{-2}
560-550	4.2×10^{-2}	8.2×10^{-2}	1.8×10^{-2}	1.5×10^{-2}
550-540	5.1×10^{-2}	8.7×10^{-2}	2.2×10^{-2}	1.6×10^{-2}
540-530	6.0×10^{-2}	9.1×10^{-2}	2.6×10^{-2}	1.6×10^{-2}
530-520	7.1×10^{-2}	9.6×10^{-2}	3.0×10^{-2}	1.6×10^{-2}
520-510	8.3×10^{-2}	1.0×10^{-1}	3.5×10^{-2}	1.6×10^{-2}
510-500	9.6×10^{-2}	1.1×10^{-1}	4.0×10^{-2}	1.7×10^{-2}
500-490	1.1×10^{-1}	1.2×10^{-1}	4.5×10^{-2}	1.7×10^{-2}
490-480	1.3×10^{-1}	1.3×10^{-1}	5.1×10^{-2}	1.8×10^{-2}
480-470	1.4×10^{-1}	1.4×10^{-1}	5.6×10^{-2}	1.9×10^{-2}
470-460	1.6×10^{-1}	1.6×10^{-1}	6.4×10^{-2}	2.2×10^{-2}
460-450	1.8×10^{-1}	1.8×10^{-1}	7.0×10^{-2}	2.4×10^{-2}
450-440	2.1×10^{-1}	2.0×10^{-1}	7.9×10^{-2}	2.7×10^{-2}
440-430	2.4×10^{-1}	2.2×10^{-1}	8.8×10^{-2}	3.1×10^{-2}
430-420	2.7×10^{-1}	2.5×10^{-1}	9.9×10^{-2}	3.7×10^{-2}
420-410	3.0×10^{-1}	2.8×10^{-1}	1.1×10^{-1}	4.2×10^{-2}
410-400	3.5×10^{-1}	3.2×10^{-1}	1.2×10^{-1}	5.0×10^{-2}
400-390	4.0×10^{-1}	3.7×10^{-1}	1.4×10^{-1}	5.8×10^{-2}
390-380	4.6×10^{-1}	4.2×10^{-1}	1.6×10^{-1}	7.0×10^{-2}
380-370	5.3×10^{-1}	4.8×10^{-1}	1.7×10^{-1}	8.1×10^{-2}
370-360	6.1×10^{-1}	5.5×10^{-1}	2.0×10^{-1}	9.7×10^{-2}
360-350	7.0×10^{-1}	6.3×10^{-1}	2.2×10^{-1}	1.1×10^{-1}

Table 3 (Continued)

H(km)	$n_e^{160}(k_o) \times 10^6$	$n_+^{160}(k_o) \times 10^6$	$n_e^{30}(k_o) \times 10^6$	$n_+^{30}(k_o) \times 10^6$
350-340	8.2×10^{-1}	7.3×10^{-1}	2.5×10^{-1}	1.4×10^{-1}
340-330	9.4×10^{-1}	8.4×10^{-1}	2.9×10^{-1}	1.6×10^{-1}
330-320	1.1×10^{0}	9.9×10^{-1}	3.3×10^{-1}	1.9×10^{-1}
320-310	1.3×10^{0}	1.1×10^{0}	3.7×10^{-1}	2.3×10^{-1}
310-300	1.8×10^{0}	1.6×10^{0}	4.9×10^{-1}	3.2×10^{-1}
300-290	2.1×10^{0}	1.8×10^{0}	5.7×10^{-1}	3.9×10^{-1}
290-280	2.5×10^{0}	2.2×10^{0}	6.6×10^{-1}	4.7×10^{-1}
280-270	3.0×10^{0}	2.6×10^{0}	7.8×10^{-1}	5.7×10^{-1}
270-260	3.6×10^{0}	3.1×10^{0}	9.2×10^{-1}	7.0×10^{-1}
260-250	4.3×10^{0}	3.8×10^{0}	1.1×10^{0}	8.6×10^{-1}
250-240	5.3×10^{0}	4.6×10^{0}	1.3×10^{0}	1.1×10^{0}
240-230	6.5×10^{0}	5.7×10^{0}	1.6×10^{0}	1.3×10^{0}
230-220	8.2×10^{0}	7.1×10^{0}	1.9×10^{0}	1.7×10^{0}
220-210	1.0×10^{1}	9.0×10^{0}	2.4×10^{0}	2.2×10^{0}
210-200	1.4×10^{1}	1.2×10^{1}	3.1×10^{0}	2.9×10^{0}
200-190	1.8×10^{1}	1.6×10^{1}	4.0×10^{0}	3.9×10^{0}
190-180	2.5×10^{1}	2.1×10^{1}	5.4×10^{0}	5.4×10^{0}
180-170	3.5×10^{1}	3.0×10^{1}	7.6×10^{0}	7.7×10^{0}
170-160	5.3×10^{1}	4.5×10^{1}	1.1×10^{1}	1.2×10^{1}
160-150	8.6×10^{1}	7.3×10^{1}	1.8×10^{1}	1.9×10^{1}
150-140	1.5×10^{2}	1.3×10^{2}	3.1×10^{1}	3.4×10^{1}
140-130	3.2×10^{2}	2.7×10^{2}	6.4×10^{1}	7.3×10^{1}
130-120	1.0×10^{3}	8.4×10^{2}	1.9×10^{2}	2.3×10^{2}

Table 4. The total production of slow electrons and ions between 600 and 120 km per single fast ion at 600 km altitude is tabulated as a function of inverse wavenumber.

k^{-1}(km)	$n_{eT}^{160}(k)$	$n_{+T}^{160}(k)$	$n_{eT}^{30}(k)$	$n_{+T}^{30}(k)$
5	3.4	2.5	1.5×10^{-1}	2.1×10^{-1}
20	4.0×10^{2}	3.5×10^{2}	1.7×10^{1}	1.9×10^{1}
100	1.5×10^{-3}	1.3×10^{3}	2.2×10^{2}	2.6×10^{2}
500	1.8×10^{3}	1.5×10^{3}	3.4×10^{2}	3.9×10^{2}

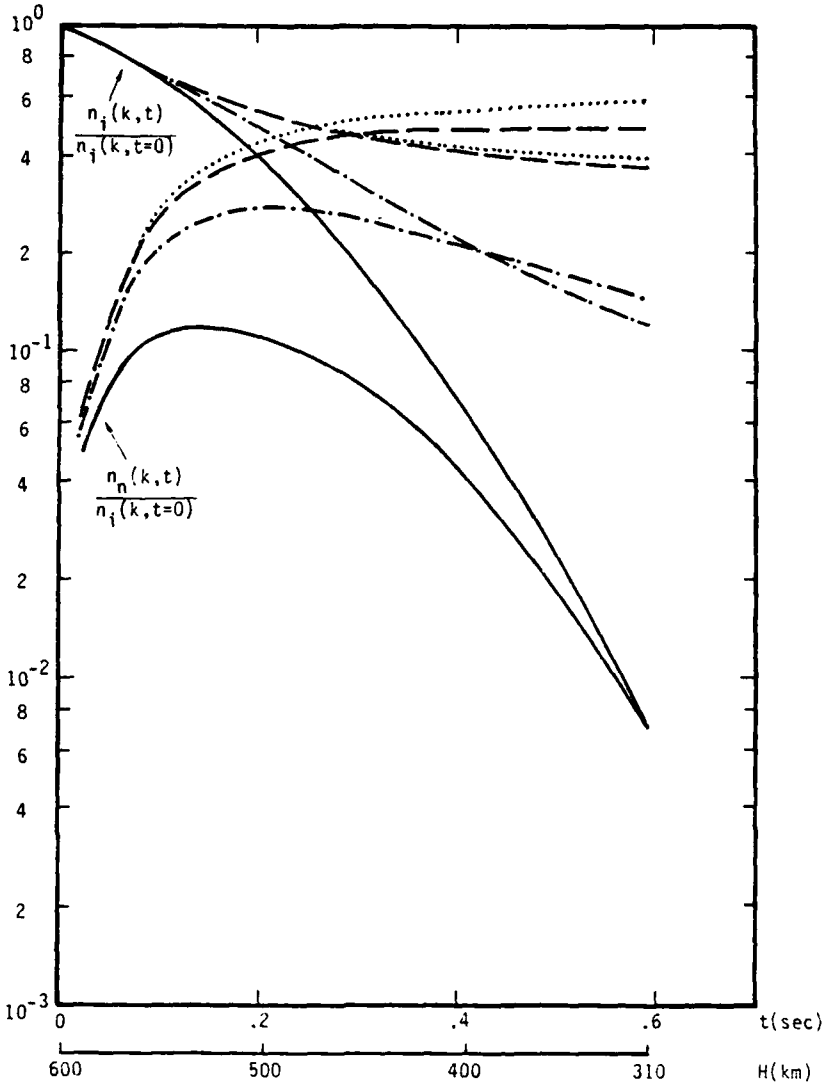

Figure 18. For 160 keV particles, the fast ion density, as a function of wavenumber and time, $n_i(k,t)$, and the fast neutral density as a function of wavenumber and time, $n_n(k,t)$, are normalized to the initial fast ion density at time, t = 0 sec, and altitude, 600 km, and plotted versus time, t(sec), and altitude, H(km). The initial neutral density is zero. The different types of lines used in the figure represent different wavelengths: k^{-1} = 5 km ———, = 20 km - - -, = 100 km — • —, and = 500 km •••••

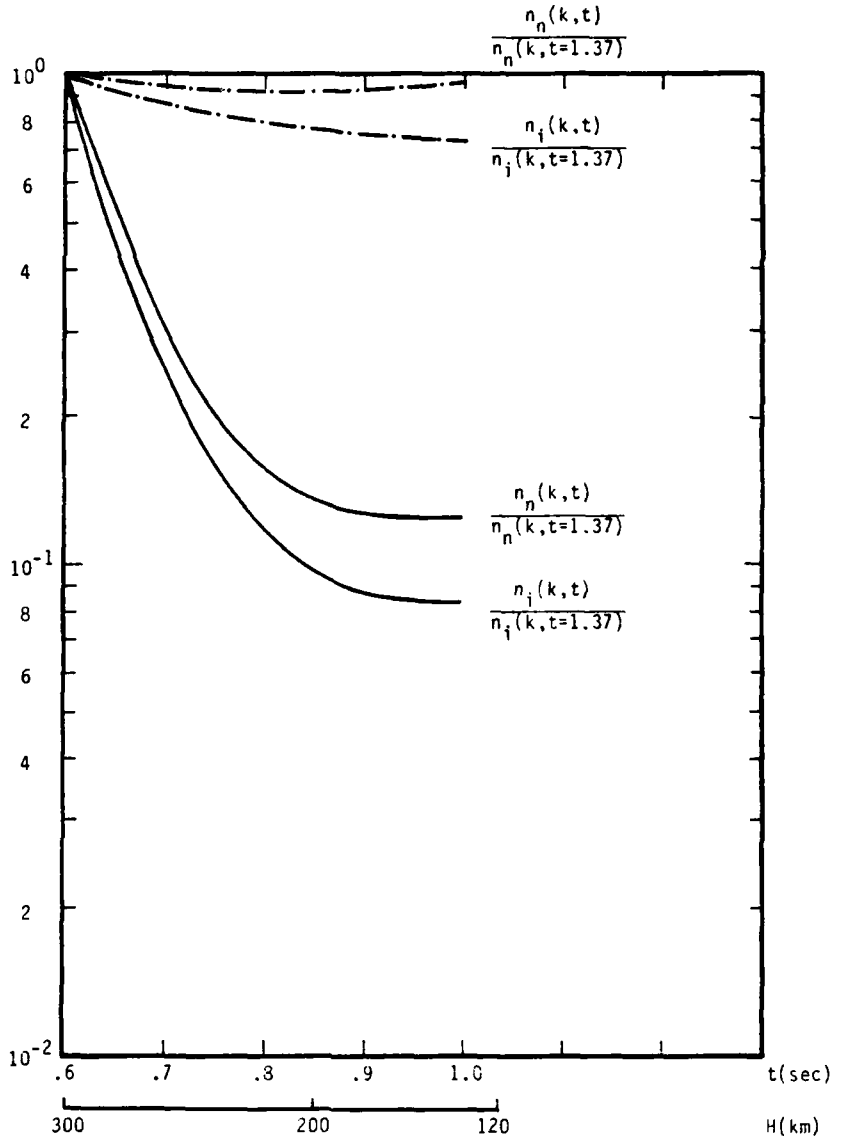

Figure 19. For 160 keV particles, the fast ion density, as a function of wavenumber and time, $n_i(k,t)$, and the fast neutral density as a function of wavenumber and time, $n_n(k,t)$, are normalized to the initial fast ion density at time, t = 1.368 sec, and altitude, 310 km, and plotted versus time, t(sec), and altitude, H(km). The initial neutral density is zero. The different types of lines used in the figure represent different wavelengths: k^{-1} = 5 km ——— , = 20 km - - - , = 100 km — · — ·, and = 500 km ·····

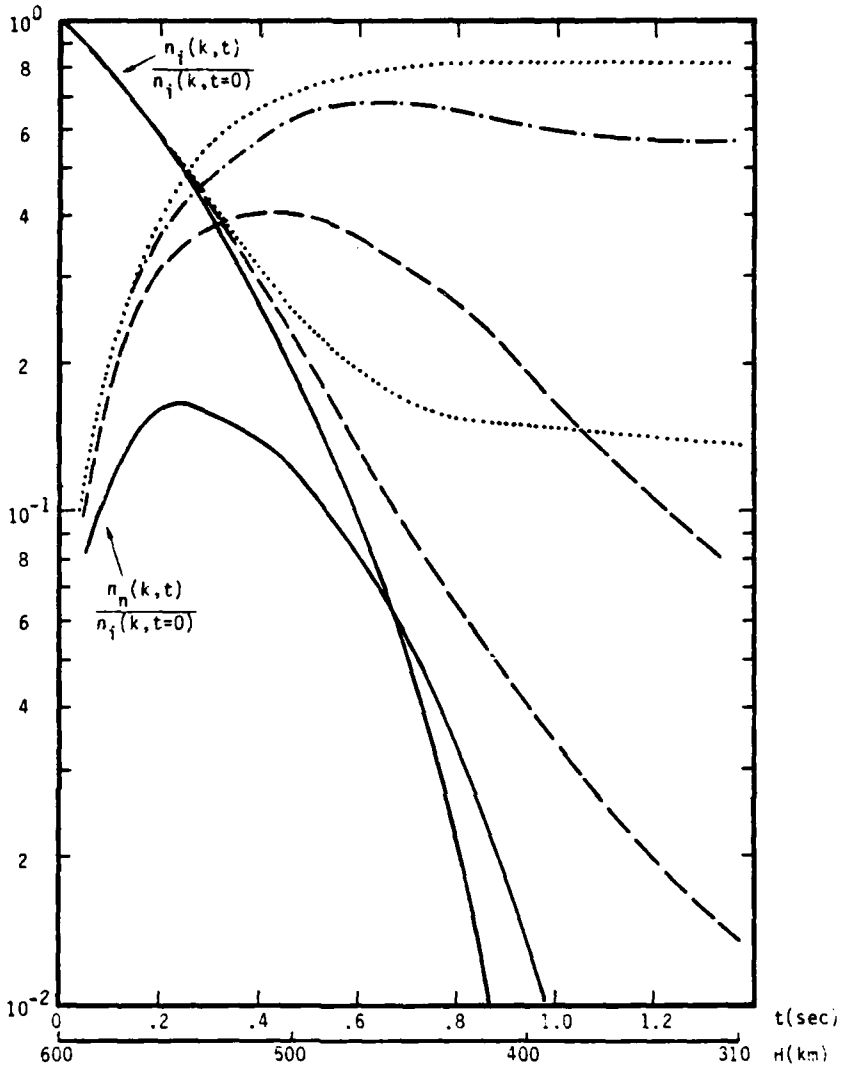

Figure 20. For 30 keV particles, the fast ion density, as a function of wavenumber and time, $n_f(k,t)$, and the fast neutral density as a function of wavenumber and time, $n_n(k,t)$, are normalized to the initial fast ion density at time, t = 0 sec, and altitude, 600 km, and plotted versus time, t(sec), and altitude, H(km). The initial neutral density is zero. The different types of lines used in the figure represent different wavelengths: k^{-1} = 5 km ——— , = 20 km - - -, = 100 km — · —·, and = 500 km ·····

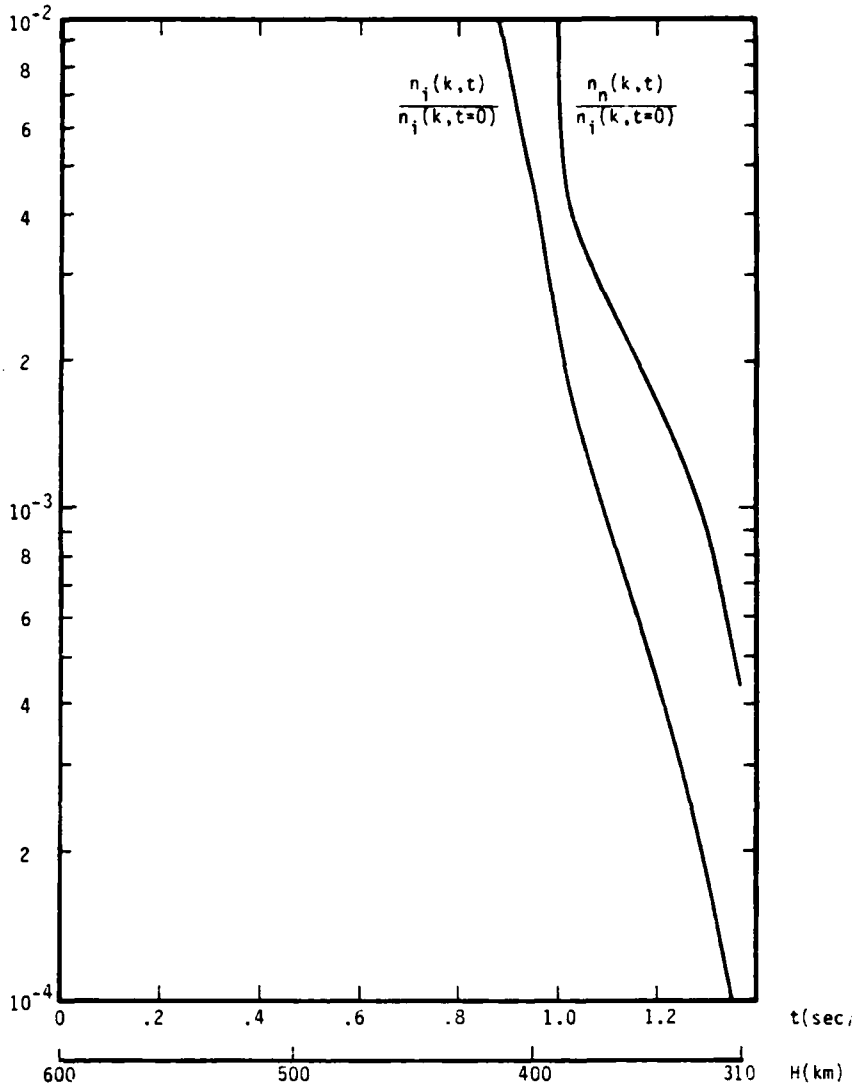

Figure 21. For 30 keV particles, the fast ion density, as a function of wavenumber and time, $n_i(k,t)$, and the fast neutral density as a function of wavenumber and time, $n_n(k,t)$, are normalized to the initial fast ion density at time, t = 0 sec, and altitude, 600 km, and plotted versus time, t(sec), and altitude, H(km). The initial neutral density is zero. The different types of lines used in the figure represent different wavelengths: k^{-1} = 5 km ———, = 20 km - - -, = 100 km — · — ·, and = 500 km ·····

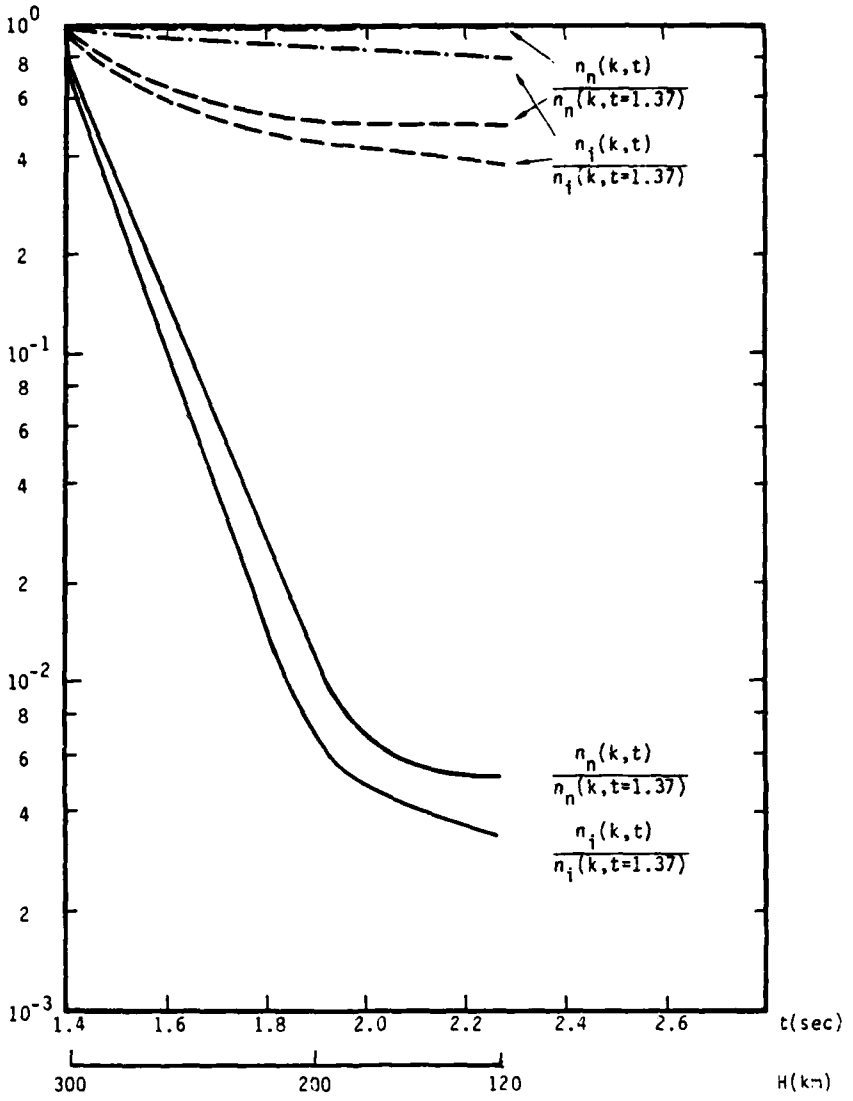

Figure 22. For 30 keV particles, the fast ion density, as a function of wavenumber and time, $n_i(k,t)$, and the fast neutral density as a function of wavenumber and time, $n_n(k,t)$, are normalized to the initial fast ion density at time, t = 1.368 sec, and altitude, 310 km, and plotted versus time, t(sec), and altitude, H(km). The initial neutral density is zero. The different types of lines used in the figure represent different wavelengths: k^{-1} = 5 km ———, = 20 km - - -, = 100 km — · — ·, and = 500 km ·····

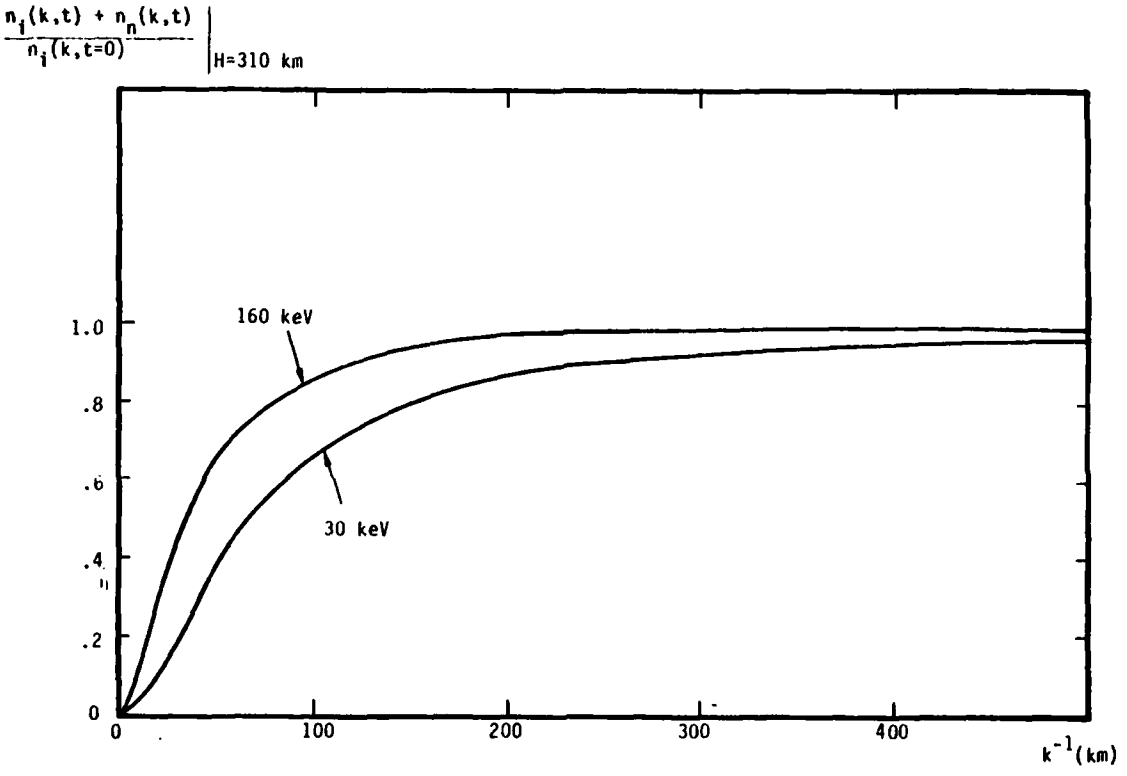

Figure 23. The total fast ion and fast neutral density at H = 310 km normalized to the initial fast ion density versus inverse wavenumber in kilometers.

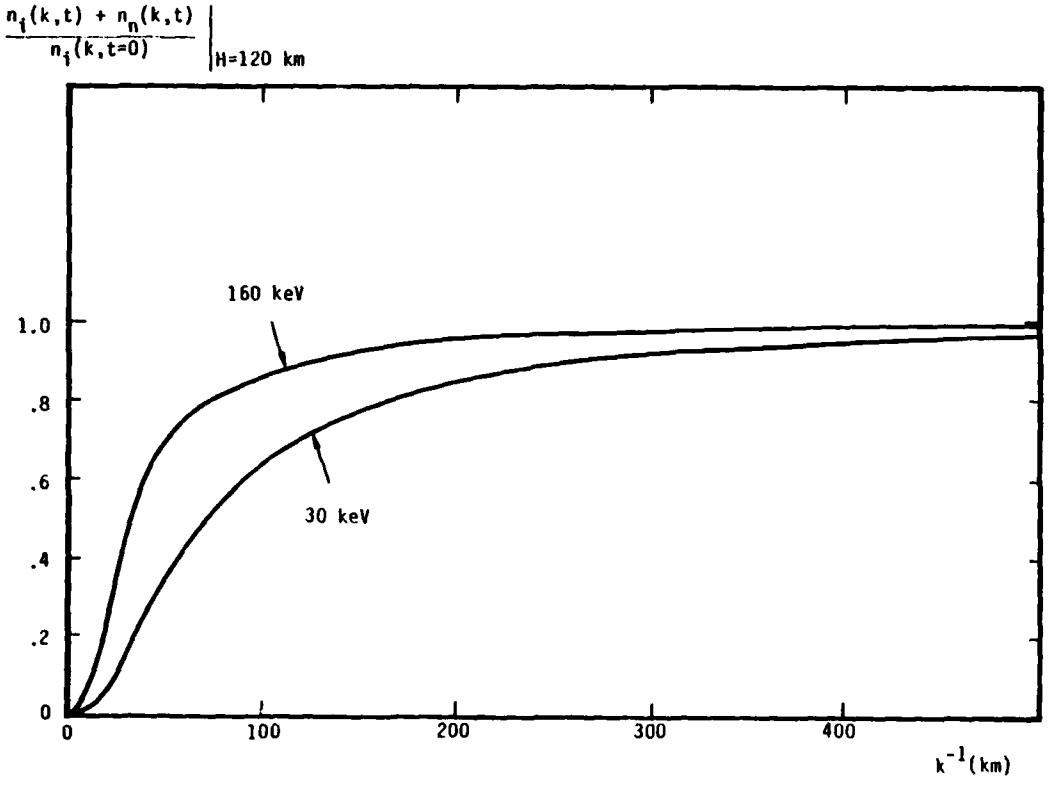

Figure 24. The total fast ion and fast neutral density at H = 110 km normalized to the initial fast ion density versus inverse wavenumber in kilometers.

The slow electron and ion production due to ionization by 160 keV and 30 keV ions and neutral particles is tabulated in Table 3 for the 500 km wavelength and plotted in Figures 25 - 28 for shorter wavelengths. In the figures the slow electron and ion densities are normalized to the corresponding 500 km wavelength values found in Table 3. Because the calculations are based on the CIRA tables which are tabulated for 10 km distance intervals, the numbers in Table 3 are actually the number of particles which would be generated for a time interval corresponding to the traversal of 160 or 30 keV particles across ten kilometers of altitude. To determine an average value for slow electron and ion density per cubic centimeter over a ten kilometer distance, the numbers in the table are divided by 10^6. There are four significant qualitative features in Table 3 and Figures 25 - 28. First, the number of slow particles produced increases at lower altitudes for the 500 km wavelength calculation primarily because the neutral convection or diffusion losses are relatively weak compared to shorter wavelengths and because the cold neutral background is greater at lower rather than at higher altitudes. Second, relative to the 500 kilometer slow electron and ion generation, the generation at shorter wavelengths becomes increasingly weaker especially at lower altitudes. The reason for this effect is the loss of fast ions and neutrals due to the convective and diffusive neutral loss processes at short wavelengths. Third, the total density of slow electrons and ions which would be contained within one cubic centimeter if the slow particle generation had taken place within one cubic centimeter can be calculated by adding up the contributions in each column of Table 3. It is clear that carrying out the calculation down to an altitude of 310 km still permits the creation of a larger number of electrons and ions than were in the original 500 km structure at an altitude of 600 km (see Table 4). However, for shorter wavelengths the number of slow electrons and ions is smaller than for k^{-1} = 500 km. This effect is again due to the loss mechanism which especially affects short wavelength structure. Fourth, the 160 keV particles generate a greater number of slow electrons and ions than do the 30 keV particles.

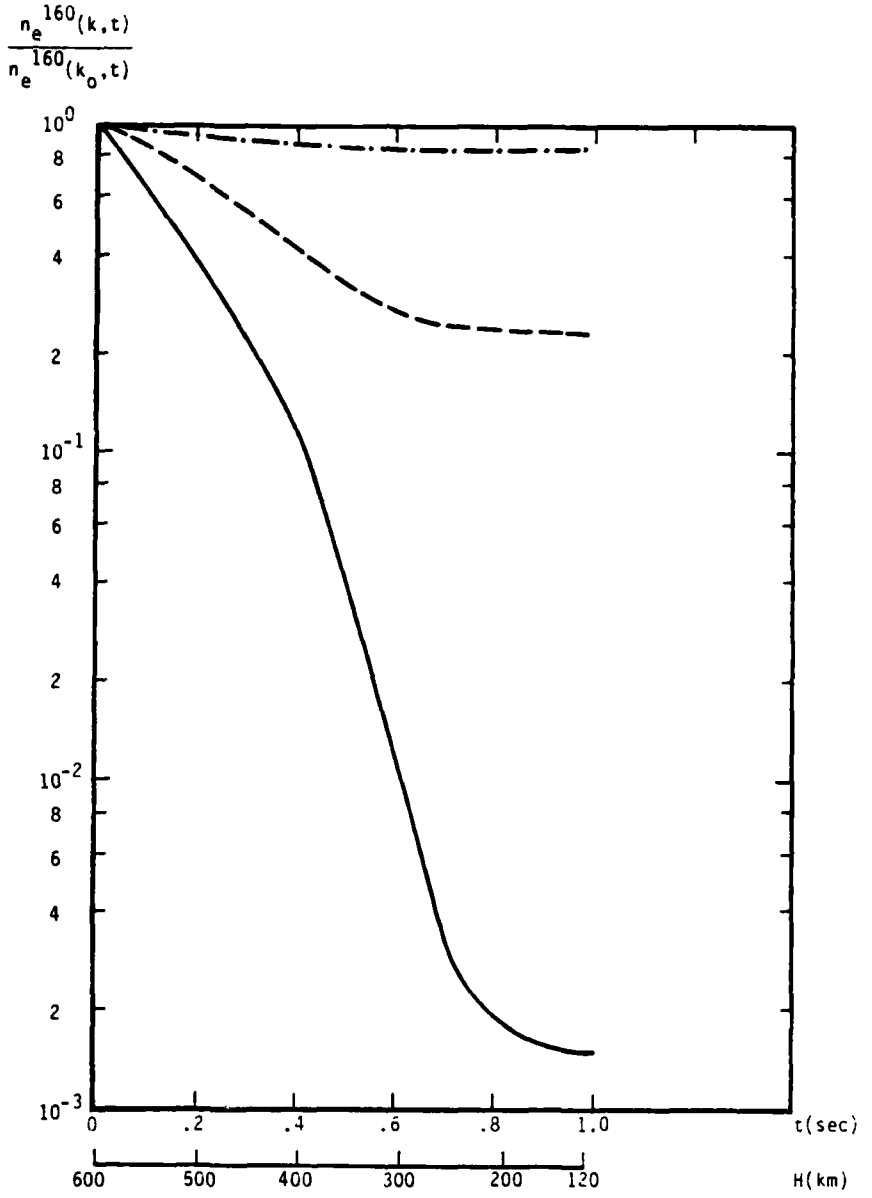

Figure 25. For 160 keV particles, the slow electron production as a function of wavenumber and time is normalized to the corresponding quantity in Table 3 (k_o^{-1} = 500 km) and plotted versus altitude, H(km), and time, t(sec). The different types of lines in the figure represent different wavenumbers: k^{-1} = 5 km ———, = 20 km - - -, = 100 km —·—·

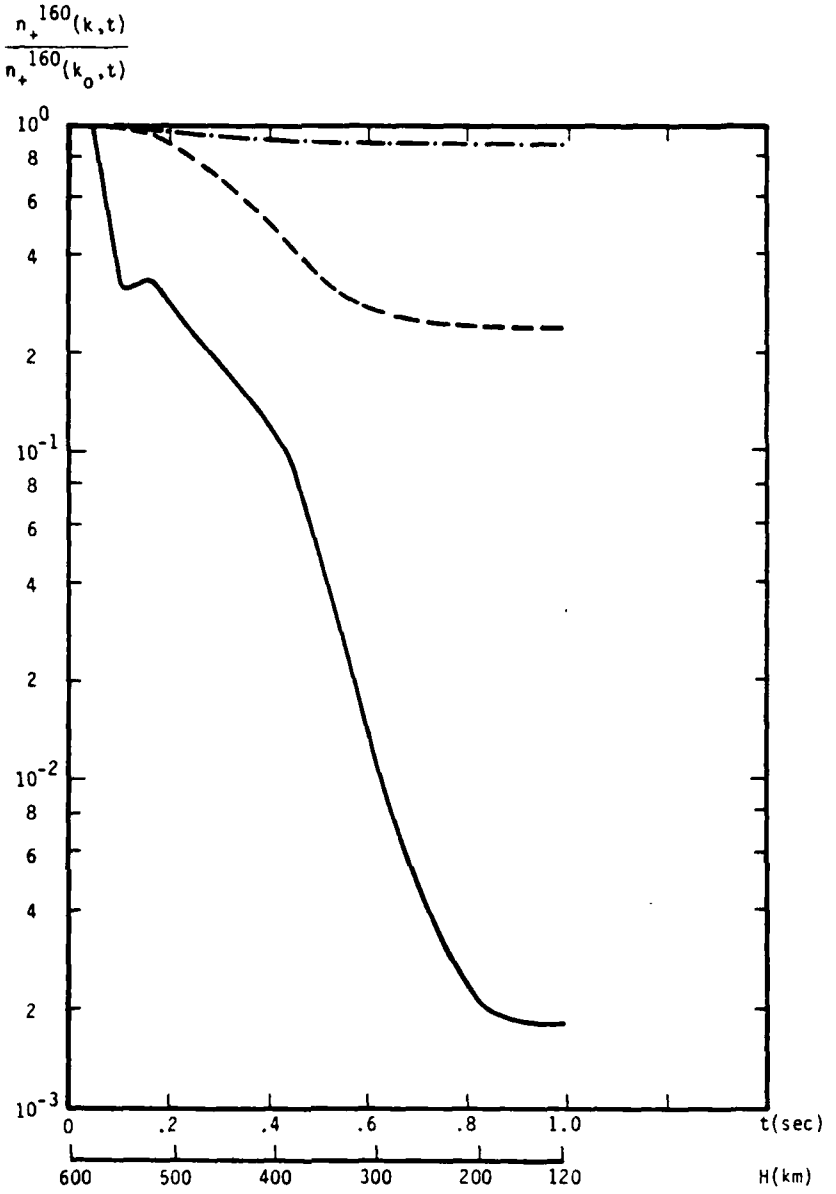

Figure 26. For 160 keV particles, the slow positive ion production as a function of wavenumber and time is normalized to the corresponding quantity in Table 3 (k_o^{-1} = 500 km) and plotted versus altitude, H(km), and time, t(sec). The different types of lines in the figure represent different wavenumbers: k^{-1} = 5 km ———, = 20 km - - -, = 100 km — · —.

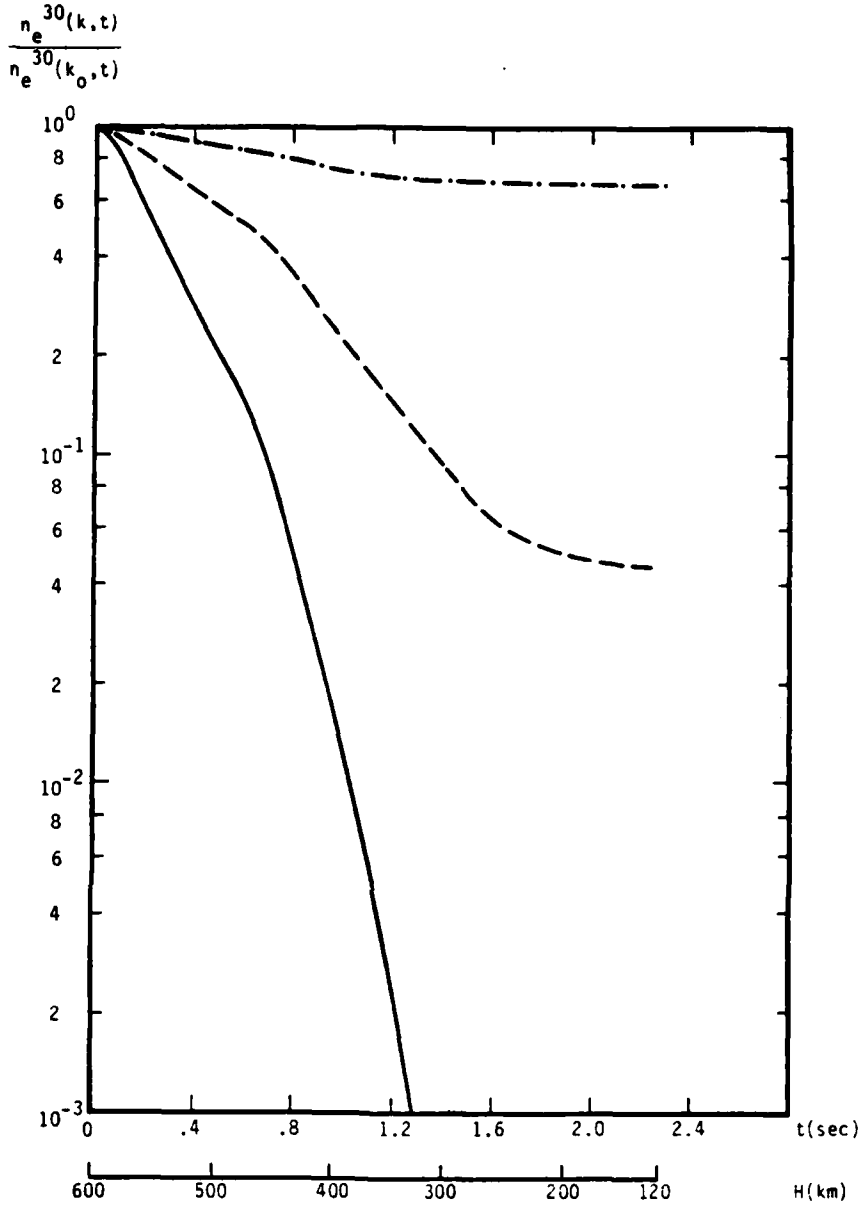

Figure 27. For 30 keV particles, the fast electron production as a function of wavenumber and time is normalized to the corresponding quantity in Table 3 (k_o^{-1} = 500 km) and plotted versus altitude, H(km), and time, t(sec). The different types of lines in the figure represent different wavenumbers: k^{-1} = 5 km ———, = 20 km - - -, = 100 km —·—·

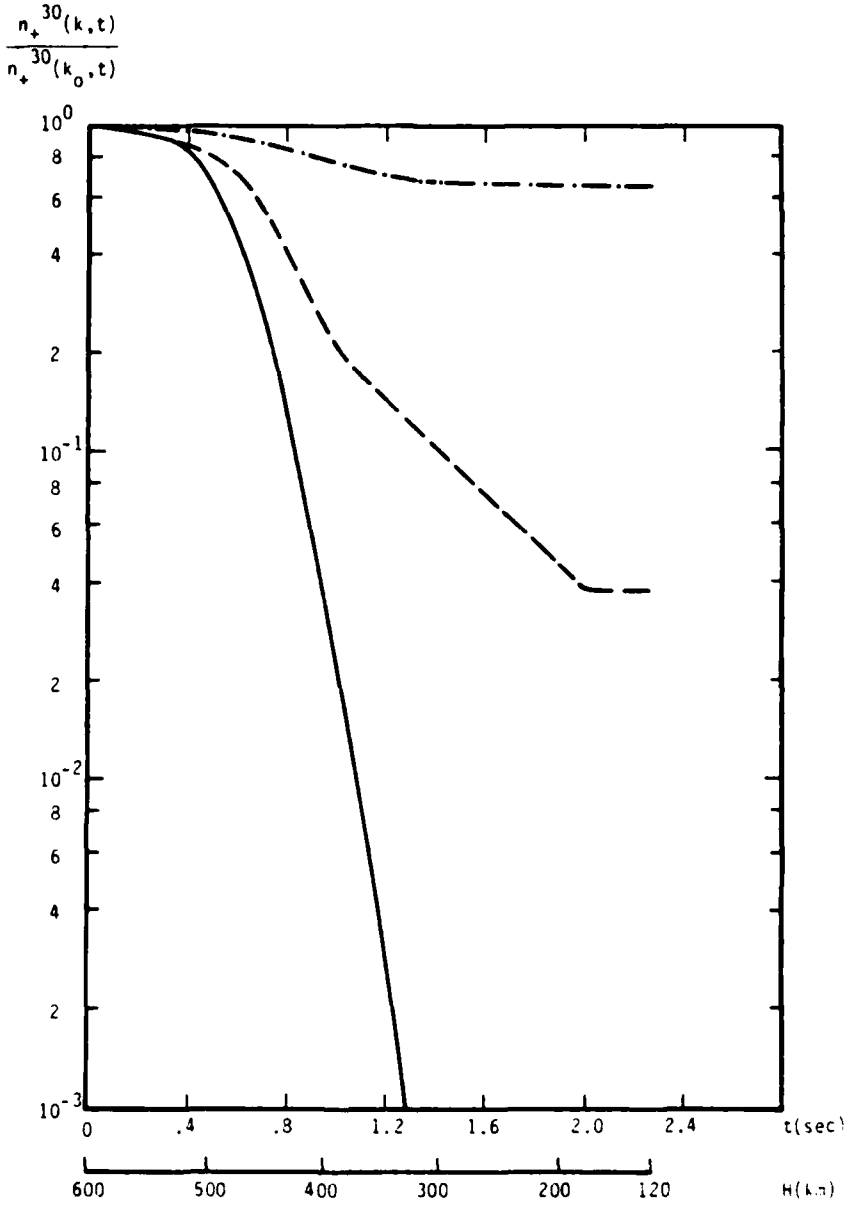

Figure 28. For 30 keV particles, the fast positive ion production as a function of wavenumber and time is normalized to the corresponding quantity in Table 3 (k_o^{-1} = 500 km) and plotted versus altitude, H(km), and time, t(sec). The different types of lines in the figure represent different wavenumbers: k^{-1} = 5 km ——, = 20 km - - -, = 100 km — · — ·

2.3 200 KM

Calculations to determine the decay of fast ionized structure down field lines as a result of charge exchange and impact ionization have been carried out for a burst altitude of 200 km with the ambient atmosphere chosen from Reference 6, consistent with MRC simulations.[5] Also, based upon the MRC simulations, LOW BEAR 200 and LITTLE ONE 200, the magnetic field lines in the vicinity of the burst are taken to be at 45 degrees with the vertical and the cold neutral density along the magnetic field lines is assumed to be a constant and appropriate to the bubble surface (i.e., 3×10^{-15} grams/cm^3). Results are summarized in Table 5 and Figures 29 to 35. The geometry for this case is shown in Figures 5 and 6. Because contours of constant density are roughly parallel to the magnetic field and the cold neutral density variation across the magnetic field was not taken into account in the calculations, the results presented here actually represent an underestimate of the actual impact of charge exchange and impact ionization on the decay of the initial fast ion structure.

Neutral effects appear singularly weak in this case (compared to those previous) because the high degree of ionization associated with a fireball has eroded the cold neutral density appropriate to the ambient undisturbed ionosphere. In reality, far from the burst point the cold neutral density approaches ambient and slow electron and ion production becomes much larger than the initial fast ion density, and is comparable to the lower altitude production for the 600 km and 400 km bursts presented above. This is not determined quantitatively from the microfiche data of Reference 5.

Table 5. The total number of slow electrons and ions between 200 and 200 km produced per single fast ion at 200 km is tabulated as a function of inverse wavenumber.

k^{-1}(km)	$n_{eT}^{160}(k)$	$n_{+T}^{160}(k)$	$n_{eT}^{30}(k)$	$n_{+T}^{30}(k)$
5	1.1	1.6	.29	.82
20	1.5	1.8	.39	.88
100	1.7	1.9	.44	.91
500	1.8	1.9	.50	.94

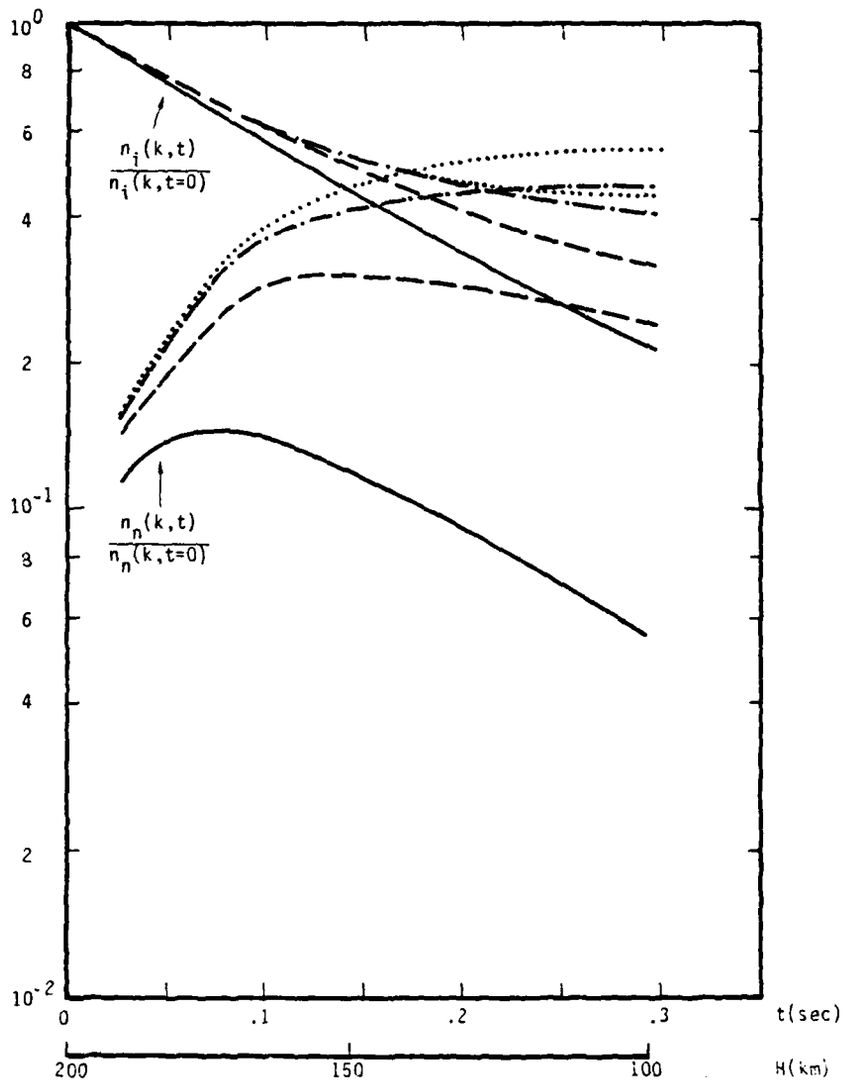

Figure 29. For 160 keV particles, the fast ion density as a function of wavenumber and time, $n_i(k,t)$, and the fast neutral density as a function of wavenumber and time, $n_n(k,t)$, are normalized to the initial fast ion density at time, t = 0 sec, and altitude, 200 km, and plotted versus time, t(sec), and altitude, H(km). The initial neutral density is zero. The different types of lines in the figure represent different wavelengths: k^{-1} = 5 km ——— , = 20 km - - - , = 100 km — · — · , and = 500 km ····· . The total cold neutral density is taken to be 3×10^{-15} g/cm^3.

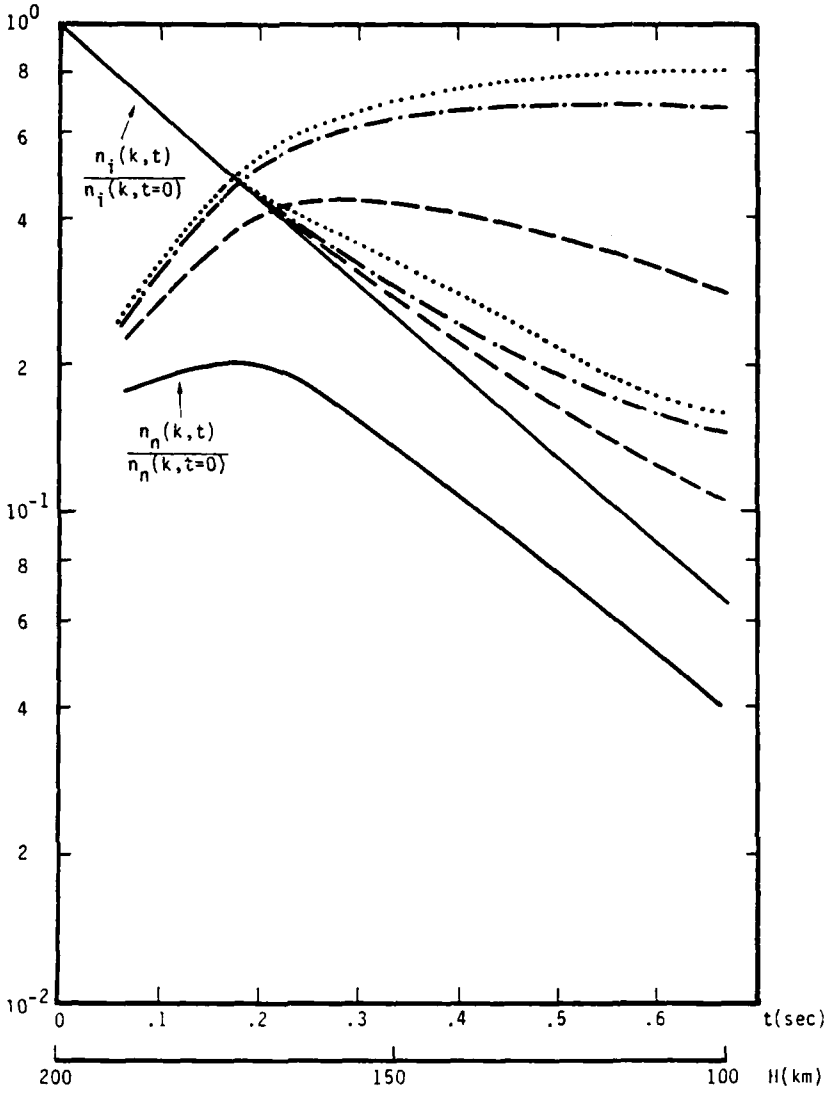

Figure 30. For 30 keV particles, the fast ion density as a function of wavenumber and time, $n_i(k,t)$, and the fast neutral density as a function of wavenumber and time, $n_n(k,t)$, are normalized to the initial fast ion density at time, t = 0 sec, and altitude, 200 km, and plotted versus time, t(sec), and altitude, H(km). The initial neutral density is zero. The different types of lines in the figure represent different wavelengths: k^{-1} = 5 km ——— , = 20 km - - - , = 100 km — · — ·, and = 500 km ····· . The total cold neutral density is taken to be 3×10^{-15} g/cm^3.

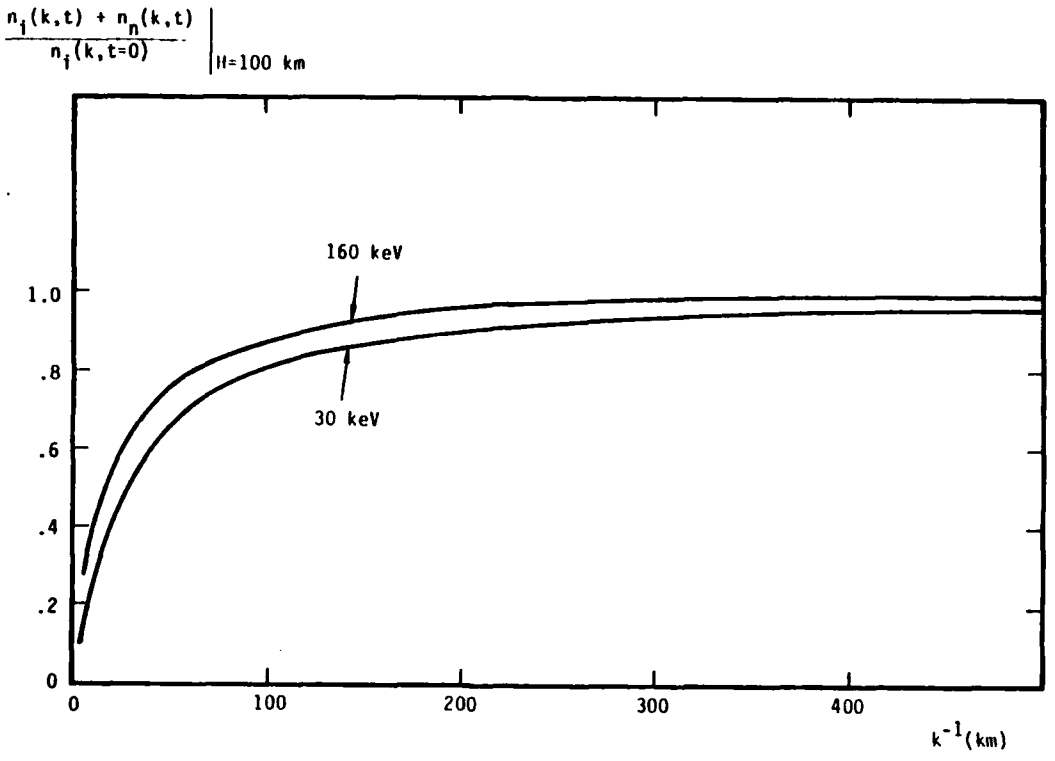

Figure 31. The total fast ion and fast neutral density at H = 100 km normalized to the initial fast ion density versus wavenumber in kilometers.

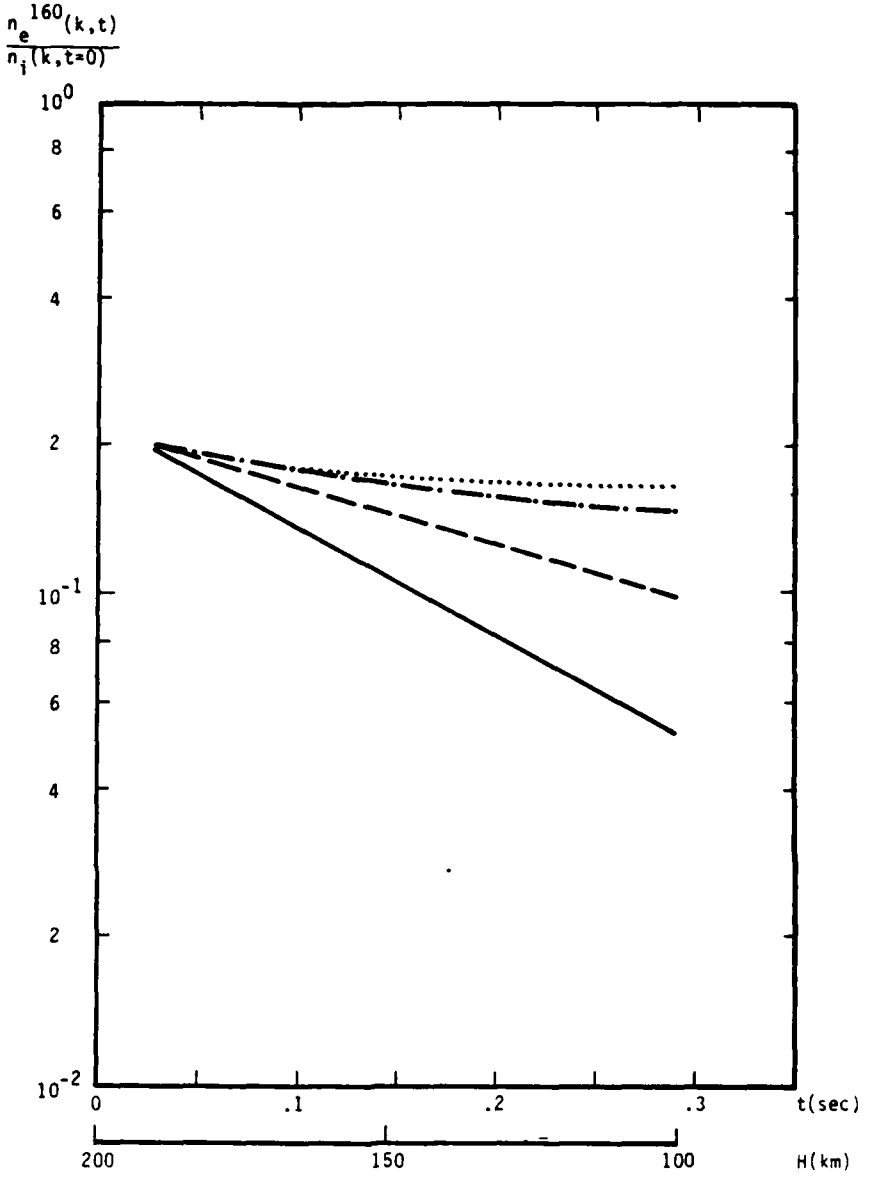

Figure 32. For 160 keV particles, the slow electron production as a function of wavenumber and time normalized to the initial fast ion density. The different types of lines represent different wavenumbers: k^{-1} = 5 km ——— , = 20 km - - - , = 100 km — · — ·, and = 500 km ····· .

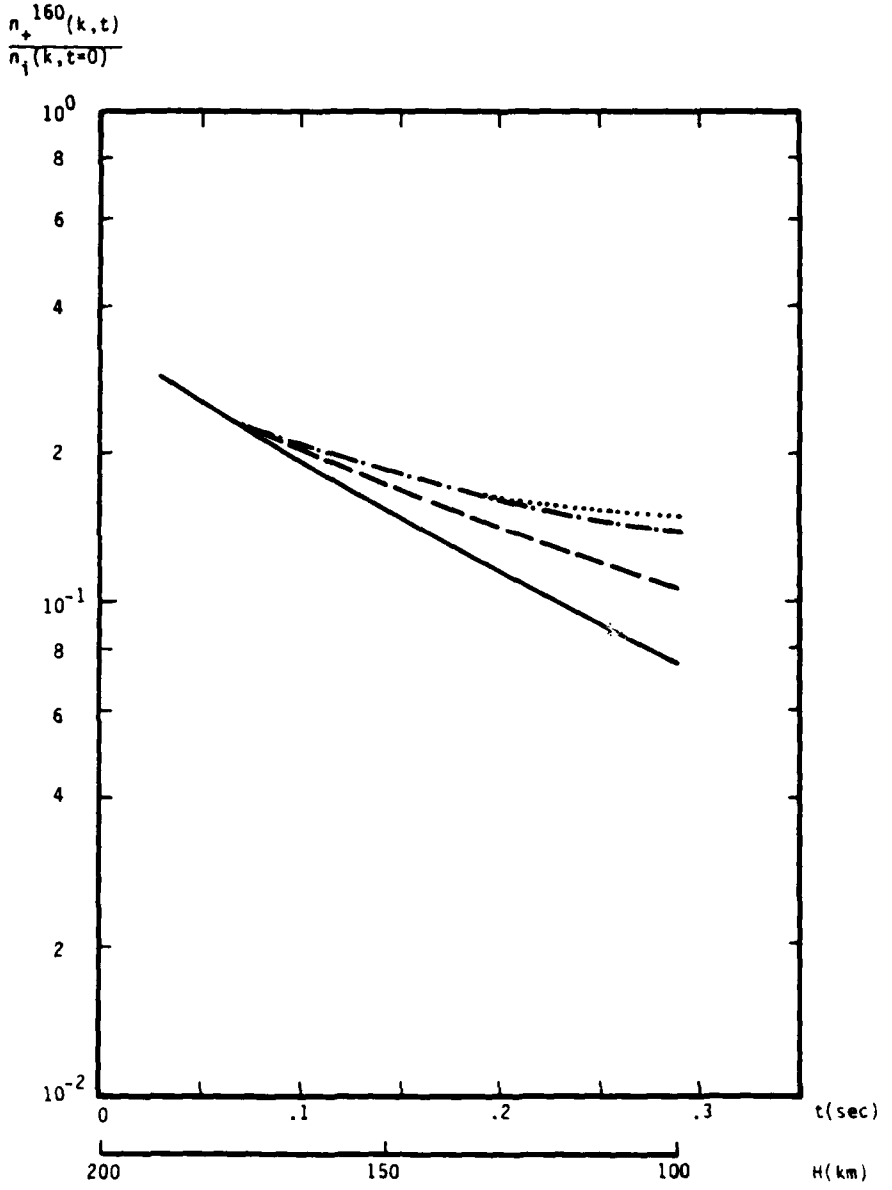

Figure 33. For 160 keV particles, the slow ion production as a function of wavenumber and time normalized to the initial fast ion density. The different types of lines represent different wavenumbers: k^{-1} = 5 km ——— , = 20 km - - - , = 100 km — · — ·, and = 500 km ····· .

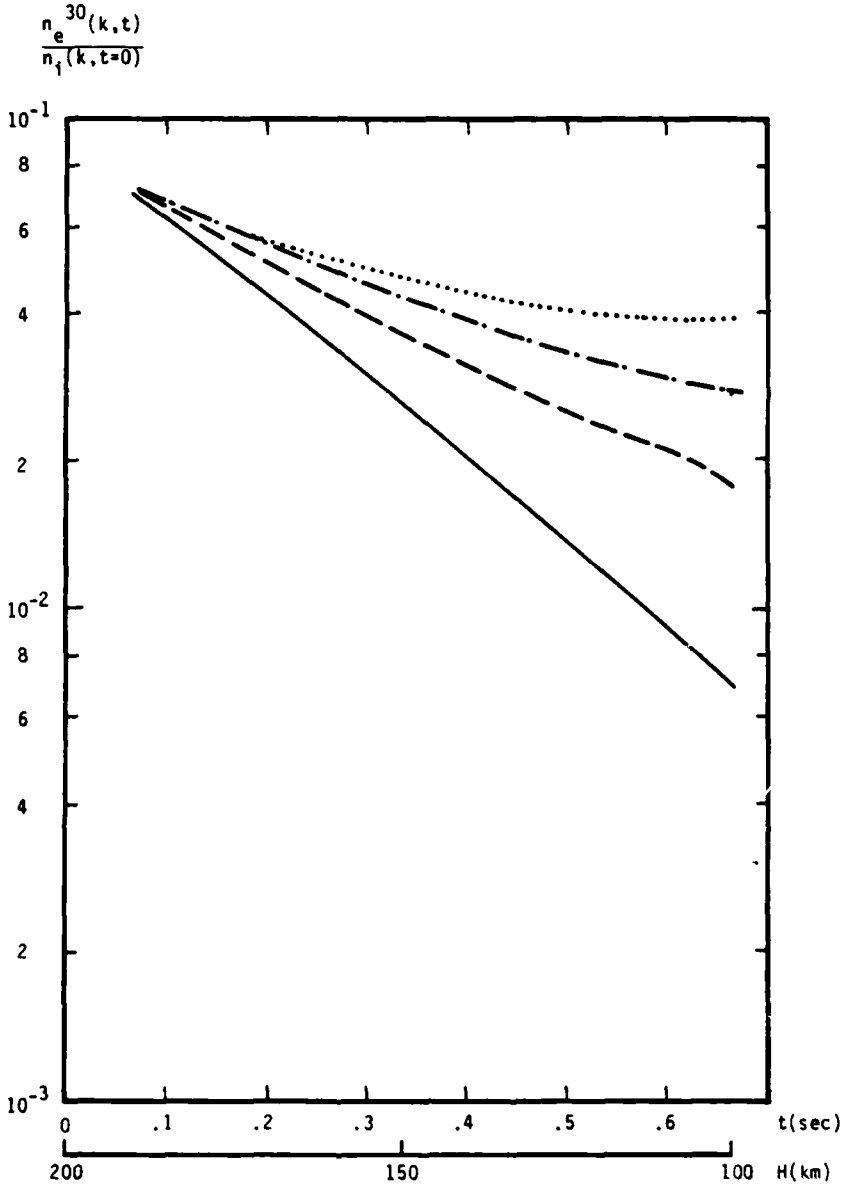

Figure 34. For 30 keV particles, the fast electron production as a function of wavenumber and time normalized to the initial fast ion density. The different types of lines represent different wavenumbers: k^{-1} = 5 km ——— , = 20 km - - - , = 100 km — · — ·, and = 500 km ····· .

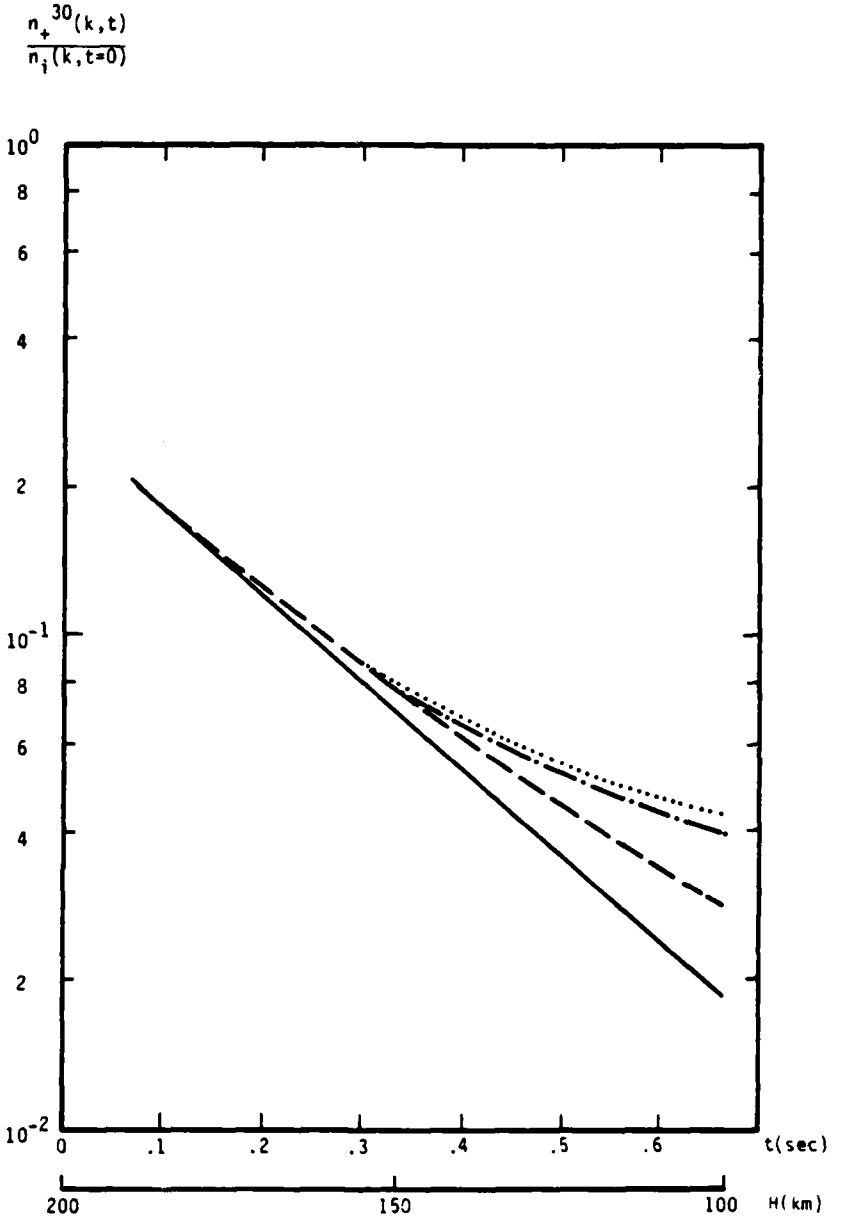

Figure 35. For 30 keV particles, the fast ion production as a function of wavenumber and time normalized to the initial fast ion density. The different types of lines represent different wavenumbers: k^{-1} = 5 km ——— , = 20 km - - - , = 100 km — · — ·, = 500 km ····· .

3. EFFECT OF DECAY BY RECOMBINATION ON THE PSD

All ionization decay appears to be nonlinear in the ionization density, since at some point in the recombination process (which can be succession of interactions) two charged particles produce a neutral. This can be seen in detail in References 7 and 8.

Ionization decay should obey an equation of the form

$$\frac{dn}{dt} = -\alpha n^2 \tag{9}$$

with

α = decay coefficient

n = electron density.

We will do specific calculations with α = constant, although generally $\frac{d\alpha}{dn} > 0$.[8] Usage of α = constant in place of $\frac{d\alpha}{dn} > 0$ would tend to present a lower bound on the smoothing effect of nonlinear decay, but further intricacy is possible.

Consider variation over a time interval with

$$0 < t < t \quad , \tag{10a}$$

$$n(t = 0) = n_0 \quad , \tag{10b}$$

$$n(t) = n \quad . \tag{10c}$$

Then integrating Eq. (9) results in

$$\frac{1}{n} - \frac{1}{n_0} = \alpha t \quad , \tag{11a}$$

or

$$n = \frac{n_0}{1 + \alpha t\, n_0} \quad . \tag{11b}$$

On Fourier transforming both sides over a periodicity length X:

$$n(\vec{k}) = \int_0^X e^{-ikX'} \quad \frac{n_0}{1 + \alpha t\, n_0} \; dX' \quad . \tag{12}$$

For $n_0\, \alpha t < 1$,

$$n(\vec{k}) = n_0(\vec{k}) \quad . \tag{13}$$

Clearly, nothing much happens chemically.

For

$$n_0\, \alpha t >> 1 \tag{14}$$

one has:

$$\frac{n_0}{1 + \alpha t\, n_0} = \frac{n_0}{n_0\, \alpha t\, (1 + \frac{1}{n_0 \alpha t})}$$

$$= \frac{1}{\alpha t} \left[1 - \frac{1}{n_0 \alpha t} + \frac{1}{(n_0 \alpha t)^2} + \ldots\right] \quad . \tag{15}$$

Then:

$$n(\vec{k} = 0) = \frac{X}{\alpha t} \quad , \tag{16a}$$

but:

$$n(\vec{k} \neq 0) = \frac{-1}{(\alpha t)^2} \int_0^X \frac{1}{n_0} \; e^{-ikX'} \; dX' \quad . \tag{16b}$$

Combination of Eqs. (16a) and (16b) results in the interesting conclusion that the ratio $n(\vec{k} \neq 0)/n(\vec{k} = 0)$ decreases with increasing time. To see this, consider the case ($k_1 \neq 0$):

$$n_0 = n_0(\vec{k} = 0) + 2n_0(\vec{k}_1)\cos(k_1 X) \quad , \quad k_1 \neq 0$$

$$2n_0(\vec{k}_1) \ll n_0(\vec{k} = 0) \quad . \tag{17}$$

Then:

$$\frac{1}{n_0} = \frac{1}{n_0(\vec{k} = 0)} - \frac{2n_0(\vec{k}_1)}{n_0^2(\vec{k} = 0)}\cos(k_1 X) \tag{18}$$

and, using (16b):

$$n(k_1) = -\frac{1}{(\alpha t)^2}\int_0^X (-)\frac{2n_0(k_1)}{n_0^2(k = 0)} e^{ik_1 X'} \cos k_1 X' \, dX'$$

$$= \frac{X}{(\alpha t)^2}\frac{n_0(k_1)}{n_0^2(k = 0)} \quad . \tag{19}$$

Next using Eqs. (16a) and (11b):

$$\frac{n(k_1)}{n(k = 0)} = \frac{1}{\alpha t}\frac{n_0(k_1)}{n_0^2(k = 0)} \simeq \frac{n_0(k_1)}{n_0(k = 0)}\frac{n_0}{n_0(k = 0)} \quad . \tag{20}$$

Associating $n_0(k = 0)$ with n_0 results in

$$\frac{n(k_1)}{n(k = 0)} \simeq \frac{n}{n_0}\frac{n_0(k_1)}{n_0(k = 0)} \ll \frac{n_0(k_1)}{n_0(k = 0)} \quad . \tag{21}$$

Alternatively, again associating $n_0(k = 0)$ with n_0; $n(k = 0)$ with n:

$$n(k_1) \simeq \frac{n^2}{n_0}\frac{n_0(k_1)}{n_0} \quad . \tag{22}$$

Combination of Eqs. (11b), (22), and (13) leads to Figure 36. It is interesting to note that $n(k_1)$ is bounded by $n_0^*(= 1/\alpha t)$ for all n_0; further, that if $n_0 > n_0^*$, $n(k_1)$ varies as n_0^* (n_0^*/n_0), i.e., $n(k_1)$ decays as t^{-2}, even though n decays as t^{-1}.

Let us assume that initially (at times less than 1 second after burst) one has structure with $n_0(k_1)/n_0 \simeq 1$, and that the electron temperature variation among bursts is less significant than the density variation. Then at times after burst of the order of 5 seconds, one would expect density fluctuations to be less pronounced at densities with

$$n_0 > \frac{1}{\alpha t} \simeq \frac{1}{5\alpha} \quad . \tag{23}$$

With $\alpha \simeq 10^{-12}$ cm^3/sec, this condition becomes $n_0 > 2 \times 10^{11}$ cm^{-3}.

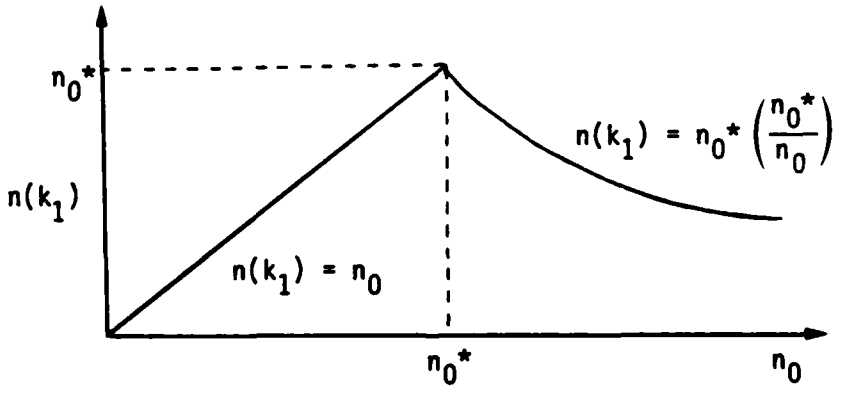

Figure 36.

Assuming full ionization and an electron temperature of five times the ambient, this corresponds to an ambient background density of 10^{12} cm^{-3}, i.e., significant structural non-sharpness at burst altitudes below about 100 km. Data from Blugill and Kingfish exhibit structural non-sharpness, while Checkmate and Starfish do not appear to exhibit structural non-sharpness.[9] This is in keeping with our theoretical expectation.

The applicability of nonlinear chemical damping of structure as a source of structural diffusiveness is confined to altitudes below 110 km if one is limited to times of the order of 5 seconds or less. However, this limitation may well be arbitrary. One can also consider the fate of structure generated by some source of instability (which is "turned off" at time t_1) in the time interval between t_1 and t_2, with t_2 denoting the time for onset of structural development appropriate to the gradient drift instability, for instance. If one takes t_2 = 300 seconds and t_1 = 1 second, the density limitations apply to n_0 as low as 3×10^9 cm^{-3}. With temperatures of 0.5 eV, this would affect structures up to an altitude of 160 km; at lower temperatures, which could be more appropriate at times of the order of hundreds of seconds after burst, from Sappenfield's α-coefficients[8] one sees that the effect could be even more extensive in altitude.

One can calculate the effect of the recombination on a general profile $n_0(X)$ through Eq. (12). Roughly speaking, for $n_0(X) < 1/\alpha t$ there is no loss of structure; for $n_0 > 1/\alpha t$ the structure is lost more rapidly than the mean density. To get some feeling for the effect, we consider

$$n_0 = n_0(k = 0)\left[1 + (1 - \varepsilon)\cos k_1 X\right] \quad , \quad 0 < \varepsilon < 1 \quad . \tag{24}$$

Then for $n_0\, \alpha t >> 1$ from Eq. (16b), one has

$$n(mk_1) = \frac{-1}{(\alpha t)^2} \int_0^{2\pi/k_1} \frac{1}{n_0(k = 0)} \frac{1}{[1 + (1 - \varepsilon)\cos k_1 X']} e^{-imk_1 X'} dX' \quad ,$$

$$m = \text{integer} \quad . \tag{25}$$

On substituting $z = k_1 X'$, and using some trigonometry and a standard formula:[10]

$$n(mk_1) = \frac{(-)\Pi}{k_1 n_0(k=0)} \frac{r^{2m}}{(\alpha t)^2} \frac{2}{\sqrt{2-\epsilon}} \frac{1}{\sqrt{\epsilon}} (-)^m r^{2m} \tag{26}$$

with

$$r = \frac{\sqrt{2-\epsilon} - \sqrt{\epsilon}}{\sqrt{2(1-\epsilon)}} \quad . \tag{27}$$

One can verify

$$0 < r < 1$$

for

$$0 < \epsilon < 1 \quad .$$

From Eq. (26), an <u>exponential</u> spectrum results from the profile of Eq. (24). The variation as $\epsilon \to 0$ is not strongly divergent. Hence, even for rather large initial modulations, structure at k_1 is lost more rapidly than the mean density, while at the same time bounded higher harmonic behavior is created.

From this analysis one concludes:

1. Chemical recombination produces a spectrum with

$$\frac{n(k \neq 0)}{n(k=0)} \approx \frac{n_0(k \neq 0)}{n_0(k=0)} \frac{n}{n_0}$$

for $n_0 \alpha t \gg 1$. Put another way, for $n_0 \alpha t \gg 1$, $n(k \neq 0) \sim t^{-2}$ while $n(k=0) \sim t^{-1}$.

2. From Figure 36, for all possible n_0 with $n_0(k \neq 0)/n_0(k=0)$ fixed and of order unity, the maximum $n(k \neq 0)$ at time t is of order n_0^*, $(= 1/\alpha t)$ and derives from $n_0 = n_0^*$. For $n_0 > n_0^*$, $n(k \neq 0) \leq n_0^*(n_0^*/n_0)$.

3. For $n_0 \alpha t \gg 1$ and

$$n_0 = n_0(k = 0)\ [1 + (1 - \varepsilon) \cos k_1 X] \quad , \quad 0 < \varepsilon < 1 \quad ,$$

an exponentially decaying (in wavenumber) spectrum of higher harmonics is generated [see Eq. (26)].

4. COULOMB DIFFUSION OF FAST IONS AND ELECTRONS

In this section expressions for the Coulomb diffusion of suprathermal electrons and ions across a slab geometry magnetic field are derived. The plasma model used for the calculation is identical to the one used in Appendix A with the exception that an x-directed ambipolar electric field will be required for the present discussion. Only elastic collisions are considered.

The equations appropriate to the description of transport of fast particles are:[11-13]

$$0 = \frac{\vec{j}_e \times \vec{B}_o}{c} - \nabla P_e - en_e\vec{E} + \nu_e \frac{m_e}{e}\vec{j}_e \tag{28a}$$

$$0 = \frac{\vec{j}_i \times \vec{B}_o}{c} - \nabla P_i + en_i\vec{E} - \nu_i \frac{m_i}{e}\vec{j}_i \quad . \tag{28b}$$

In Eqs. (28a) and (28b) the notation is similar to Appendix A except that quantities here refer to fast ions and electrons. Also, in the equations ν_e and ν_i are the collision frequencies for momentum loss with the less energetic background particles of the energetic electrons and ions, respectively; however, the reaction between energetic particles is neglected.

To lowest order in the assumed small parameters $\nu_e/|\Omega_e|$ and $\nu_i/|\Omega_i|$ the solutions to Eqs. (28a) and (28b) are:

$$\vec{j}_e(o) = \hat{y}\left(\frac{c}{B_o}\frac{\partial P_e}{\partial x} + en_e\vec{E}\cdot\hat{x}\right) \tag{29a}$$

$$\vec{j}_i(o) = \hat{y}\left(\frac{c}{B_o}\frac{\partial P_i}{\partial x} - en_i\vec{E}\cdot\hat{x}\right) \quad . \tag{29b}$$

To next order in the small parameter,

$$\vec{j}_e(1) = \hat{x}\,\frac{\nu_e m_e}{e}\left(\frac{c}{B_o}\right)^2\left(\frac{\partial P_e}{\partial x} + en_e\vec{E}\cdot\hat{x}\right) \tag{30a}$$

$$\vec{j}_i(1) = -\hat{x}\,\frac{\nu_i m_i}{e}\left(\frac{c}{B_o}\right)^2\left(\frac{\partial P_i}{\partial x} - en_i\vec{E}\cdot\hat{x}\right) \quad . \tag{30b}$$

Because of quasineutrality,

$$n_e \approx n_i \quad , \tag{31}$$

it is necessary that there be no x-directed current:

$$0 = (\vec{j}_e + \vec{j}_i)\cdot\hat{x} \quad . \tag{32}$$

Equation (32) implies that

$$\vec{E}\cdot\hat{x} = \frac{\nu_i m_i(\partial P_i/\partial x) - \nu_e m_e(\partial P_e/\partial x)}{en_e(\nu_e m_e + \nu_i m_i)} \tag{33}$$

and

$$\vec{j}_e(1)\cdot\hat{x} = -\vec{j}_i(1)\cdot\hat{x} = \hat{x}\,\frac{\nu_e\nu_i m_e m_i}{\nu_e m_e + \nu_i m_i}\,\frac{1}{e}$$

$$\left(\frac{c}{B_o}\right)^2\left(\frac{\partial P_e}{\partial x} + \frac{\partial P_i}{\partial x}\right) \quad . \tag{34}$$

Several features of Eqs. (33) and (34) are noteworthy. First, it is possible to determine a constraint on the ambipolar electric field in Eq. (33) which is consistent with quasineutrality if we scale the electric field as

$$\vec{E}\cdot\hat{x} \sim \frac{T}{eL} \tag{35}$$

where T is a temperature and L is a scale length. From Gauss' law this constraint is:

$$\frac{|n_e - n_i|}{|n_e|} \approx \frac{T}{4\pi n e^2 L^2} = \left(\frac{\lambda_D}{L}\right)^2 << 1 \quad . \tag{36}$$

In Eq. (36), the parameter λ_D is the Debye length. Second, Eq. (34) is independent of the ion collision frequency if

$$\nu_e m_e << \nu_i m_i \quad . \tag{37}$$

Physically, this corresponds to the ion transport across the magnetic field being constrained by the slower electron transport rate. Contrarily, if

$$\nu_i m_i << \nu_e m_e \quad , \tag{38}$$

the electron transport is constrained by the slower ion transport rate.

To complete the description of electron and ion transport across the magnetic field, a precise form for the electron and ion collision frequencies for suprathermal electrons and ions is necessary. Such expressions are found in Ref. 14 under the assumption that the thermal particles are electrically charged. For fast electrons collisions with both background electrons and ions contribute and

$$\nu_e = (7.7\ \lambda_{ee} + 3.9\ \lambda_{ei}) \times 10^{-6}\ n_e\ \varepsilon^{-3/2} \quad . \tag{39}$$

In Eq. (39) the parameters n_e and ε are the background electron density (in units of cm^{-3}) and energy (in units of electron volts), respectively. The Coulomb logarithms λ_{ee} and λ_{ei} are a function of the background electron temperature (T_e), background ion temperature (T_i), background electron density, and the relative ion to hydrogen mass ratio, μ:

$$\lambda_{ee} = 23 - \ln (n_e^{1/2} T_e^{-3/2}) \quad , \quad T_e < 10 \text{ eV}$$

$$= 24 - \ln (n_e^{1/2} T_e^{-1}) \quad , \quad T_e > 10 \text{ eV} \quad , \tag{40a}$$

$$\lambda_{ei} = 23 - \ln (n_e^{1/2} T_e^{-3/2}) \quad , \quad 10 \text{ eV} > T_e > T_i m_e/m_i$$

$$= 24 - \ln (n_e^{1/2} T_e^{-1}) \quad , \quad T_e > 10 \text{ eV} > T_i m_e/m_i$$

$$= 30 - \ln (n_i^{1/2} T_i^{-3/2} \mu^{-1}) \quad , \quad T_i > T_e m_i/m_e \quad . \tag{40b}$$

The ion collision frequency depends on whether the energetic ions have speeds which are in excess of or less than the electron thermal speed. For ions with speeds which are larger than the electron thermal speed electrons are the primary cause of drag on energetic ions and

$$\nu_i = 1.7 \times 10^{-4} \mu^{-1/2} \lambda_{ei} n_i \varepsilon^{-3/2} \quad . \tag{41}$$

where μ is the ratio of ion the proton mass. However, if the electron thermal speed is larger than the energetic ion speed drag on both electrons and ions contribute to the slowing down of a fast ion, i.e.,

$$\nu_i = 1.8 \times 10^{-7} \mu^{-1/2} \lambda_{ii} n_i \varepsilon^{-3/2} + 1.6 \times 10^{-9} \mu^{-1} n_e$$

$$\lambda_{ei} T_e^{-3/2} \quad . \tag{42}$$

In Eq. (42)

$$\lambda_{ii} = 41.5 - 0.5 \ln (n_e/T_e) \tag{43}$$

and it has been assumed the ion-ion collisions are betweer like ion species.

On using Eqs. (40a), (40b) and (43) to compare (39) and (41) or (42), one readily establishes that to within factors of unity

$$m_i \nu_i > m_e \nu_e \quad .$$

Hence particle fluxes can be estimated through the simplified form of Eq. (34):

$$n_e \nu_{ex} = n_i \nu_{ix} \simeq \frac{\nu_e m_e c^2}{e^2 B^2} \frac{\partial}{\partial x} (P_e + P_i) \quad . \tag{44}$$

If temperature variation is neglected, the density diffusion coefficient, D_n is given by:

$$D_n = \frac{m_e c^2}{e^2 B_o^2} \nu_e (T_e + T_i) \quad . \tag{45}$$

Let us seek the bound on wavelengths such that there is a density decay of at least e^{-1} in 5 minutes. This condition is:

$$D_n k_y^2 \geq 3 \times 10^{-3} \text{ sec}^{-1}$$

or equivalently (for $T_e = T_i$):

$$\lambda < 2.5 \times 10^5 \left(\frac{n_e}{10^9}\right)^{\frac{1}{2}} \left(\frac{0.1}{T_e}\right)^{\frac{1}{4}} \quad . \tag{46}$$

It is clear that significant Coulomb diffusion perpendicular to $\vec{B}$, as an early time phenomenon ($\leq$ 5 minutes time scale) is limited to wavelengths of order several kilometers or less.

5. SUMMARY AND OVERVIEW

In time sequence one expects first charge exchange and impact ionization (Section 2), and then recombination (Section 3), and Coulomb diffusion (Section 4) to affect the Fourier amplitudes in wavenumber of the charged particle density. The relationship between inverse wavenumber (k^{-1}) and structure scale length perpendicular to $\vec{B}$ (L_n) is ambiguous because L_n is not precisely defined; typically however one expects for reasonable definitions of L_n that

$$L_n \simeq \sqrt{2}\, k^{-1} \quad .$$

(To see this consider a wave $\alpha \cos kx$, $\alpha << 1$, on a background of size unity. Let us find the scale length corresponding to this wave. To first order in α we have

$$\nabla n/n = k\, \alpha \cos kx$$

or for the root mean squared value

$$(\nabla n/n)_{r.m.s.} = \left(\int dx\, k^2\, \alpha^2 \cos^2 kx / \int dx \right)^{\frac{1}{2}}$$

$$= k\, \alpha \sqrt{2}/2 \quad .$$

If we set $(\nabla n/n)_{r.m.s.} = \alpha/L_n$, $L_n = \sqrt{2}\, k^{-1}$.)

Subject to this uncertainty the various graphical results of Section 2 can be interpreted in terms of structure scale length directly.

The results from Section 2 furnish strong limitations on the persistence to lower altitude of structure due to fast particle structure present at the bomb burst altitude. Figures 11 and 13 establish for the 400 km burst with vertical field lines that degradation increases with decreasing length

scale, also that the major contribution to degradation comes from the region in altitude where the neutral mean free path for impact ionization is comparable to the structure size. At higher altitudes charge exchange, proportional to the ambient neutral density, is relatively weak; at lower altitudes the mean free path for impact ionization becomes less than the structure scale length and diffusion of ionized structure through the intervening neutral transport becomes weaker. The degradation of structure through neutral transport persists to lower altitudes for shorter wavelengths. Hence the increased damping of Fourier components with decreasing wavelength.

Figures 15 - 17 show that the wavelength dependence of degradation is increased when the magnetic field makes an angle with the vertical. This is due to the greater path length between altitudes.

The results of Section 2.2 show behavior which parallels that of Section 2.1. However, one notes that Figure 24 indicates more degradation than corresponding Figure 10. This appears to be largely due to the greater densities in the ionospheric model of Section 2.2 which result in the region of maximum increase in degradation being higher in altitude where the atmospheric density gradient scale lengths (and hence the extent of region of strong degradation) are greater.

The figures of Section 2.3 show for fireball behavior, where the cold neutral density is severely eroded, that degradation from neutral effects is less severe.

The results of Section 3 show that chemical recombination affects structure significantly if $n_0 \alpha t > 1$. (Here n_0 = the ionization at the start of the time interval, t, and α = the recombination coefficient.) Recombination causes all structure to decay more rapidly than a uniform background, and an initial structure with a single large amplitude Fourier component produces a spectrum of higher harmonics which exponentially decay with increasing wavenumber.

The results of Section 4 for diffusion due to Coulomb scattering show that significant degradation from this mechanism is limited to wavelengths of several kilometers or less provided the electron density is less than 10^9 cm^{-3} and the ionization temperature is greater than 0.1 eV.

The results of this report support the potential usefulness of the approach of separating early time behavior into two intervals:

a) $0 < t < t_1$, when plasma wave mechanisms develop structure.

b) $t_1 < t < t_2$, when structure decays according to non-plasma wave mechanisms, prior to the time when the magnetic field relaxes back to ambient.

It is possible due to the strength of the mechanisms of Sections 2 and 3 that detailed consideration of much of the plasma instability behavior which has occurred in connection with the early-time behavior of HANE (prior to t_1) is unnecessary for the provision of initial condition inputs to the SCENARIO code[2] (at t_2).

The following areas and questions derive from this report:

1. Detailed application of these notions to large scale codes.

2. Estimation of t_1 as a function of free-energy source (When do various free energy sources of instability turn off? Do the turn off times occur prior to the relaxation of the magnetic field back to ambient?).

3. Estimation of field line coupling effects (space-charge and electromagnetic) on the spectrum of structure.

4. Estimation of mass flow effects on structure scale lengths.

REFERENCES

1. This approach was suggested by L. Wittwer.

2. J. B. Workman, S. Y. F. Chu, and J. R. Ferrante, "A Power Model for Plasma Convection," DNA 4927F, Berkeley Research Associates, April, 1979.

3. W. L. Fite, J. S. Greene, Jr., A. W. Ali, and I. M. Pikus, "Kinetics of High-Energy Heavy-Particle Collisional Processes," in DNA 1948H.

4. F. W. Sears, An Introduction to Thermodynamics, the Kinetic Theory of Gases and Statistical Mechanics, Addison-Wesley Publishing Company, Reading, Massachusetts, 1953, p. 272.

5. R. W. Kilb and D. Glenn, "CMHD Simulations of Very High Altitude Nuclear Bursts from 0 to 1 Second," Mission Research Corporation, unpublished.

6. COSPAR Working Group IV, CIRA 1965, North-Holland Publishing Company, Amsterdam, 1965.

7. W. S. Knapp and K. Schwartz, "Aids for the Study of Electromagnetic Blackout," DNA 3499H, General Electric Co., February, 1975, Table 4-3.

8. W. W. White and F. E. Fajen, "High Altitude Phenomenology at Very Late Times," Mission Research Co., unpublished.

9. R. W. Kilb, private communication.

10. I. S. Gradshteyn and I. W. Ryzhik, Table of Integrals, Series, and Products, Academic Press, New York, 1965, formula 3.615, p. 368.

11. L. Spitzer, Jr., Physics of Fully Ionized Plasmas, John Wiley & Sons, 1962.

12. C. L. Longmire, Elementary Plasma Physics, John Wiley & Sons, 1963.

13. B. B. Kadomtsev, Plasma Turbulence, Academic Press, 1965.

14. D. L. Book, NRL Plasma Formulary, Naval Research Laboratory.

APPENDIX A

CLASSICAL PLASMA AND MAGNETIC FIELD TRANSPORT IN SLAB GEOMETRY

Two mechanisms, classical and anomalous, relax plasma and magnetic field configurations in such a way that entropy is maximized and thermal equilibrium is approached.[A1-A4] The difference between the two mechanisms is that those which are classical are a result of particle collisions whereas those which are anomalous are caused by wave phenomena. In general, the minimum rate of plasma and magnetic field transport possible in any configuration is classical with appropriate account being taken of geometry.

In this appendix the rate of plasma and magnetic field transport in a slab geometry is derived assuming classical electron-ion collisions. The precise plasma model used in the calculations is shown in Figure A-1. The z-directed magnetic field of strength B_o and the particle pressure, P, have x-directed gradients. The y-direction is ignorable.

The equations which give the plasma and magnetic field transport in the x-direction are for simply ionized ions:[A1-A4]

$$0 = \frac{\partial n_e}{\partial t} - \frac{1}{e} \nabla \cdot \vec{j}_e \tag{A-1a}$$

$$0 = \frac{\partial n_i}{\partial t} + \frac{1}{e} \nabla \cdot \vec{j}_i \tag{A-1b}$$

$$0 = -\nabla P_e - e n_e \vec{E} + \frac{\vec{j}_e \times \vec{B}_o}{c} + \frac{m_e}{e} \nu_{ei} (\vec{j}_e + \vec{j}_i) \tag{A-1c}$$

$$0 = -\nabla P_i + e n_i \vec{E} + \frac{\vec{j}_e \times \vec{B}_o}{c} - \frac{m_e}{e} \nu_{ei} (\vec{j}_e + \vec{j}_i) \tag{A-1d}$$

$$0 = \nabla \times \vec{B}_o - \frac{4\pi}{c} (\vec{j}_e + \vec{j}_i) \tag{A-1e}$$

$$0 = \nabla \times \vec{E} + \frac{1}{c} \frac{\partial \vec{B}_o}{\partial t} \quad . \tag{A-1f}$$

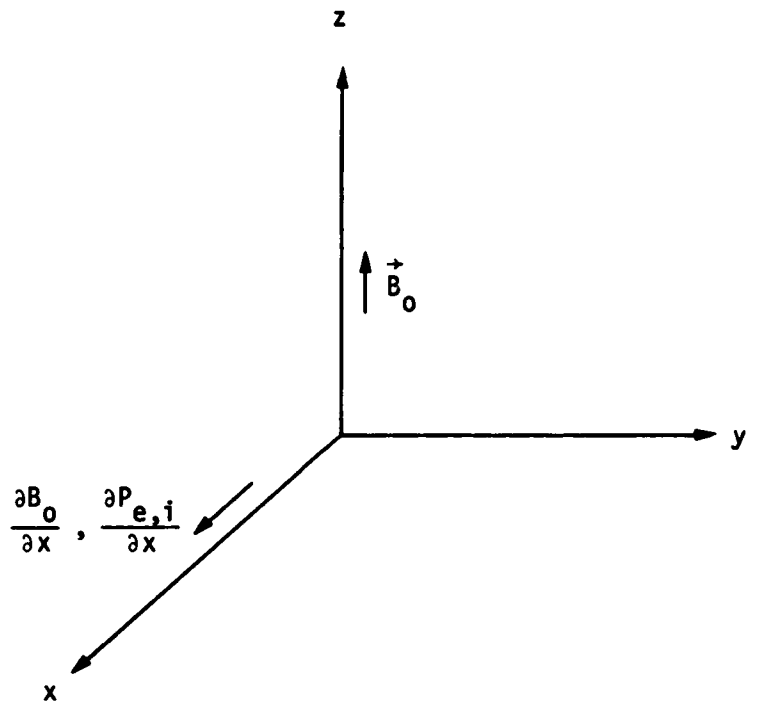

Figure A-1. Geometric model used as basis for calculations in Appendix A.

In Eqs. (A-1a - A-1f) the symbols n_e, n_i, P_e, P_i, $\vec{E}$, $\vec{j}_e$, $\vec{j}_i$, and ν_{ei} represent the electron density, ion density, electron pressure, electric field, ion pressure, electron current, ion current, and electron-ion collision frequency, respectively. The constants c, m_e and e are the speed of light, electron mass and the magnitude of the electron charge, respectively. Also, time is represented by "t."

Several features of Eqs. (A-1a) to (A-1f) are noteworthy. First, the addition of Eqs. (A-1c) and (A-1d) and using Eq. (A-1e) results in the equilibrium condition

$$e(n_i - n_e)\vec{E} = \nabla(P_e + P_i + B_o^2/8\pi) \quad . \tag{A-2}$$

This condition reduces to

$$0 = \nabla(P_e + P_i + B_o^2/8\pi) \tag{A-3}$$

if

$$\vec{E} = E_o\hat{y} \tag{A-4}$$

is a y-directed inductive electric field. Second, inertial terms have been neglected in Eqs. (A-1c) and (A-1d). When such terms are significant, nonlinear phenomena (e.g., shocks) rather than diffusive transport are described by the equations.[A2]

The electron and ion currents can be determined from Eqs. (A-1c) and (A-1d) in terms of the small parameter $\nu_{ei}/|\Omega_e|$ where

$$\Omega_e = -e\,B_o/m_e c \tag{A-5}$$

is the electron-cyclotron frequency. To lowest order,

$$\vec{j}_e(0) = \frac{c}{B_o}\left(\frac{\partial P_e}{\partial x}\hat{y} - \frac{en_eE_o}{B_o}\hat{x}\right) \tag{A-6a}$$

$$\vec{j}_i(0) = \frac{c}{B_o}\left(\frac{\partial P_i}{\partial x}\hat{y} + \frac{en_iE_o}{B_o}\hat{x}\right) \tag{A-6b}$$

where $\hat{x}$ is the x-directed unit vector. To next order,

$$\vec{j}_e(1) = -\vec{j}_i(0) = -\hat{x}\,\frac{\nu_{ei}}{\Omega_e}\,\frac{c}{B_o}\,\frac{\partial}{\partial x}\,(P_i + P_e) \quad . \tag{A-7}$$

Note that the convective $E_o \times \vec{B}_o$ term in Eqs. (A-6a) and (A-6b) does not explicitly contribute to the current in Eq. (A-7). Also, Eq. (A-7) does not depend on the existence of an ambipolar electric field.

Substitution of Eq. (A-7) into Eqs. (A-1a) and (A-1b) leads to the following expressions for the rate of which electron and ion density profiles change with time,

$$\frac{\partial n_e}{\partial t} = \frac{\partial n_i}{\partial t} = \frac{\partial}{\partial x}\left(\frac{c}{eB_o}\right)^2 m_e\,\nu_{ei}\,\frac{\partial}{\partial x}\,(P_e + P_i)$$

$$= \frac{\partial}{\partial x}\,D_n\,\frac{\partial}{\partial x}\,n_e \quad , \tag{A-8}$$

with the diffusion coefficient,

$$D_n = \left(\frac{c}{eB_o}\right)^2 m_e\,(T_e + T_i)\,\nu_{ei} \quad . \tag{A-9}$$

In deriving the second form of Eq. (A-8)

$$P = n_e(T_e + T_i)$$

with constant electron and ion temperature, T_e and T_i, respectively.

To find the rate at which the magnetic field diffuses with time it is noteworthy that Eq. (A-3) implies that the total particle plus magnetic pressure is a function of time but not of space; i.e.,

$$g(t) = P_e + P_i + B_o^2/8\pi \quad . \tag{A-10}$$

The differentiation of Eq. (A-10) with respect to time results in

$$\frac{\partial}{\partial t}\ \frac{B_o^2}{8\pi} = \frac{B_o}{4\pi}\ \frac{\partial B_o}{\partial t} = \frac{dg(t)}{dt} - (T_e + T_i)\ \frac{\partial n_e}{\partial t} \quad . \tag{A-11}$$

From Eqs. (A-3), (A-8), and (A-11) it follows that

$$\frac{\partial}{\partial t}\ \frac{B_o^2}{8\pi} = \frac{\partial}{\partial x}\ D_n\ \frac{\partial}{\partial x}\ \frac{B_o^2}{8\pi} + \frac{dg(t)}{dt} \tag{A-12}$$

or since the function, g(t) does not depend on space

$$\frac{\partial}{\partial t}\ [f(x,t)] = \frac{\partial}{\partial x}\ D_n\ \frac{\partial}{\partial x}\ f(x,t) \tag{A-13}$$

where

$$f(x,t) \equiv B_o^2/8\pi - g(t) \quad . \tag{A-14}$$

Eqs. (A-8), (A-12) and (A-13) indicate that the diffusion equations for the magnetic pressure and density have identical forms only if g(t) does not depend on time (i.e., the total pressure in the system is a constant for all times). Furthermore, the directions of density and magnetic field transport are oppositely directed.

To determine whether density or magnetic field diffuse more rapidly it is useful to define the scale lengths,

$$L_n = |n_e/(\partial n_e/\partial x)| \tag{A-15a}$$

$$L_B = |B_o^2/(\partial B_o^2/\partial x)| \quad . \tag{A-15b}$$

Equation (A-3) permits the scale lengths to be related:

$$L_n = \beta L_B \tag{A-16}$$

with

$$\beta = 8\pi\ (P_e + P_i)/B_o^2 \quad . \tag{A-17}$$

The scale times for diffusion of density and f(x,t),

$$\tau_n = |n_e/(\partial n_e/\partial t)| \tag{A-18}$$

$$\tau_f = |f(x,t)/[\partial f(x,t)/\partial t]| \quad , \tag{A-19}$$

are then related from Eqs. (A-8) and (A-13) by

$$\tau_n/\tau_f \approx \beta^2 \quad . \tag{A-20}$$

For g(t) a constant Eq. (A-20) gives the ratio of the time scale for density variation to the time scale for magnetic field pressure variation.

It follows from Eq. (A-20) that the density diffuses more rapidly than f(x,t) for $\beta < 1$, but f(x,t) diffuses more rapidly than the density for $\beta > 1$. Because of the increasing magnetic field modification for high beta plasmas, this behavior is consistent with the diamagnetic properties of the assumed plasma model.

In addition to determining the time and spatial evolution of the density and magnetic field it is possible to write an expression for the evolution of the inductive y-directed electric field. From Eqs. (A-1f) and (A-12)

$$\frac{\partial E_o}{\partial x} = \frac{4\pi}{cB_o}\left(\frac{\partial}{\partial x} D_n \frac{\partial}{\partial x}\frac{B_o^2}{8\pi} + \frac{dg(t)}{dt}\right) \tag{A-21}$$

and so the electric field depends not only on the magnetic field strength and spatial gradients of the magnetic field but also on the time variation of the total pressure within the system.

REFERENCES

A1. L. Spitzer, Jr., Physics of Fully Ionized Plasmas, John Wiley & Sons, 1962.

A2. C. L. Longmire, Elementary Plasma Physics, John Wiley & Sons, 1963.

A3. B. B. Kadomtsev, Plasma Turbulence, Academic Press, 1965.

A4. T. J. M. Boyd and J. J. Sanderson, Plasma Dynamics, Barnes & Noble, Inc., 1969.

APPENDIX B. DECAY OF FAST ION STRUCTURE IN THE IONOSPHERE

ABSTRACT

Fast ions with energies in excess of ten kilovolts can be generated within the ionosphere by magnetic storms or manmade mechanisms. It is shown that charge exchange of fast ions into fast neutrals results in the rapid attenuation of structure with neutral mean free paths much larger than the structure dimensions and the generation of structure of larger size. For structure with dimensions much larger than the neutral mean free path fast neutral loss is diffusive rather than convective and attenuation of structure is less rapid.

INTRODUCTION

Fast ions with energies in excess of one kilovolt can be generated in the ionosphere by magnetic storms [Sharp et al., 1976a; Sharp et al., 1976b; Banks, 1979] or manmade mechanisms [Zinn et al., 1966; Glasstone and Dolan, 1977]. Once formed, these ions travel on magnetic drift surfaces toward the northern or southern conjugate points. While following their trajectories the ions can undergo charge exchange collisions with less energetic background neutrals [Fite, et al., 1972] thereby generating fast neutrals, with energies approximating the original fast ion energies, and slow much less energetic ions. The fast neutrals are not constrained to magnetic drift surfaces and follow a trajectory, consistent with those forces which are not electromagnetic or electrostatic (e.g., gravity, pressure, etc.), until they undergo an impact ionization collision with the cold neutral background [Fite, et al., 1972]. With the impact ionization collision a fast ion and a less energetic neutral are generated. In addition to undergoing charge exchange and impact ionization processes, the fast particles can concurrently or in separate collisions ionize cold neutral material [Fite, et al., 1972] and increase the total amount of ionization available. Successive charge exchange, impact ionization and ionization events occur until the energy of the initially fast particles is reduced to the background level.

The purpose of this appendix is to calculate the attenuation, resulting from charge exchange and impact ionization collisions, of an initial structure of fast ions as the structure travels down field lines into denser portions of the atmosphere. It is demonstrated that the attenuation is most rapid for small structures because for such structures the neutral mean free path for impact ionization is larger than the structure dimensions and neutral transport is convective rather than diffusive.

Subsequent portions of this appendix are divided in the following way. In the second and third sections the plasma model and equation are described, respectively. In the fourth and fifth sections solutions to the equations in a homogeneous plasma and in the ionosphere are given. The final section is a discussion of results.

MODEL

The model used as the basis for the calculations is shown in Figure B-1. A z-directed magnetic field of strength B_0 is assumed antiparallel to the gravity vector, $\vec{g}$. Hence, the magnetic field geometry is most applicable to regions near the north or south magnetic poles. The inhomogeneity of the fast ion density, n_1, and fast neutral density, n_2, are x-directed and the y-coordinate is ignorable. The evolution of an infinitesimal z-directed length of the structure is followed and the velocity space fast ion distribution function is assumed for definiteness in the calculations to be a delta function with equal perpendicular and parallel speeds. The velocity distribution of neutrals formed by charge exchange is isotropic in the x- and y-directions because of ion gyration about the magnetic field. To determine the evolution of a finite z-directed length of structure and a velocity spread of particles solutions analogous to the ones which are considered here would have to be superimposed.

The fast particles are taken to be either singly ionized or neutral monatomic oxygen. The cold neutral background species and density as a function of altitude, n_s, are taken from Fite et al., 1972 . Possible variation of neutral density in the direction orthogonal to the magnetic field is neglected.

EQUATIONS FOR EVOLUTION OF FAST PARTICLE DENSITIES

To establish the evolution of the fast particle structure, the calculation is carried out in a Lagrangian frame of reference moving with the initial fast ion structure along the magnetic field. The relevant equations are:

$$\frac{dn_1(x,t)}{dt} = - \nu_1(t)n_1(x,t) + \nu_2(t)n_2(x,t) \qquad \text{(B-1a)}$$

$$\frac{dn_2(x,t)}{dt} = - \nu_2(t)n_2(x,t) + \nu_1(t)n_1(x,t) - \nu_o(\frac{d}{dx},t)\, n_2(x,t) \qquad \text{(B-1b)}$$

with the symbols the fast ion density as a function of x and t $[n_1(x,t)]$, fast neutral density as a function of x and t $[n_2(x,t)]$ charge exchange collision frequency as a function of time $[\nu_1(t)]$, impact ionization collision frequency $[\nu_2(t)]$, and neutral loss frequency which is a function of a differential operator and time $[\nu_o(d/dx,t)]$. It is useful to rewrite Eqs. (B-1a) and (B-1b) in terms of the Fourier integrals:

$$n_1(x,t) = \int_{-\infty}^{\infty} dk\; n_1(k,t)\; \exp(ikx) \quad . \qquad \text{(B-2a)}$$

$$n_2(x,t) = \int_{-\infty}^{\infty} dk\; n_2(k,t)\; \exp(ikx) \quad . \qquad \text{(B-2b)}$$

Hence,

$$\frac{d}{dt} + \nu_1(t)\; n_1(k,t) = \nu_2(t)n_2(k,t) \qquad \text{(B-3a)}$$

$$[\frac{d}{dt} + \nu_2(t) + \nu_o(k,t)]n_2(k,t) = \nu_1(t)n_1(k,t) \qquad \text{(B-3b)}$$

The collision frequencies in Eqs. (B-1a), (B-1b), (B-3a) and (B-3b) are determined through the relations

$$\nu_1(t) = v_1 \sum_s \sigma_{1s} n_s(t) \tag{B-4a}$$

$$\nu_2(t) = v_2 \sum_s \sigma_{2s} n_s(t) \tag{B-4b}$$

v_1, v_2, σ_{1s}, σ_{2s} and $n_s(t)$ represent the fast ion speed, fast neutral speed, cross section for collisions of fast ions with cold neutrals of species s, cross section for collisions of fast neutrals with cold neutrals of species s, and cold neutral density of species s as a function of time, respectively.

Two forms for the neutral loss frequency have been chosen. First if the neutral mean free path is much larger than the structure dimensions in the x-direction, neutrals can convect out of the structure before they can undergo an impact ionization collision. Hence, such particles are effectively lost from the structure, and the collision loss frequency is approximated by the following expression [Sears, 1953].

$$\nu_0(k,t) = kv_2/8 \tag{B-5}$$

For cases when the neutral mean free path is much smaller than the structure dimension in the x-coordinate a diffusive loss model is appropriate [Sears, 1953] and

$$\nu_0(k,t) = \frac{k^2 |\hat{v}_2 \times (\hat{B}_0/B_0)|^2}{3\nu_2} \quad . \tag{B-6}$$

In the numerical solution of Eqs. (B-3a) and (B-3b) the expression for the collisional loss term is taken to be the minimum of Eqs. (B-5) and (B-6).

SOLUTION OF EQUATIONS FOR A HOMOGENEOUS IONOSPHERE

Qualitative features of the fast particle structure decay can be discovered by solving Eqs. (B-3a) and (B-3b) in the limit when the collision frequencies and the neutral loss frequency are time independent. Hence, in this section Eqs. (B-3a) and (B-3b) are solved and discussed in this limit.

Eqs. (B-3a) and (B-3b) can now be written as:

$$[p(k) + \nu_1]n_1(k) = \nu_2 n_2(k) \tag{B-7a}$$

$$[p(k) + \nu_o + \nu_2]n_2(k) = \nu_1 n_1(k) \tag{B-7b}$$

with

$$n_1(k,t) \sim \exp[p(k)t] \tag{B-8a}$$

$$n_2(k,t) \sim \exp[p(k)t] \tag{B-8b}$$

It follows from Eqs. (B-7a) and (B-7b) that the explicit values for p(k) are a solution of the characteristic equation:

$$0 = p(k)^2 + (\nu_1 + \nu_2 + \nu_o)p(k) + \nu_1\nu_o \quad . \tag{B-9}$$

Hence:

$$p_{\pm}(k) = \frac{-(\nu_1 + \nu_2 + \nu_o) \pm [(\nu_1 + \nu_2 + \nu_o)^2 - 4\nu_1\nu_o]^{1/2}}{2} \quad , \tag{B-10}$$

where the two solutions to Eq. (B-9) have been written as $p_{\pm}(k)$ depending on the sign in front of the square root in Eq. (B-10). Both $p_{\pm}(k)$ are negative definite and contribute to decay of structure. Based on Eqs. (B-8a), (B-8b) and (B-10) the explicit solution to Eqs. (B-7a) and (B-7b) can be written as

$$n_1(k,t) = \frac{\nu_2}{p(k) + \nu_1} A(k) \exp(p_+ t) + \frac{\nu_2}{p_- + \nu_1} B(k) \exp(p_- t) \quad , \qquad \text{(B-11a)}$$

$$n_2(k,t) = A(k) \exp(p_+ t) + B(k) \exp(p_- t) \quad . \qquad \text{(B-11b)}$$

where A(k) and B(k) are constants. With the initial conditions

$$n_1(k,t)\Big|_{t=0} = n_0(k) \qquad \text{(B-12a)}$$

$$n_2(k,t)\Big|_{t=0} = 0, \qquad \text{(B-12b)}$$

Equations (B-11a) and (B-11b) can be rewritten as

$$n_1(k,t) = \frac{n_0(k)}{p_- - p_+} \{(p_- + \nu_1) \exp(p_+ t) - (p_+ + \nu_1) \exp(p_- t)\} \qquad \text{(B-13a)}$$

$$n_2(k,t) = \frac{n_0(k)}{p_- - p_+} \frac{(p_+ + \nu_1)(p_- + \nu_1)}{\nu_2} [\exp(p_+ t) - \exp(p_- t)] \qquad \text{(B-13b)}$$

with the dependence of p_+ and p_- on wavenumber suppressed for brevity of notation.

It is useful to rewrite Eqs. (B-13a) and (B-13b) in two limits. First, for ν_1, $\nu_2 \ll \nu_0$ fast neutrals are lost almost immediately after being formed and the equations become

$$n_1(k,t) \approx n_0(k) \exp(-\nu_1 t) \qquad \text{(B-14a)}$$

$$n_2(k,t) \approx (\nu_1/\nu_0)\, n_0(k) \exp(-\nu_1 t) \quad . \qquad \text{(B-14b)}$$

An important feature of these equations is that fast ion structure only depends on its initial value and the charge exchange collision frequency. Second, for $\nu_1, \nu_2 \gg \nu_0$ the total number of fast ions plus fast neutrals decreases very slowly relative to the charge exchange and impact ionization collision times and

$$n_1(k,t) \approx \frac{n_o(k)}{\nu_1 + \nu_2} \{\nu_2 + \nu_1 \exp[-(\nu_1 + \nu_2)t]\} \quad \text{(B-15a)}$$

$$n_2(k,t) \approx \frac{n_o(k)}{\nu_1 + \nu_2} \nu_1 \{1 - \exp[-(\nu_1 + \nu_2)t]\} \quad \text{(B-15b)}$$

Hence, for time approaching infinity

$$n_1(k,t)/n_2(k,t) \approx \nu_2/\nu_1 \quad . \quad \text{(B-16)}$$

which is independent of k.

SOLUTION OF EQUATIONS FOR AN INHOMOGENEOUS IONOSPHERE

Equations (B-3a) and (B-3b) have been solved numerically for the real inhomogeneous ionosphere. The initial conditions for the calculation are an altitude of 800 kilometers at t = 0 and

$$n_o(k) = n_1(k,t)\Big|_{t=0} \quad \text{(B-17a)}$$

$$0 = n_2(k,t)\Big|_{t=0} \quad . \quad \text{(B-17b)}$$

The numerical solution is followed down the field lines to an altitude at which the fast ion density for each wavelength is about 0.001 of its initial value. For vertical magnetic field lines, a fast particle energy of 12 keV, and equal parallel and perpendicular speeds, the fast ion velocities down the field line are 1.9×10^7 cm/sec. The calculations have been carried out for two different ionospheric models with the cold neutral diatomic nitrogen, diatomic oxygen and monatomic oxygen densities at each altitude given by the CIRA 1965 Hour 10, Model 9 and 1965 Hour 22, Model 4 tables, respectively [COSPAR Working Group IV, 1965]. (The first model is appropriate to a quiescent ionosphere with a very high level of solar activity while the second model is appropriate to an ionosphere with a level of mean solar activity but under the magnetic storm conditions of Sharp, et al., 1976a and Sharp, et al., 1976b.)

Results are summarized in Figures B-2 and B-3 for wavenumbers with $k > 10^{-5}$ cm^{-1} and the two ionospheric models. The calculations indicate that the fast ion attenuation is insensitive to the wavenumber particularly at higher altitudes. Ion structure decays by three orders of magnitude in going from 800 km to 370 km in altitude in Figure B-2 and from 800 to 280 km in Figure B-3. Also, the fast neutral density is calculated to be appreciably smaller than the fast ion density. These results are consistent with the homogeneous cold neutral results of the previous section in the limit when the mean free path for neutral collision is much larger than structure dimensions [Eqs. (B-14a) and (B-14b)]. Hence, to lowest order the structure behavior is more closely approximated by Eqs. (B-14a) and (B-14b) rather than Eq. (B-16) and the evolution of the fast ion structure in the Lagrangian frame of reference moving along the magnetic field with the fast ions is

$$n_1(k,t) = n_0(k,t) \exp[- \int_0^t dt\ \nu_1(t)] \quad . \tag{B-18}$$

For lower altitudes or larger wavelengths the neutral mean free path is much smaller than the structure size and the loss of particles is governed by neutral diffusion rather than neutral convection. It follows from Eq. (B-6) that this diffusive loss is weakest for inverse wavenumber and impact ionization frequency going to infinity. Under circumstances when $\nu_0(t) \ll \nu_1(t)$, $\nu_2(t)$ the relationship between $n_1(k,t)$ and $n_2(k,t)$ is governed by an adiabatic relation analogous to Eq. (B-18),

$$n_1(k,t)/n_2(k,t) = \nu_1(t)/\nu_2(t) \quad . \tag{B-19}$$

In the limit of $k \to 0$, the relation between the fast ion and fast neutral densities as a function of the initial ion density, Eq. (B-17a), is:

$$n_1(k,t) = \frac{n_0(k)}{1 + \nu_1(t)/\nu_2(t)} \tag{B-20a}$$

$$n_2(k,t) = \frac{[\nu_1(t)/\nu_2(t)]n_0(k)}{1 + \nu_1(t)/\nu_2(t)} \quad . \tag{B-20b}$$

Eq. (B-20a) indicates that at the altitude where the ion density for $k \to \infty$ is one thousand times smaller than its initial value (i.e., 370 km for Figure B-2 and 280 km for Figure B-3) the ratio

$$\frac{n_1(k,t)\Big|_{k\to\infty}}{n_1(k,t)\Big|_{k\to 0}} \simeq 10^{-3}\,[1 + \nu_1/\nu_2] \quad . \tag{B-21}$$

For the neutral densities and cross-sections appropriate to both Figures B-2 and B-3 this ratio is approximately 7×10^{-3}.

It is clear that the exponential decay rate for structure at a given wavenumber is greatest for altitudes where the neutral mean free path is comparable to the inverse wavenumber.

DISCUSSION

Fast ions can be generated by both geophysical or manmade phenomena in the upper atmosphere.

It has been shown that the charge exchange of fast ions (e.g., monatomic oxygen with 12 keV kinetic energy) into fast neutrals is a powerful mechanism for attenuating fast ion structure from the altitude of 800 km down to 370 kilometers (for Figure B-2) and 280 kilometers (for Figure B-3) as long as Eqs. (B-14a) and (B-14b) are a good description for the decay. For the parameters and ionospheric model appropriate to Figures B-2 and B-3 this corresponds to an inverse wavenumber of approximately 2 and 1 km, respectively. For larger inverse wavenumbers or lower altitudes diffusion of fast neutrals becomes more important and so the wavenumber component of structure decays at a less rapid rate. Consequently for structure consisting of significant wavenumber components with inverse wavenumbers less than or greater than the ion and neutral mean free path, decay as well as structure shape changes occur due to strong attenuation of the short wavelength contribution.

The calculations also demonstrate that the penetration of fast ion structure originating at high altitude to lower altitudes is a strong function of ionospheric model. The physical basis for this effect is the increase in neutral densities especially at altitudes above 300 km with increasing solar activity.

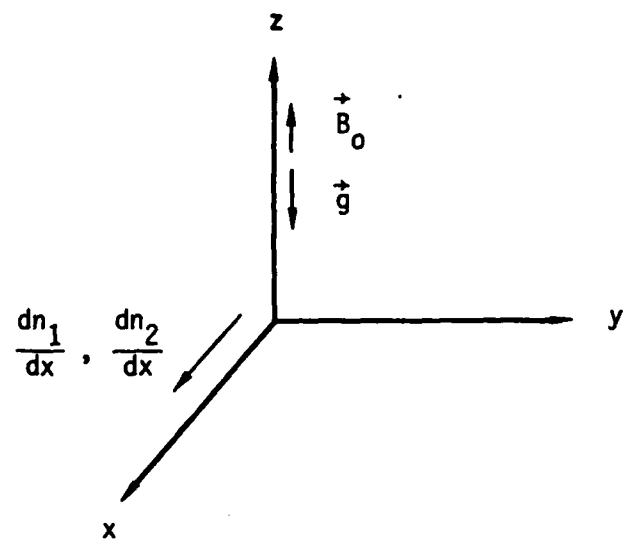

Figure B-1. Model used as basis for calculations.

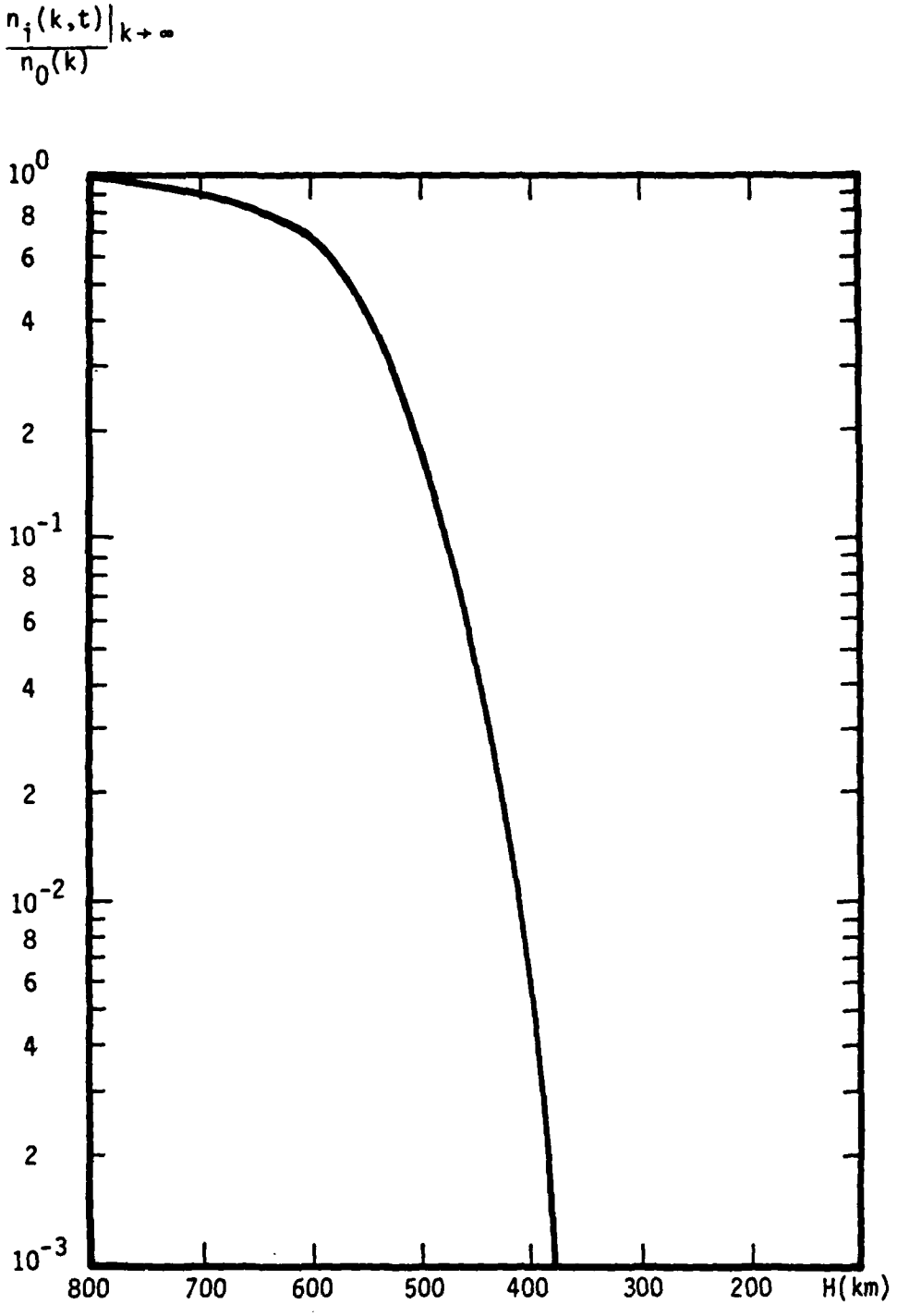

Figure B-2. Fast ion density for $k \to \infty$ in units of the initial fast ion density at 800 km vs. altitude in kilometers.

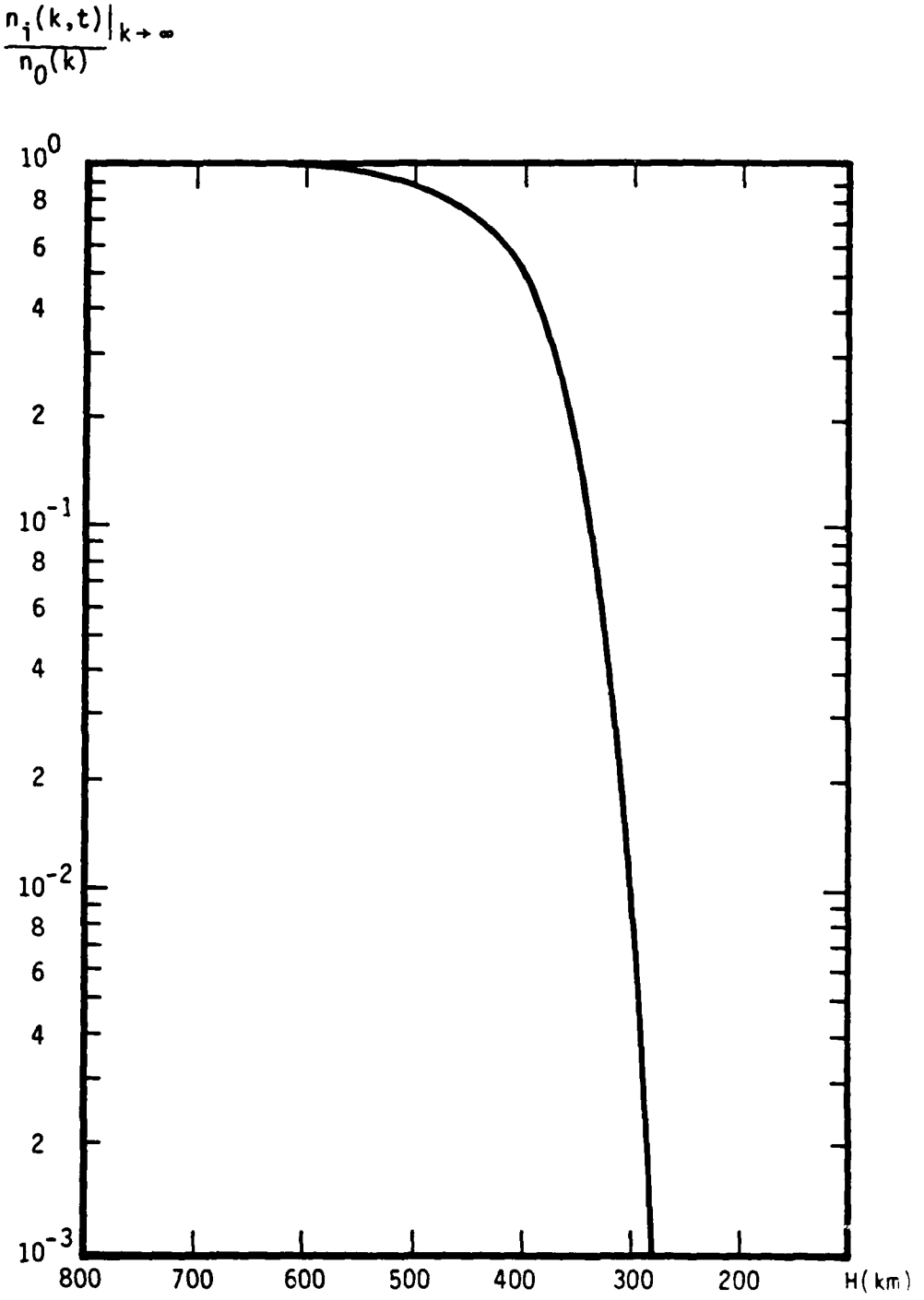

Figure B-3. Fast ion density for $k \to \infty$ in units of the initial ion density at 800 km vs. altitude in kilometers for a magnetic storm ionosphere model.

AD-A117 497 JAYCOR SAN DIEGO CA F/G 4/1
SOME PHYSICAL AND CHEMICAL ASPECTS OF STRIATION STRUCTURE.(U)
AUG 80 S R GOLDMAN, J L SPERLING DNA001-79-C-0050
UNCLASSIFIED DNA-5912Z NL

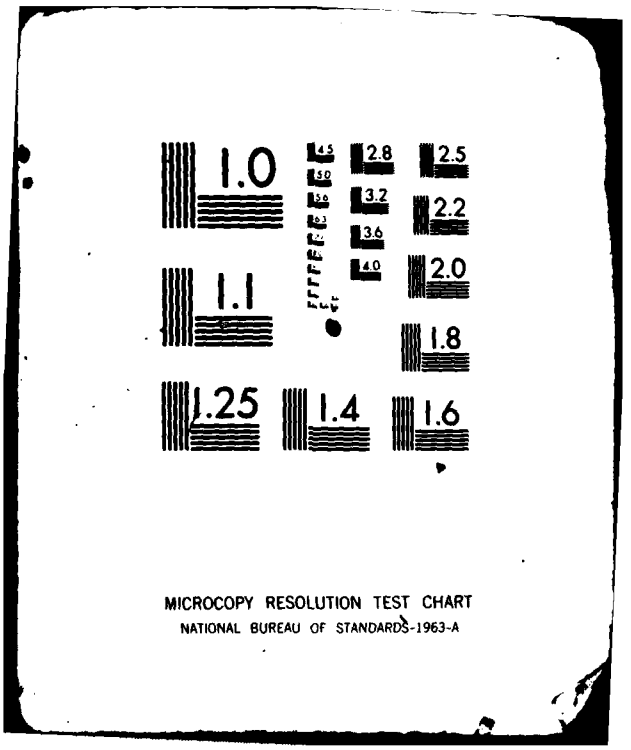
1.0
1.1
1.25
1.4
1.6
1.8
2.0
2.2
2.5
2.8
3.2
3.6
4.0
MICROCOPY RESOLUTION TEST CHART
NATIONAL BUREAU OF STANDARDS-1963-A

REFERENCES

Banks, P. M., Magnetosphere, Ionosphere and Atmosphere Interactions, in Space Plasma Physics: The Study of Solar System Plasmas, Vol. 2, Part I, p. 688, National Academy of Sciences, Washington, D.C., 1979.

COSPAR Working Group IV, CIRA 1965, North-Holland Publishing Company, Amsterdam, 1965.

Fite, W. L., J. S. Greene, Jr., A. W. Ali and I. M. Pikus, Kinetics of High-Energy Heavy-Particle Collisional Processes, in Defense Nuclear Agency Reaction Rate Handbook, DNA 1948H, edited by M. Bortner and T. Barnes, Ch. 15, GE-TEMPO, 1972.

Glasstone, S. and P. J. Dolan, The Effects of Nuclear Weapons, Chapter 1, United States Departments of Defense and Energy, Washington, D.C., 1977.

Sears, F. W., An Introduction to Thermodynamics, the Kinetic Theory of Gases and Statistical Mechanics, Chapter 13, Addison-Wesley, Reading, Massachusetts, 1953.

Sharp, R. D., R. G. Johnson and E. G. Shelley, The Morphology of Energetic O^+ Ions During Two Magnetic Storms: Temporal Variations, J. Geophys. Res. 81, 3283, 1976a.

Sharp, R. D., R. G. Johnson and E. G. Shelley, The Morphology of Energetic O^+ Ions During Two Magnetic Storms: Latitudinal Variations, J. Geophys. Res. 81, 3292, 1976b.

Zinn, J., H. Hoerlin and A. G. Petschek, The Motion of Bomb Debris Following the Starfish Test, in Radiation Trapped in the Earth's Magnetic Field, B. M. McCormack, Ed. (D. Reidel Publ. Co., Dordrecht-Holland, 1966), pp. 671-692.

APPENDIX C. ELECTRIC FIELD LIMITATION OF DRIFT DISSIPATIVE WAVE GENERATION IN IONOSPHERIC STRUCTURES

ABSTRACT

Coupled background electric fields and density profiles exist across the sides of striations and other elongated ionospheric structures. The presence of the electric field profoundly modifies the behavior of drift dissipative waves by shifting the location of the waves away from the point where the relative density gradient is a maximum, consequently inhibiting the growth of the waves.

INTRODUCTION

Plasma waves in the ionosphere are sources of electron density structure. In addition within the laboratory it is well known that they can lead to anomalous diffusion of pre-existing density structures [Cheng and Okuda, 1977].

It has been observed that barium cloud strations and other ionospheric plasma density structures (as in Equatorial Spread F) tend to be elongated in the plane perpendicular to the geomagnetic field in the direction of the $\vec{E} \times \vec{B}$ drift [Perkins and Doles, 1976; Scannapieco and Ossakow, 1976; Tsunoda et al., 1979]. (Here $\vec{E}$ and $\vec{B}$ are the ambient electric and magnetic fields, respectively.) Around most of the perimeter of such structures, the ambient electric field should be parallel (or anti-parallel) to the density gradient. Gradient-drift modes have been shown to be stabilized under these conditions [Perkins and Doles, 1976]. Hudson and Kennel [1975] have pointed out the possible importance of drift-dissipative modes in ionospheric structures. The purpose of this calculation is to evaluate the effect of this electric field on drift dissipative mode growth rates. The key result of the calculation is that drift dissipative modes tend to be stabilized through the presence of ambient electric fields.

This appendix is divided into two additional sections. In the second section, the dispersion relation for drift dissipative modes in the presence of an ambient electric field is derived and solved. The final section is a short discussion and review of the results.

DISPERSION RELATION

a. General Analysis

In this section, the nonlocal dispersion relation for drift dissipative modes in the presence of an ambient electric field is derived and solved. As the basis for the calculation, a plasma model is used (see Figure C-1) in which the x-direction is normal to the surface of the striation perimeter. The plasma density gradient and the ambient electric field are then x-directed. The plasma is assumed to be homogeneous in the y- and z-directions and a uniform z-directed field is present. The plasma itself consists of a quasi-neutral mixture of electrons and singly ionized ions. A uniform background of neutral particles is also permitted in the model.

Consistent with the plasma model, the wave electric field has the form

$$\vec{E}_1(x,y,z,t) = -\nabla\{\phi_1(x)\exp[i(k_y y + k_z z - \omega t)]\} \quad , \tag{C-1}$$

where t denotes the time. In a collisionless plasma and in the absence of the ambient electric field, the dispersion relation for drift waves with frequencies well below the ion-gyrofrequency has the form [Cheng and Okuda, 1976]

$$\frac{d^2\phi_1}{dx^2} + Q\phi_1 = 0 \quad , \tag{C-2}$$

where

$$Q = \Delta^{-1} \Sigma_\alpha [1 + (\omega + \omega_\alpha^*) X_{0\alpha}]/T_\alpha \quad ,$$

$$\Delta = \rho_i^2 (\omega + \omega_i^*)(X_{0i} - X_{1i})/T_i \quad ,$$

$$\omega_\alpha^* = -k_y \rho_\alpha^2 \Omega_\alpha \, d[\ln(n)]/dx \quad ,$$

$$X_{\ell d} = I_\ell(b_\alpha) \exp(-b_\alpha) \, Z(\omega/\sqrt{2}\, k_z v_a)/\sqrt{2}\, k_z v_a \quad ,$$

$$b_\alpha = (k_y \rho_\alpha)^2 \quad ,$$

$$\rho_\alpha = v_\alpha/\Omega_\alpha \quad ,$$

$$v_\alpha = (T_\alpha/m_\alpha)^{1/2} \quad ,$$

$$\Omega_\alpha = q_\alpha B_0/m_\alpha c \quad . \qquad \text{(C-3)}$$

The magnetic field strength, the speed of light, the charge of a species α particle, the temperature of species α, and the mass of species α are here represented by B_0, c, q_α, T_α, and m_α, respectively. Electron and ion parameters are differentiated by subscripts e and i. The plasma dispersion function (Fried and Conte, 1961) and the modified Bessel function of the first kind are denoted by Z and I_ℓ, respectively. Also, the dependence of ϕ_1, Q, A, and n on x has been suppressed in the notation of Eqs. (C-2) and (C-3).

To modify Eq. (C-2) into a form appropriate to drift dissipative modes in the presence of an ambient electric field, the following replacements are made [Kadomtsev, 1965]:

$$\omega' \equiv \omega + k_y c E_0(x)/B_0 \quad , \qquad \text{(C-4a)}$$

$$[1 + (\omega + \omega_e^*) X_{0e}]/T_e \rightarrow \frac{1}{T_e} \left(\frac{-\omega_e^* + i\delta}{\omega' + i\delta} \right) , \qquad \text{(C-4b)}$$

where

$$\delta = (k_z v_e)^2/\nu_e \quad . \qquad \text{(C-5)}$$

In Eqs. (C-4) and (C-5), the quantities $E_0(x)$ and ν_e denote the ambient electric field strength and the electron collision frequency, respectively. For electron collisions with ions,

$$\nu_e = \frac{23.4 - 1.15 \log_{10}(n_e) + 3.45 \log_{10}(T_e)}{3.5 \times 10^5} \frac{n_e}{T_e^{3/2}} , \qquad (C\text{-}6)$$

where T_e and n_e are in units of electron volts and inverse cubic centimeters, respectively.

To illustrate the effect of the electric field on the drift mode, it is assumed that

$$\delta \gg |\omega|, \quad |\omega_i^*|, \quad |w_e^*| \quad . \qquad (C\text{-}7a)$$

In addition,

$$|\omega| \gg (2)^{1/2} k_z v_i \qquad (C\text{-}7b)$$

for drift waves, and so the parameter Q in Eq. (C-3) can be written as

$$Q(x) = \frac{1}{T_i \Delta\omega'} [a\omega' - b\omega_i^*] , \qquad (C\text{-}8a)$$

where

$$a = 1 + T_i/T_e - I_0(b_i) \exp(-b_i) , \qquad (C\text{-}8b)$$

$$b = I_0(b_i) \exp(-b_i) . \qquad (C\text{-}8c)$$

Now if the x-directed scale length of the wave is much smaller than the density gradient scale length,

$$\ell = \left|\frac{1}{\phi_1}\right| \left|\frac{d\phi_1}{dx}\right|^{-1} \ll \left|\frac{1}{n} \frac{dn}{dx}\right|^{-1} , \qquad (C\text{-}9)$$

then the parameter Q can be expanded in a Taylor series about the point, x=0, where the local dispersion relation is approximately satisfied; i.e.,

$$Q(x) = Q(x)\Big|_{x=0} + \frac{dQ(x)}{dx}\Big|_{x=0} + \frac{x^2}{2} \frac{d^2Q(x)}{dx^2}\Big|_{x=0} . \qquad (C\text{-}10)$$

The first term on the right-hand side of Eq. (C-10) is the local dispersion relation for drift waves when equated to zero [Kadomtsev, 1965]. The last two terms contribute to the nonlocal dispersion of the modes.

Now if

$$Q(x)\Big|_{x=0} \approx 0 \quad , \tag{C-11a}$$

$$\frac{dQ(x)}{dx}\Big|_{x=0} = 0 \quad , \tag{C-11b}$$

then

$$\frac{dQ(x)}{dx}\Big|_{x=0} \approx \frac{1}{T_i \Delta\omega'} \, a \, \frac{d\omega'}{dx} - b \, \frac{d\omega_i^*}{dx} \Big|_{x=0} \quad , \tag{C-12a}$$

$$\frac{d^2Q(x)}{dx^2}\Big|_{x=0} \approx \frac{1}{T_i \Delta\omega'} \, a \, \frac{d^2\omega'}{dx^2} - b \, \frac{d^2\omega_i^*}{dx^2} \Big|_{x=0} \quad . \tag{C-12b}$$

In Sub-appendix CA, relations [Eqs. (C-8a)-(C-9b)] between the background density gradient and electric field strength are evaluated. Using these expressions, Eqs. (C-12a) and (C-12b) can be rewritten in the following way.

$$\frac{dQ(x)}{dx}\Big|_{x=0} = - \frac{1}{T_i \Delta\omega'} \left[(1 + T_i/T_e) \, \frac{d\omega_i^*}{dx} + a \, k_y \, \frac{cE_\infty}{B_0} \, \frac{n_\infty}{n^2} \, \frac{dn}{dx} \right] \Big|_{x=0} \quad , \tag{C-13a}$$

$$\frac{d^2Q(x)}{dx^2}\Big|_{x=0} = - \frac{1}{T_i \Delta\omega'} \left[(1 + T_i/T_e) \, \frac{d^2\omega_i^*}{dx^2} + a \, k_y \, \frac{cE_\infty n_\infty}{B_0} \, \frac{d}{dx} \left(\frac{1}{n^2} \, \frac{dn}{dx} \right) \right] \Big|_{x=0} \quad . \tag{C-13b}$$

b. Asymptotic Analysis

Let $\omega_{i,m}^*$ denote the maximum value of ω_i^* [and hence of $(1/n)(dn/dx)$] over the range in x with spatial variation.

The effect of the background electric field can be categorized by

$$\left|\frac{\omega_{i,m}^{*}}{k_y c E_\infty n_\infty / B_0 n(x)}\right| = r \quad . \tag{C-14}$$

For $r \gg 1$ electric field effects in Eqs. (C-13a) and (C-13b) are insignificant, the drift mode is localized around the value of x such that $|\omega_{i,m}^{*}|$ is a maximum, and the growth rate scales as $|\omega_{i,m}^{*}|$. (See Sub-appendix CB for details.)

For $r \ll 1$ the electric field effect is dominant. This limit obtains for density gradient scale lengths perpendicular to B ($= L_n$) with

$$\frac{L_n}{\rho_i} \gg \frac{v_i}{cE_{xo}/B} \quad . \tag{C-15}$$

Typically $v_i/(cE_{xo}/B)$ is less than 10 and the inequality is satisfied for $L_n > 0.1$ km.

To demonstrate the electric field effect quantitatively for $r \ll 1$, assume that

$$\frac{1}{n}\frac{d^q n}{dx^q} < \xi\left(\frac{1}{n}\frac{dn}{dx}\right)_m^q \equiv \xi/L^q \tag{C-16}$$

with ξ of order unity, and the maximum value of $[1/n(dn/dx)]$ denoted by $[1/n(dn/dx)]_m$.

Condition (C-16) appears to be likely for higher order density derivatives, although one could mathematically construct density profiles which violate it. On using Eqs. (C-11b) and (C-13a) one obtains:

$$\left(\frac{1}{n}\frac{dn}{dx}\right)_{x=0} = \frac{\dfrac{k_y \rho_i^2 \omega_{ci}\left(1 + T_i/T_e\right)}{a\, k_y (cE_\infty/B_0)(n_\infty/n)}\left(\dfrac{1}{n}\dfrac{d^2 n}{dx^2}\right)_{x=0}}{1 - \dfrac{k_y \rho_i^2 \omega_{ci}\left(\frac{1}{n}\frac{dn}{dx}\right)_{x=0}}{a\, k_y (cE_\infty/B)(n_\infty/n)}\left[1 + (T_i/T_e)\right]} \quad , \tag{C-17}$$

with a of order unity for $T_i \approx T_e$.

Using Eq. (C-16) to lowest order in r this becomes:

$$\left(\frac{1}{n}\ \frac{dn}{dx}\right)_{x=0} = \frac{k_y \rho_i^2 \omega_{ci}(1 + T_i/T_e)}{a k_y c\, E_\infty n_\infty/(nR_0)L}\ \frac{1}{L} \simeq \frac{r}{L}\ . \qquad \text{(C-18)}$$

From Eqs. (C-16) and (C-18) it is clear that

$$\left(\frac{1}{n}\frac{dn}{dx}\right)_{x=0} < \left(\frac{1}{n}\frac{dn}{dx}\right)_m\ . \qquad \text{(C-19)}$$

c. Nonlocal Behavior

We note additionally that previous nonlocal treatments of drift waves have been in the zero ambient electric field limit and have been carried out about the points where the magnitude of the diamagnetic drift frequency is a maximum and d^2Q/dx^2 is positive. However, with an ambient electric field, Eq. (C-19) indicates that the drift waves are centered about points which are different from the ones at which the magnitude of the drift frequency is a maximum. Moreover, the extremum values of Q are shifted in space as a result of the ambient electric field and it is not obvious that d^2Q/dx^2 is positive or negative. Hence, in Sub-appendix CC the nonlocal dispersion of drift waves is examined first for d^2Q/dx^2 greater than zero and then less than zero.

It should be noted that the detailed features of the x-directed mode structure are higher order in the inverse density gradient scale length than the shift in modal location. Consequently, these detailed features are correspondingly less significant.

DISCUSSION

A nonlocal analysis of the dispersion relation for drift dissipative modes in the presence of an ambient electric field has been evaluated. A critical feature of the calculation is the coupling of the ambient electric field to the density profile (Sub-appendix CA).

The analysis suggests that drift dissipative waves are in general stabilized by the presence of an ambient electric field which shifts the location of the drift waves away from the points where the relative density gradient (i.e., n'/n) is a maximum and the growth of the waves is most vigorous. In particular, for situations where the E x B velocity is larger than the diamagnetic velocity at the location of maximum logarithmic density gradient by a factor of r ($\gg 1$), typically for gradient scale lengths $L_n > 0.1$ km, the growth rate for instability is a factor of r^{-1} lower than the expected value in the absence of the ambient electric field.

Further these calculations suggest that drift-dissipative waves could be triggered on the sides of elongated F region structures by the increase of atmosphere ionization in the E region at dawn. The creation of a highly conducting, relatively uniform ($\perp B$) region of ionization connected by magnetic field lines to the altitude of structure could act to short out background electric fields acting along the sides of structure. The resulting growth rates for drift-dissipative waves would then be substantially increased. This could lead to anomalous diffusion of Spread F structure in a manner analogous to that already discussed in connection with laboratory plasmas [Cheng and Okuda, 1977].

SUB-APPENDIX CA

In this sub-appendix, a relationship between the ambient electric field and density profile is derived based upon the constraint that the flow across the density gradient is quasi-neutral.

Neglecting terms which do not contribute to the formation of ambipolar electric fields and inertial terms, the ion momentum equation has the form

$$0 = \frac{q_i \hat{v}_i \times \hat{B}_o}{m_i c} - \nu_1 \hat{v}_i + \frac{q\hat{E}_{ox}(x)}{m_i} - \frac{T_i}{m_i n} \nabla n \quad , \qquad \text{(CA-1)}$$

where ν_i is the ion-neutral collision frequency.

In an expansion in the small parameter ν_i/Ω_i, the lowest-order component of the ion velocity in the direction of the density gradient is

$$v_{ix}(x) = \frac{qE_{ox}(x)}{m_i} - \frac{T_i}{m_i n(x)} \frac{dn(x)}{dx} \frac{\nu_i}{\Omega_i^2} \quad . \tag{CA-2}$$

In the ionosphere,

$$|\nu_e/\Omega_e| \ll |\nu_i/\Omega_i| \quad , \tag{CA-3}$$

where ν_e is the electron-neutral collision frequency. Hence, the quasi-neutral condition requires that

$$\text{const.} = n(x)\, v_{ix}(x) \quad . \tag{CA-4}$$

For

$$0 = \lim_{x \to \infty}[dn(x)/dx] \quad , \tag{CA-5}$$

and assuming that only $n(x)$ and $E_{ox}(x)$ are functions of position, then

$$\frac{qE_{ox}(x)}{m_i} - \frac{T_i}{m_i} \frac{1}{n(x)} \frac{dn(x)}{dx} = \frac{qE_\infty n_\infty}{n(x) m_i} \quad , \tag{CA-6}$$

where

$$E_\infty = \lim_{x \to \infty}[E_{ox}(x)] \quad , \tag{CA-7a}$$

$$n_\infty = \lim_{x \to \infty}[n(x)] \quad . \tag{CA-7b}$$

It follows from Eq. (CA-6) that

$$\omega' + \omega_i^*(x) = \omega + k_y \frac{cE_\infty n_\infty}{B_o n(x)} \quad , \tag{CA-8}$$

and

$$\frac{d\omega'(x)}{dx} = -\frac{d\omega_i^*}{dx} - k_y \frac{cE_\infty n_\infty}{B_o n^2(x)} \frac{dn(x)}{dx} \quad , \tag{CA-9a}$$

$$\frac{d^2\omega'(x)}{dx} = -\frac{d^2\omega_i^*}{dx} - k_y \frac{cE_\infty n_\infty}{B_o} \frac{d}{dx}\left[\frac{1}{n^2(x)} \frac{dn(x)}{dx}\right] \quad . \tag{CA-9b}$$

SUB-APPENDIX CB

It has been shown that a large ambient x-directed electric field shifts the location of drift wave localization away from the location of largest density gradient. To show that the shift causes a reduction of drift wave growth rate from its optimum value, the local dispersion relation with the destabilizing parallel electron diffusion term can be written in the following way:

$$0 = \frac{T_i}{T_e} \frac{i\beta(\alpha - 1) + (\alpha - \beta^2)}{\alpha^2 + \beta^2} + a - b \frac{T_i}{T_e} \frac{1}{\alpha} \qquad \text{(CB-1)}$$

where

$$\alpha = -\omega'/\omega_e^* \quad , \qquad \beta = -\delta/\omega_e^* \quad . \qquad \text{(CB-2)}$$

Fixing the value of k_y and permitting k_z^2 to vary in such a way that β is constant, it is evident that the solution for the real and imaginary value for ω' scales like ω_e^* (i.e.,

$$\omega' \sim \omega_e^* d \qquad \text{(CB-3)}$$

where d is a constant). Hence, there is a growth rate reduction by the ratio of

$$\frac{\omega_e^*}{(\omega_e^*)_{max}} = \frac{\gamma}{\gamma_{max}} \qquad \text{(CB-4)}$$

at a location where the drift frequency is reduced from its maximum value. Here, the quantity γ/γ_{max} is the ratio of the drift wave growth rates at the location of drift wave localization with and without an electric field, respectively.

In the preceding discussion the stabilizing role of ion-neutral collisions has not been considered. However, Kadomtsev points out that for ion-neutral collision frequency, ν_i,

$$|\omega_e^*/\nu_i| < 1 \qquad \text{(CB-5)}$$

leads to wave stabilization [Kadomtsev, 1965]. Hence, for fixed ion-neutral collision frequency, reduction of drift wave frequency from its maximum value with fixed k_y leads to a reduction of parameter space permitting drift wave growth. It follows that a large ambient electric field lessens the vigor of the drift waves both with and without stabilization by ion-neutral collisions.

SUB-APPENDIX CC

In this sub-appendix Eq. (CC-2) is explicitly solved for d^2Q/dx^2 greater than and less than zero, respectively.

1. $d^2Q/dx^2 > 0$

Through the use of Eqs. (CC-10), (CC-11b) and (CC-13b), Eq. (CC-2) can be written, for $d^2Q/dx^2 > 0$, in the form

$$0 = \left[\frac{d^2}{du^2} + \frac{1}{2} + p - \frac{u^2}{4}\right]\phi_1(u) \quad , \tag{CC-1}$$

where

$$u = x \exp(-i\pi/4)/\beta \tag{CC-2}$$

$$Q\Big|_{x=0} = -i(1/2 + p)\ \beta^{-2} \quad , \tag{CC-3}$$

$$\frac{d^2Q}{dx^2}\Bigg|_{x=0} = -1/2\ \beta^{-4} \quad . \tag{CC-4}$$

The appropriate boundary conditions for the differential equation correspond to the outward propagation of energy away from x = 0. Hence, the index p has a non-negative integral value, and the solution to Eq. (CC-1) is the parabolic cylinder function [Morse and Feshbach, 1953],

$$\phi_1(x) \propto D_p[x \exp(-i\pi/4)/\beta] \quad . \tag{CC-5}$$

From Eqs. (CC-3) and (CC-4) it follows that there is a negative contribution to the growth of the wave caused by the outward convection of energy away from $x = 0$ [Pearlstein and Berk, 1969; Sperling and Perkins, 1976]. The explicit form for this negative contribution is

$$\gamma_d = -|\omega_i^*|(1 + 2p)\left(1 + \frac{T_i}{T_e}\right)\frac{\rho_i}{L}\left\{[I_0(b_i) - I_1(b_i)]\exp(-b_i)\left[1 + \frac{T_i}{T_e} - I_0(b_i)\right.\right.$$

$$\left.\left.\times \exp(-b_i)\right]^{-3}\ [2\alpha_2^2 - 3\alpha_3^v]\right\}^{1/2} \quad . \tag{CC-6}$$

2. $\underline{d^2Q/dx^2 < 0}$

For the case that $d^2Q/dx^2 < 0$, Eq. (CC-2) becomes

$$0 = \left[\frac{d^2}{du^2} + \frac{1}{2} + p - \frac{u^2}{4}\right]\phi_1(u) \quad , \tag{CC-7}$$

where

$$u = x/\beta \quad , \tag{CC-8}$$

$$Q\Big|_{x=0} = (1/2 + p)\beta^{-2} \quad , \tag{CC-9}$$

$$\left.\frac{d^2Q}{dx^2}\right|_{x=0} = -1/2\ \beta^{-4} \quad . \tag{CC-10}$$

The appropriate boundary conditions for Eq. (CC-7) is that ϕ_1 is localized around the point $x = 0$ [i.e., $\phi_1(u) \to 0$ for $|x| \to \infty$]. The solution to Eq. (CC-7) is the parabolic cylinder function

$$\phi_1(x) \propto D_p(x/\beta) \tag{CC-11}$$

for p equal to a non-negative integer.

From Eqs. (CC-2) and (CC-3), it follows that there is a real frequency shift, $\delta\omega$, associated with the nonlocal dispersion relation:

$$\delta\omega = -\omega_i^* |\gamma_d/\omega_i^*| \qquad \text{(CC-12)}$$

where γ_d is given by Eq. (CC-6).

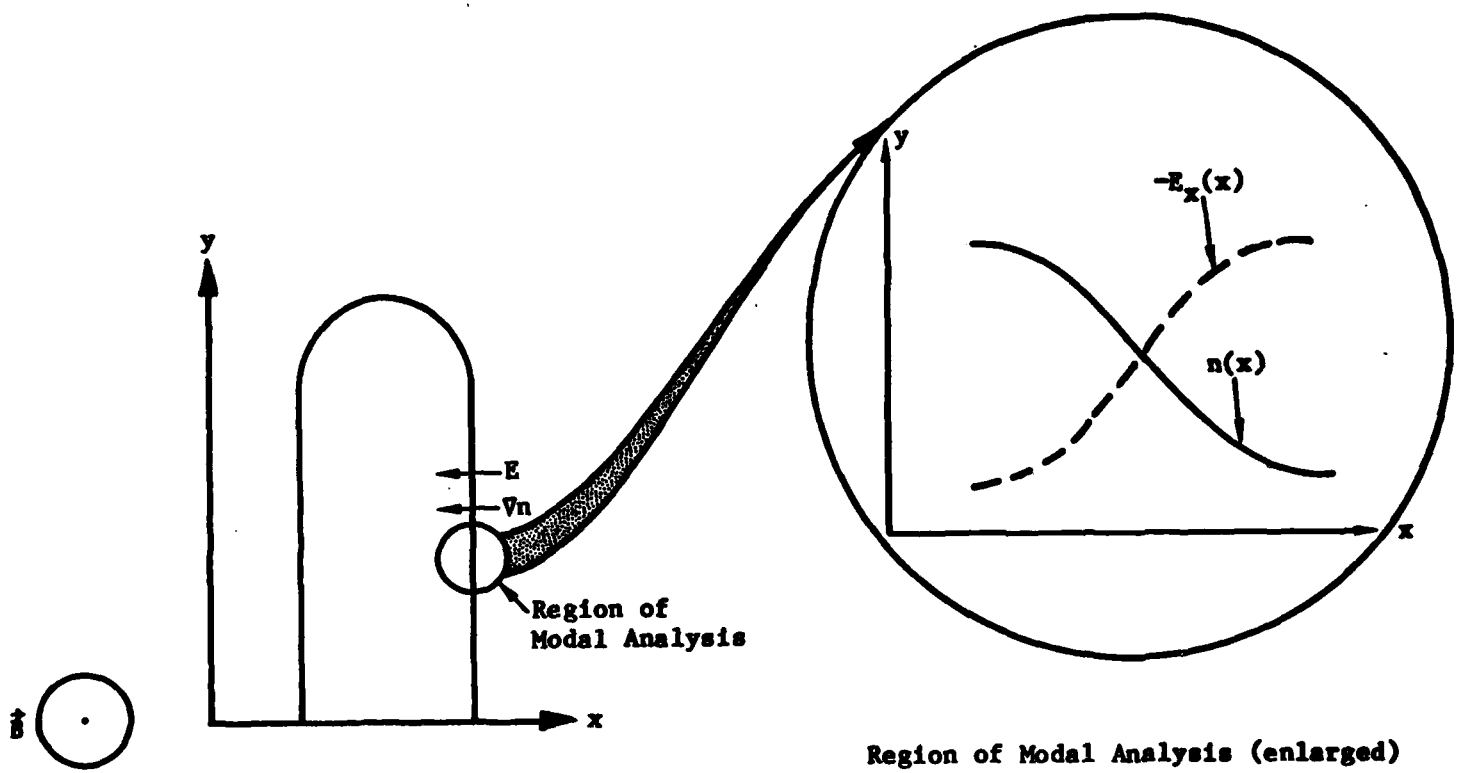

Figure C-1. Geometry for elongated structure in the plane perpendicular to $\vec{B}$. The $\vec{E} \times \vec{B}$ velocity is in the direction of elongation (y-direction). Hence along the sides of the structure $\vec{E}$ and ∇n are in the x-direction. The small circular area along the side is enlarged to show electric field and plasma density variation in x.

REFERENCES

Cheng, C. Z. and H. Okuda, "Formation of Convective Cells, Anomalous Diffusion and Strong Plasma Turbulence Due to Drift Instabilities," Phys. Rev. Lett. 38, 708, 1977.

Fried, B. D. and S. D. Conte, The Plasma Dispersion Function, Academic Press, New York, 1961.

Hudson, M. K. and C. F. Kennel, "Linear Theory of Equatorial Spread F," J. Geophys. Res. 80, 4581, 1975.

Kadomtsev, B. B., Plasma Turbulence, Chapter IV, Academic Press, New York, 1965.

Morse, P. M. and H. Feshbach, Methods of Theoretical Physics, p. 1565, McGraw-Hill, New York, 1953.

Pearlstein, L. D. and H. L. Berk, "Universal Eigenmode in a Strongly Sheared Magnetic Field," Phys. Rev. Lett. 23, 220, 1969.

Perkins, F. W. and J. H. Doles, III, "Velocity Shear and the E × B Instability," J. Geophys. Res. 80, 211, 1975.

Scannapieco, A. J. and S. L. Ossakow, "Nonlinear Equatorial Spread-F," Geophys. Res. Lett. 3, 451, 1976.

Sperling, J. L. and F. W. Perkins, "Ion-Cyclotron Waves in Nonuniform Plasmas and Parametric Instabilities," Phys. Fluids 19, 281, 1976.

Tsunoda, R. T., M. J. Baron and J. Owen, "Altair: An Incoherent Scatter Radar for Equatorial Spread F Studies," Radio Science 14, 1111, 1979.

DISTRIBUTION LIST

DEPARTMENT OF DEFENSE

Defense Nuclear Agency
ATTN: RAEE
ATTN: STNA
ATTN: NATD
ATTN: NAFD
4 cy ATTN: TITL
6 cy ATTN: RAAE

Defense Technical Information Center
12 cy ATTN: DD

Field Command
Defense Nuclear Agency
ATTN: FCPR, J. McDaniel

Field Command
Defense Nuclear Agency
Livermore Branch
ATTN: FCPRL

DEPARTMENT OF THE NAVY

Naval Research Laboratory
ATTN: Code 6780, S. Ossakow

DEPARTMENT OF THE AIR FORCE

Air Force Weapons Laboratory
Air Force Systems Command
ATTN: NTYC
ATTN: SUL
ATTN: NTN

DEPARTMENT OF ENERGY CONTRACTORS

Lawrence Livermore National Lab
ATTN: Technical Info Dept Library

Los Alamos National Laboratory
ATTN: MS 664, J. Zinn
ATTN: D. Simons
ATTN: S. Schmidt

DEPARTMENT OF DEFENSE CONTRACTORS

Berkeley Research Associates, Inc
ATTN: J. Workman

DEPARTMENT OF DEFENSE CONTRACTORS (Continued)

ESL, Inc
ATTN: J. Marshall

General Research Corp
ATTN: J. Garbarino
ATTN: J. Ise, Jr.

JAYCOR
4 cy ATTN: J. Sperling

Kaman Tempo
ATTN: DASIAC
ATTN: W. Knapp
ATTN: W. McNamara

Mission Research Corp
ATTN: Tech Library
ATTN: D. Sappenfield
ATTN: R. Hendrick
ATTN: S. Gutsche
ATTN: R. Kilb
ATTN: F. Fajen
ATTN: R. Bogusch

R & D Associates
ATTN: W. Karzas
ATTN: H. Ory
ATTN: F. Gilmore
ATTN: W. Wright
ATTN: R. Lelevier
ATTN: R. Turco
ATTN: B. Gabbard
ATTN: M. Gantsweg
ATTN: C. Greifinger
ATTN: P. Haas

Science Applications, Inc
ATTN: L. Linson
ATTN: D. Hamlin

SRI International
ATTN: C. Rino
ATTN: W. Chesnut

Visidyne, Inc
ATTN: J. Carpenter
ATTN: C. Humphrey